EngD Thesis

Investigating Catalytic Activity at Oxide Surfaces Using a QM/MM Methodology

Christopher Downing

Supervisor: Professor C. R. A. Catlow
Second Supervisor: Dr Scott Woodley
Industry Supervisor: Dr Paul Sherwood

UCL

Abstract

A set of complementary studies has been undertaken to investigate the interaction of CO_2 with metal oxide surfaces. Beginning with the simple and well-studied magnesium oxide surface, work progressed to include a manganese dopant near the MgO active site before shifting to manganese oxide. All work made use of the Quantum Mechanical/Molecular Mechanical (QM/MM) methodology implemented within the ChemShell code, which combines information from an electronic structure calculation on atoms in the vicinity of the adsorption site with relaxation effects from a large component of the surrounding catalyst system.

Initial findings showed that CO_2 interacts favourably with the MgO (100) terrace, and that the presence of trapped electrons at surface oxygen vacancies opens up the possibility for catalytic chemical processes to occur. Particular attention was paid to the CO_2 radical anion species formed when the adsorbate binds to a vacancy containing a single electron, and the addition of hydrogen to the surface-adsorbate complex allowed for a number of catalytic cycles to be identified. Manganese doping was used to investigate the effect of a transition metal on the interaction between the adsorbate and the vacancy, before moving on to the transition metal oxide where more complex effects such as lattice distortion and antiferromagnetic ordering were included in the model. Finally, work was performed on the related system Li-doped MgO in order to investigate an open question regarding the activation barrier for methyl radical formation as part of the oxidative coupling of methane reaction.

Declaration

I, Christopher Alan Downing, confirm that the work presented in this thesis is my own. Where information has been derived from other sources, I confirm that this has been indicated in the thesis.

Acknowledgements

The work described within this thesis would not have been possible without support from the Molecular Modelling and Materials Science Doctoral Training Centre within the University College London Department of Chemistry, the STFC Scientific Computing Department, and the UK Materials Chemistry Consortium. I am grateful to all involved, and in particular wish to thank Dr Paul Sherwood and Dr Tom Keal for their support in allowing me to spend part of my research time working with them at STFC Daresbury.

I would like to thank my wife, family and friends for their support and patience throughout the process of performing the research presented here and the preparation of this thesis.

I would also like to express thanks to Dr Alexey Sokol and Dr Andrew Logsdail for their guidance and encouragement throughout the various stages of the work.

Finally, I would like express my sincere gratitude to my supervisor Professor Richard Catlow for his support throughout my time at UCL. In particular I am grateful for his encouragement in working on a variety of research projects as well as his commitment, positivity and attentiveness when providing advice and feedback. His input has been essential in making these four years both satisfying and enjoyable.

Contents

List of Figures

List of Tables

Chapter 1

General Introduction

Understanding and making use of the chemistry of carbon dioxide represents a fundemental challenge in modern science. The inter-linked problems of dwindling fossil fuel supplies and increasing atmospheric CO_2 are such that regardless of any other advances in our energy generation, storage and transport methods, the ability to capture CO_2 and recycle it to form a hydrocarbon product would be hugely advantageous.

The most significant barrier to widespread adoption of CO_2 recycling is based on cost, with respect to both the initial capture process and subsequent reactions with other species. The second of these problems, on which this thesis will be focused, necessitates the use of a catalyst to minimise the energetic barriers at key reaction steps, allowing the conversion of CO_2 to higher value products to proceed with the minimum possible expenditure of energy.

The modelling of chemical reactions necessitates the use of electronic structure calculation methods, the application of which is generally restricted to a limited number of atoms. Restricting the computational model to such a component of the chemical system places limits on the achievable accuracy. Therefore, a hybrid quantum mechanical/molecular mechanical (QM/MM) approach has been chosen for this research in order to include the effects of longer-range interactions with minimal additional computational cost.

Within the present chapter, the justification for research on CO_2 conversion catalysis and related processes will be outlined in greater detail, along with a description of current progress, from the earliest cases of industrial-scale utilization of CO_2 as a reactant, to more recent advances in catalyst development. Particular attention will be paid to previous studies which have used computational modelling to predict how CO_2 will behave when interacting with catalytic active sites.

In chapter two, an overview of the computational methods used to perform the research is provided, progressing from the fundamental theory associated with each method through to the actual software implementations and computing resources used.

In chapter three, four and five, the primary results for CO_2 reactivity at oxide surfaces are described. The work focuses initially on magnesium oxide, and progresses via transition-metal doped MgO to the structurally similar manganese oxide. As well as investigating the interactions of CO_2 with the surfaces of these materials, oxygen vacancies in various charge states are considered as potential catalytically active sites. The study of transition metal oxides presents additional technical challenges when compared with the simpler alkali earth oxides, and so the additional computational developments necessary in order to complete the work will be discussed.

Chapter six contains results pertaining to a related catalytic process, the oxidative coupling of methane, for which Li-doped MgO is proposed as a catalyst. In particular, this study focuses on how the QM/MM embedding environment influences the calculated reaction barrier for the abstraction of a hydrogen atom from CH_4.

Finally, chapter seven provides a summary of the findings presented earlier, proposed future work, and concluding remarks. Tables and figures forming part of the discussion are presented within the relevant chapters. A list of publications produced over the course of carrying out the presented work, and additional data such as the interatomic potentials and effective core potentials used within the calculations, are contained within the appendices.

1.1 Background

A major source of motivation for research into the reactivity of carbon dioxide is the observed correlation between atmospheric CO_2 levels and rising global average temperatures. Efforts to mitigate this temperature rise by reducing the rate of CO_2 release to the atmosphere are drawing widespread attention. A second significant justification for the need to perform research into CO_2 recycling is the prospect of worldwide oil reserves being strained to such an extent that using hydrocarbons as a primary fuel source becomes unattractive. Each of these problems, their consequences and proposed solutions have been described in detail elsewhere,[1–3] and are outlined here.

1.1.1 Climate Change

Like a number of other atmospheric gases including methane and water vapour, CO_2 absorbs and emits infrared radiation *via* its stretching and bending vibrational modes. These gases contribute to the greenhouse effect, a process by which long wavelength thermal radiation is trapped within the atmosphere causing the equilibrium surface temperature of a planet to be increased relative to the temperature which would be observed without atmospheric gases. The greenhouse effect is a natural process essential to the development of life on Earth, but one which is suceptible to change as a result of human activity.

Since the start of the industrial revolution, emission of CO_2 to the atmosphere has dramatically increased, shifting the concentration from around 280 parts per million (ppm) to the current value of around 400ppm.[4]

Data from Antarctic ice cores[5] has shown that over the last 420,000 years, temperature and concentrations of atmospheric CO_2 and CH_4 have correlated well.

Based on this and other similar findings, an anthropogenic cause for recent climate change is considered to be “extremely likely”.[6]

Current models produced by the Intergovernmental Panel on Climate Change (IPCC) project that without serious efforts to halt or reverse the trend towards higher atmospheric CO_2 concentrations, the increasing potency of the greenhouse effect will have a dramatic impact on global climate - estimates place the expected increase in global average temperature over the next century at 2-5°C, depending on the predicted changes in population, total energy use and other factors which may influence CO_2 emissions.

1.1.2 Finite Fossil Fuel Resources

Widespread use of fossil fuels throughout the last three hundred years has driven an unprecedented increase in living standards, technology and wealth. Initially, the use of coal as a combustion fuel was the primary consumption route, and coal-fired power stations remain the most significant global energy source.[7] However, the last century has seen a massive expansion in the use of oil-based fuels, particularly for transportation applications.

The primary advantages of oil-derived hydrocarbon fuels over all current alternatives relate to their practicality - most common fuels are liquid at room temperature allowing for ease of transport and storage, provide much greater energy density than electrochemical or capacitive devices, and have a range of properties such as viscosity, flash point and autoignition temperature which can be tuned by altering the choice of hydrocarbon chain length and degree of branching. These features allow a suitable fuel to be chosen to meet a wide range of usage requirements. For example, while automotive, aviation and maritime propulsion systems all make use of liquid hydrocarbon fuels, each application has a distinct requirement for performance, as well as very different economic influences.

Many alternative energy sources are currently under investigation, with an emphasis on renewable technologies such as solar and wind power. Nuclear power, a proven alternative energy source already in widespread use, could provide an even more significant contribution to meeting our energy demands in the future. Unfortunately, concerns over safety and security may limit the increased adoption of nuclear energy technologies. Each version of nuclear or renewable energy technology has a distinct set of advantages and drawbacks, but all share the common restriction that they are only viable for large-scale, static deployment rather than localised or mobile applications. The use of hydrocarbon fuels in transport applications cannot easily be reduced by simply transitioning to renewable energy sources, as both the current energy storage solutions (primarily Li-ion batteries) and distribution infrastructure are ill-equipped for such a dramatic shift.

A final point to consider is that even if all energy were provided by renewable sources, and all transport made use of CO_2-neutral energy of some kind, vast quantities of hydrocarbons would still be required to meet the world's demand for plastics and other carbon-based chemical products. As the global population grows and average living standards increase, the demand for these materials can only climb further.

1.1.3 The Methanol Economy

Given the drawbacks to continued fossil fuel usage already described, it is clear that a transition to widespread usage of a renewable chemical fuel is highly desirable, and ultimately likely to be unavoidable. The use of CO_2 as a reactant, particularly if the gas can be captured from the atmosphere, would eventually allow us to manage our greenhouse gas emissions and slow, halt or potentially reverse some of the effects of climate change. Such a scenario would also provide the potential for fuel security to any nation with the capability to produce large quantities of energy from renewable sources, with fuel synthesis and CO_2 emission from transport applications forming a closed loop. The synthetic fuel would also play a role in the management of unpredictable energy production from renewable sources such as wind and solar, allowing excess fuel to be produced when grid demand for electricity is low and generation is high, and spare fuel to be used in cases where electricity production falls below demand.

Olah et al. refer to the scenario described here as the "Anthropogenic Chemical Carbon Cycle", and along with many others,[1–3,8–10] advocates methanol as the synthetic fuel of choice. The production of methanol from CO_2 and H_2 presents an attractive solution. Methanol may be used directly as a fuel (either through combustion or within a direct methanol fuel cell), converted to dimethyl ether for use as a direct replacement for diesel fuel,[11] or processed to form heavier, more valuable hydrocarbon species.

Given that methanol has around half the volumetric energy density of current automotive fuel, and with around 31 billion barrels of petroleum consumed each year, methanol production would need to be scaled from the current value of 65 million tonnes per year to around 7.8 billion tonnes per year - a 120-fold increase. These figures should serve to emphasise the urgent need for the development of catalysts and new reaction processes which can enable an optimally efficient CO_2 recycling process.

1.2 Recycling and Sequestration of CO_2

The challenges associated with using CO_2 as a chemical reactant in a renewable manner can broadly be divided into "capture" and "catalysis" fields. CO_2 capture processes may also be subdivided into those intended for permanent sequestration of the gas and those where the adsorbant is expected to undergo multiple capture/release cycles, effectively removing the gas from one source and concentrating it in another location.

Given the limitations of both CO_2 recycling and sequestration, an optimal solution may requre both CCS and recycling of CO_2, as well as increased adoption of renewable energy sources in cases where energy density and ease of transport are not critical factors.

1.2.1 CO_2 Capture

Descriptions of CO_2 capture can broadly be divided into those focused on concentrated sources such as flue gases from coal-fired power stations, and those concerned with the capture of atmospheric CO_2. The latter allows for much greater flexibility in both the location and scale of the recycling process, with the disadvantage that capture of CO_2 from a lower concentration source carries a correspondingly higher energetic cost.[12,13] A further subdivision is possible depending on the goal of the CO_2 capture, with different technologies being favoured for permanent sequestration versus temporary capture as part of a recycling process.

The simplest materials under consideration for CO_2 capture applications are the alkali earth oxides MgO and CaO. Exposure to CO_2 allows for the formation of carbonates, $MgCO_3$ and $CaCO_3$, which may be subsequently decomposed by thermal treatment to recover the metal oxide and CO_2.[14,15] Unfortunately, while these materials are highly abundant and consequently low cost, the energy input required to achieve acceptable absorption and desorption rates is excessively high. Such materials are therefore only considered viable for permanent sequestration, where the carbonate is stored underground to prevent any ongoing environmental impact from the CO_2. Sequestration has the advantage of being a much simpler process than recycling, requiring fewer additional reactants and being applicable to lower CO_2 concentrations. It is also possible to perform CO_2 sequestration by simply compressing the purified gas and pumping it into an isolated location, such as an empty oil or gas well. However, sequestration has the obvious drawback that it does not contribute to solving the problem of fossil fuel scarcity. Widespread use of carbon capture and storage (CCS) processes without recycling would therefore be dependent on the availability of viable renewable energy alternatives to reduce the need for fossil fuels in static energy generation, a significant improvement in battery or hydrogen storage technologies for transport applications, and alternative hydrocarbon sources (such as biomass) for the synthesis of more complex hydrocarbon products such as solvents and pharmaceuticals. Given the magnitude of each of these challenges, it is safe to assume that the synthesis of hydrocarbon fuels from captured CO_2 will very probably play a significant role in managing our future energy demands.

For CO_2 capture from high-concentration sources, some of the most promising materials include aqueous alkanolamine solutions, which undergo a reaction to form carbonates, and solid metal organic frameworks (MOFs), which allow CO_2 to be adsorbed within the framework. Each have their own limitations, such as the requirement for high CO_2 pressures in the MOF case, and are not transferrable to direct air capture (DAC) applications. Instead, simple hydroxides (NaOH, KOH, $Ca(OH)_2$) are the preferred DAC materials currently under investigation, allowing for either thermal or chemical regeneration cycles.[3]

1.2.2 Methanol Synthesis

Processes designed to recycle CO_2 generally have the aim of producing a short-chain hydrocarbon, such as methanol, which can either be used in subsequent reactions to form higher value products, or used directly as a fuel. In order for methanol to considered a viable energy carrier, the CO_2 used in its production must form part of a closed cycle. Capture of CO_2 at the point of its generation would be the most efficient choice due to the increased concentration, however the technical challenge posed by the need for a lightweight capture and recycling device within every vehicle makes this concept impractical. Further work is therefore required to find a suitable direct air capture process.

Most methanol is produced from the reaction of CO and H_2, a mixture known as synthesis gas, or syngas:

$$\mathrm{CO + 2\,H_2 \leftrightharpoons CH_3OH} \tag{1.1}$$

There is evidence to suggest that the mechanism of this process involves the interconversion of CO and CO_2 via the water-gas shift reaction (WGSR):[16]

$$\mathrm{CO + H_2O \leftrightharpoons CO_2 + H_2} \tag{1.2}$$

This may then be followed by the reaction of CO_2 and H_2 to produce methanol:

$$\mathrm{CO_2 + 3\,H_2 \leftrightharpoons CH_3OH + H_2O} \tag{1.3}$$

This mechanism would allow for the direct synthesis of methanol from CO_2 and H_2 given the correct reaction conditions - such a process was used on a commercial scale in the 1920s and 1930s. However, most current methanol synthesis is performed using syngas as shown in reaction 1.1.

As has already been suggested, a crucial development necessary for the increased production of methanol to meet the demands of its use as our primary chemical energy carrier is the design of a low-cost catalyst system with excellent cycling properties, comprised of abundant components. The most widely studied catalyst for methanol synthesis from both CO and CO_2 is $Cu/ZnO/Al_2O_3$.[17–21] This catalyst was first developed for methanol production by ICI in the 1960s and remains in use today. Significant amounts of experimental work has been performed since then to optimize the catalyst design, such as finding the effect of metal coverage and choice of oxide support.

Combined experimental and theoretical studies have suggest that the copper component of the catalyst is of particular importance where the reactant gas stream contains CO_2, with ZnO/Al_2O_3 becoming poisoned by the addition of CO_2.[22] The authors note, however, that while pure syngas is necessary to achieve reasonable methanol production rates on the oxide-only catalyst, the reaction for the Cu-loaded catalyst has been shown by isotopic labelling to proceed *via* an alternate mechanism which includes CO_2 as an active component.[16] While this and other work has highlighted the importance of Cu species for methanol selectivity and high turnover frequencies, others stress the synergistic behaviour of the copper and zinc.[17,23]

Other catalyst systems besides those based on the industry standard have also been studied, including gold and other noble metals supported on oxide surfaces.[24–26] The results of these studies verify the important role the metal oxide plays in catalysis, describing how careful choice of an acidic or basic oxide, such as TiO_2 or MgO respectively, alters both the activity and selectivity towards methanol production. Despite their impressive performance, the high cost of catalysts based on noble metals means that they are unlikely to make a significant contribution to the increased adoption of CO_2 recycling.

Alternative oxides such as Ga_2O_3, ZrO_2 and Cr_2O_3 have been considered and found to be more stable than standard commercial catalysts. The $Cu/ZnO/Ga_2O_3$ catalyst showed particular promise, maintaining a highly disperse coverage of copper and retaining the activity of ZnO, which is understood to aid the catalytic process by inhibiting the reverse water-gas shift reaction.[18]

1.3 Related Reactions and Processes

Besides the CO_2 sequestration and recycling steps already described, a number of other processes are relevant to the discussion of a post-fossil fuel economy. These include the production of other starting materials necessary for methanol synthesis, as well as reactions which can convert the methanol into other hydrocarbon products which are suitable for alternative applications besides use directly as fuel.

Hydrogen Production

The most significant barrier to widespread adoption of methanol as a renewable fuel besides the capture of CO_2 is the production of H_2. Currently, H_2 is widely produced from natural gas via the steam methane reforming (SMR) reaction:

$$\mathrm{CH_4 + H_2O \leftrightharpoons CO + 3\,H_2} \tag{1.4}$$

Other reactions which contribute to the production of hydrogen include the partial oxidation of methane (1.5), dry reforming of methane (1.6) and methane decomposition (1.7):

$$\mathrm{CH_4 + \tfrac{1}{2}\,O_2 \leftrightharpoons CO + 2\,H_2} \tag{1.5}$$

$$\mathrm{CH_4 + CO_2 \leftrightharpoons 2\,CO + 2\,H_2} \tag{1.6}$$

$$\mathrm{CH_4 \leftrightharpoons C(s) + 2\,H_2} \tag{1.7}$$

As all of these routes require the consumption of fossil fuels, alternative methods will eventually be required. The solution most likely to achieve widespread use based on current technology is the electrolysis of water, directly forming H_2 and O_2:

$$\mathrm{H_2O \leftrightharpoons 2\,H_2 + \tfrac{1}{2}\,O_2} \tag{1.8}$$

Electrochemical water splitting is a relatively expensive process, and is heavily dependant on the price of electricity. Cost-effective use of this method as part of a CO_2 recycling process will therefore depend on the availability of cheap sources of renewable energy, but has the additional benefit that the pure O_2 formed as a byproduct also has economic value.

Dimethyl Ether Synthesis

Dimethyl ether (DME) may play a role in a methanol-based anthropogenic carbon cycle as an alternative combustion fuel. DME can act as a direct replacement for diesel fuel in automotive applications.[11] DME is synthesised by the dehydration of methanol, a process which may be performed independently, using methanol as the feedstock, or as part of a dual reaction process to convert syngas to DME without isolation of the methanol intermediate:

$$2\,\mathrm{CH_3OH} \leftrightharpoons \mathrm{CH_3OCH_3} + \mathrm{H_2O} \tag{1.9}$$

Methane Production

As well as their combination to form methanol, captured CO_2 and H_2 may undergo a methanation reaction:

$$\mathrm{CO_2} + 4\,\mathrm{H_2} \leftrightharpoons \mathrm{CH_4} + 2\,\mathrm{H_2O} \tag{1.10}$$

This process may prove useful in replacing current natural gas usage with a synthetic fuel - in particular, such usage would allow for continued distribution of gas for cooking and heating applications using existing infrastructure.

Oxidative Coupling of Methane

In the short term as we progress from fossil fuels to a synthetic alternative, it is likely that more widespread use of natural gas reserves will become necessary. The oxidative coupling mechanism is widely thought to proceed *via* homolytic

C-H bond breaking, followed by a radical mechanism to form ethane as the initial C_2 product. The ethane then undergoes an oxidation reaction to give ethene, the product usually desired.[27]

$$2\,\mathrm{CH_4} + \tfrac{1}{2}\,\mathrm{O_2} \leftrightharpoons \mathrm{C_2H_6} + \mathrm{H_2O} \tag{1.11}$$

The method of C-H bond activation is somewhat controversial, with Lundsford and others[28] suggesting that electron holes at the catalyst surface, for example $O^{\bullet -}$ sites in Li-doped MgO. Others, including Kwapien et al., suggest that the monovalent dopant does not play such a direct role in the catalyst activity, and favour a model where the C-H bond cleavage occurs at a low-coordinated surface site with no other chemical modification, such as a corner or step edge.[29]

1.4 Computational Modelling of CO_2 Recycling

As the work reported in this thesis relates to computational studies of the interaction between CO_2 and metal oxide surfaces, an overview of previous work on insights into CO_2 recycling will now be presented. Work described here relates specifically to systems where methanol synthesis is the target application. Other studies, such as those concerned with CO_2 adsorption or the formation of important active sites, will be discussed in Chapters 3, 4, 5 and 6. In particular, any studies where the specific details of the published results have an impact on the interpretation of the work presented in this thesis are discussed at an appropriate point within the results chapters rather than as part of a literature summary.

A number of studies have been performed in order to investigate the mechanistic details of the methanol synthesis reaction on the commercial $Cu/ZnO/Al_2O_3$ catalyst.[30–32] These results highlight the role played by hydrogenation of the oxide surface during the reaction, as well as providing evidence for the coexistence of Cu^+ and Cu^0 species within the adsorbed metal clusters.

Due to the experimental evidence suggesting that CO_2 conversion to methanol greatly benefits from the presence of ZnO within the catalyst, a significant amount of research has focused on the oxide material without adsorbed metal clusters.[17,23,33–38] Of particular interest are electron-rich defect sites which can allow for the formation of ${CO_2}^-$, which has been identified as a key intermediate in the reaction process by which methanol is formed. These are complemented by work on purely metallic copper and zinc systems,,[32,39,40] as well as nickel and a number of noble metals.[41–43]

Finally, studies have been performed to investigate materials with structures other than those of bulk metal oxides - for example, Mo_6S_8 clusters[44] and zeolites.[45] While the former are unlikely to attract any commercial interest, the latter are already widely used catalysts for hydrocarbon chemistry.

Chapter 2

Computational Methods

The majority of the work presented here has made use of a hybrid quantum mechanical-molecular mechanical (QM/MM) methodology implemented within the ChemShell code.[46] This technique allows for the detailed examination of the electronic structure at a catalyst active site, while maintaining flexibility due to long-range relaxation effects.

Each of the independent components of a QM/MM calculation will be described along with an overview of the specific methods which are relevant to the work performed, followed by a discussion of the important considerations required when the two levels of theory are combined. In Section 2.1, the various electronic structure methods used as part of this work are described, and in Section 2.2 the key aspects of molecular mechanics calculations are discussed. Section 2.3 outlines the details of the QM/MM implementation used within ChemShell. Finally, 2.4 provides a description of the specific hardware and software used to obtain the results presented within this thesis.

2.1 Quantum Mechanics

The fundemental basis for electronic structure calculations is the desire to solve the time-independent Schrödinger equation:

$$\mathcal{H}\psi(r) = E\psi(r) \tag{2.1}$$

Here, E is the energy of the system and $\mathcal{H}$ is the Hamiltonian operator, which can be decomposed into kinetic and potential energy components to give:

$$\left\{-\frac{\hbar^2}{2m}\nabla^2 + \mathcal{V}\right\}\psi(r) = E\psi(r) \tag{2.2}$$

An alternative expression, more easily applicable to a real system, is to express the Hamiltonian in terms of the component interactions it describes:

$$\hat{\mathcal{H}} = \hat{T}_e + \hat{T}_n + \hat{V}_{ee} + \hat{V}_{nn} + \hat{V}_{ne} \tag{2.3}$$

$\hat{T}_e$ and $\hat{T}_n$, the kinetic energies of the electrons and nuclei are defined with respect to the total number of electrons N with mass m_e and the total number of nuclei M with mass M_i, as:

$$\hat{T}_e = -\sum_i^N \frac{\hbar^2}{2m_e}\nabla^2(r_i) \tag{2.4}$$

$$\hat{T}_n = -\sum_i^M \frac{\hbar^2}{2M_i}\nabla^2(R_i) \tag{2.5}$$

$\hat{V}_{ee}$ and $\hat{V}_{nn}$ describe the pairwise contributions of Coulombic electron-electron and nucleus-nucleus interactions respectively:

$$\hat{V}_{ee} = \sum_i^N \sum_{j>i}^N \frac{e^2}{4\pi\epsilon_0|r_i - r_j|} \tag{2.6}$$

$$\hat{V}_{ee} = \sum_i^M \sum_{j>i}^M \frac{Z_i Z_j e^2}{4\pi\epsilon_0|R_i - R_j|} \tag{2.7}$$

$\hat{V}_{ne}$ represents the electron-nucleus interactions, and is defined as:

$$\hat{V}_{ne} = \sum_i^M \sum_j^N \frac{Z_i e^2}{4\pi\epsilon_0|R_i - r_j|} \tag{2.8}$$

Exact solutions to the Schrödinger equation are only accessible for a limited number of simple systems, and so a series of approximations must be applied until a computationally tractable problem is formulated. The first of these is the Born-Oppenheimer approximation, which allows us to consider the motion of electrons and nuclei to be decoupled due to the significant difference in their masses. This approximation allows us to treat the total energy of the system as a simple sum of electron and nuclear energies, where the electron energy is a function of kinetic energy and the potential energy due to the electrostatic fields within the system, and the nuclear energy is the result of electrostatic repulsion between the nuclei.

Even with the consideration of nuclear motion excluded, the Schrödinger equation remains an N-body problem, which needs to be simplified further before application to real chemical systems is possible. Within the Hartree approximation, the wavefunction of the whole system is described as a product of single-particle wavefunctions, with each electron described in terms of the average potential due to the presence of other electrons rather than treating each interaction explicitly. Constructing an accurate potential in this manner requires the use of an iterative procedure, where an initial guess is used to obtain a solution, and the solution is then used to repeat the calculation to improve the effective potential. Each iteration should improve the accuracy of the result obtained, until eventually a self-consistent solution is achieved. This self-consistent field (SCF) approach is a common feature of most widely used electronic structure calculation methods, which continue to make use of the Born-Oppenheimer and Hartree approximations along with more modern developments to achieve accurate descriptions of systems containing thousands of electrons.

2.1.1 Hartree-Fock Theory

The Hartree-Fock approach builds upon Hartree theory by including the effects of electron spin, allowing calculations to more closely resemble a real chemical system. For a simple two-particle case, the Hartree product described above can be expressed as:

$$\Psi(\mathbf{x}_1, \mathbf{x}_2) = \chi_1(\mathbf{x}_1)\chi_2(\mathbf{x}_2) \tag{2.9}$$

for particles χ_i in positions $\mathbf{x}_i$. The Pauli exclusion principle requires the wavefunction to be antisymmetric with respect to an exchange of particles, i.e:

$$\Psi(\mathbf{x}_1, \mathbf{x}_2) = -\Psi(\mathbf{x}_2, \mathbf{x}_1) \tag{2.10}$$

This equality is not satisfied in calculations using only the Hartree approximation, and so the total wavefunction can no longer be expressed in terms of a product of particle wavefunctions. Instead, the system is described by a Slater determinant Ψ^{HF} of N spin orbitals:

$$\Psi^{HF} = \frac{1}{\sqrt{N!}} \begin{vmatrix} \chi_1(\mathbf{x}_1) & \chi_2(\mathbf{x}_1) & \cdots & \chi_N(\mathbf{x}_1) \\ \chi_1(\mathbf{x}_2) & \chi_2(\mathbf{x}_2) & \cdots & \chi_N(\mathbf{x}_2) \\ \vdots & \vdots & \ddots & \vdots \\ \chi_1(\mathbf{x}_N) & \chi_2(\mathbf{x}_N) & \cdots & \chi_N(\mathbf{x}_N) \end{vmatrix} \tag{2.11}$$

The Slater determinant form enforces the Pauli exclusion principle, causing the total wavefunction to evaluate to zero in cases where two particles have identical spatial and spin coordinates, and to satisfy equation 2.10 in cases where the coordinates of two particles are exchanged.

In order to apply the Hartree-Fock method to a real system, a finite set of basis functions must be introduced to describe the spatial component of the coordinates for each particle. A set of K spatial functions provides 2K spin orbitals, half being assigned to each of the opposing electron spins, referred to as α and β. Within a real calculation, these functions are specified as part of a *basis set*, described in more detail in Section 2.1.3. As the number of spin orbitals increases, the solution to the Hartree-Fock equation approaches the *Hartree-Fock limit*, which would correspond to an infinitely large basis set. The energy difference between the HF limit and the exact solution to the Schrödinger equation consists of contributions which are neglected due to the mean-field treatment of single-particle wavefunctions, and is referred to as the *correlation energy.* Including electron correlation effects requires the use of much more computationally expensive methods, which are not discussed here. A simpler, if less accurate approach is provided by *density functional theory.*

2.1.2 Density Functional Theory

The Hartree-Fock method described above is a wavefunction-based method, the formulation of which can be derived directly from the Schrödinger equation. Density Functional Theory (DFT) is an alternative electronic structure calculation method based on the assumption that the properties of a system, including its ground-state wavefunction Ψ_0, may be determined from the ground-state spatially-dependent electron density $\rho(r)$:

$$\Psi_0 = \Psi[\rho(r)] \tag{2.12}$$

The ground state energy is a functional of the ground-state density, with the wavefunction having kinetic and potential energy components as described earlier. For a given mean-field potential $V(r)$, the energy of the ground state is:

$$E_0 = E[\rho(r)] = \int V(r)\rho(r)dr + F[\rho(r)] \tag{2.13}$$

$F[\rho(r)]$ is a functional with unknown form. The Kohn-Sham method concentrates our ignorance of $F[\rho(r)]$ into a single term $E_{XC}[\rho(r)]$, by replacing the real system with a ficticious set of non-interacting electrons having the same density:

$$E[\rho(r)] = T_e[\rho(r)] + V_{ne}[\rho(r)] + V_{ee}[\rho(r)] + E_{XC}[\rho(r)] \tag{2.14}$$

The components T_e, V_{ne} and V_{ee} can all be calculated for the independent electrons analogously to the Hartree method, with the extra term $E_{XC}[\rho(r)]$ corresponding to the electron exchange and correlation contributions, which would otherwise be neglected from DFT. A reasonable approximation to E_{XC} allows for the calculation of the ground-state density $\rho(r)$, and therefore the ground-state energy E_0, via an iterative process in a similar vein to the Hartree and Hartree-Fock approaches.

The key challenge in DFT is therefore the generation of reasonable representations of E_{XC}. The earliest such method to achieve widespread use is the Local Density Approximation (LDA), which treats the system as locally homogeneous by using the exchange correlation energy density for a uniform electron gas $\epsilon_{XC}^{LDA}(\rho(r))$, which is known to a high degree of precision.[47,48]

$$E_{XC}^{LDA}[\rho(r)] = \int d^3r\rho(r)\epsilon_{XC}^{LDA}(\rho(r)) \tag{2.15}$$

LDA favours electron densities which are more diffuse than the exact result, leading to a tendency towards overestimating binding energies, underestimating phonon frequencies and elastic constants, and giving a poor representation band gaps, leading to predictions of the metallic/semiconducting/insulating character of materials.

Improvements to LDA can be made by incorporating gradient corrections to $\epsilon_{XC}^{LDA}(\rho(r))$, a method referred to as the Generalised Gradient Approximation (GGA):

$$E_{XC}^{GGA}[\rho(r)] = \int d^3r\rho(r)\epsilon_{XC}^{LDA}(\rho(r))F(\rho(r), \nabla\rho(r)) \tag{2.16}$$

The gradient correction $F(\rho(r), \nabla\rho(r))$ is applied in a number of different ways, with experimental data often used to provide empirical parameters. GGA provides improved binding energies and molecular geometries, and offers a small improvement in band gap predictions.

Both LDA and GGA methods give a poor description for localised electronic states such as d- and f-orbitals due to electron self-interaction, whereby the coulombic interaction between different regions of electron density resulting from a single electron is not cancelled. This effect leads DFT to favour solutions where electrons are artificially delocalised.

Hartree-Fock calculations do not exhibit this self-interaction problem as the formulation of the HF method gives an exact exchange contribution, while DFT provides only an approximation. Due to the reduced computational complexity, (and correspondingly lowered computational expense) of DFT calculations relative to HF and other wavefunction-based methods, significant effort has been expended in order to improve the results provided by DFT, giving a range of options to improve the treatment of localised states, dispersion interactions and other areas where DFT results are non-optimal.

The most promising improvement to DFT is the application of hybrid functionals, which improve the accuracy of the exchange-correlation contribution by including a component of the exact exchange from the Hartree-Fock method. The general form of a hybrid exchange-correlation functional is given by:

$$E_{XC}^{Hyb} = (1-a)E_X^{DFT} + aE_X^{HF} + E_C^{DFT} \tag{2.17}$$

In this simple case, the parameter $0 < a \leq 1$ specifies the proportion of HF exchange to be included. More complex functionals include separation of the exchange and correlation into short and long-range components, or the mixing of LDA and GGA contributions for the components not taken from Hartree-Fock results. Many different functionals are available, both with and without the inclusion of Hartree-Fock exchange. The functionals are often differentiated by their fitting procedure, with some having emphasis on accuracy at the expense of "ab-initio" character. Functionals are often targeted to a particular subset of materials such as small organic molecules or solid metal oxides, with the original functional fitting process specifically tuning the representation of these materials at the expense of generalised accuracy.

In principle, hybrid functionals allow for much greater accuracy than LDA or GGA-based DFT calculations, although this improved accuracy comes with a penalty to the computational performance: DFT calculations generally scale with the number of electrons as $\mathcal{O}(N^3)$, while the Hartree-Fock calculation required to provide the exact exchange contribution scales as $\mathcal{O}(N^4)$. Additionally, the wide variety of hybrid functionals, each with different fractions of HF exchange and other empirically tuned parameters, makes the applicability of a given functional somewhat narrower than LDA and GGA, which are more grounded in fundamental electronic structure theory.

An alternative to the use of hybrid functionals, which provides some of the same benefits with regard to improving the treatment of localised states with a less severe computational cost, is the use of a Hubbard U correction. This method involves the application of a penalty function to the hybridisation of any orbitals which are likely to suffer heavily from the effects of electron self-interaction. The natural tendency for LDA and GGA towards delocalised solutions is therefore counterbalanced somewhat, although the magnitude of the penalty function remains as an empirical parameter which must in principle be tuned independently for each material being studied.

Besides the self-interaction problem, the most notable shortcoming of DFT is the lack of any component which accurately reproduces dispersion forces. Rather than modifying the underlying electronic structure calculation to account for the missing interactions, the most common approach to introducing dispersion into DFT is the application of a corrective energy term which is a simple function of interatomic distances.

Moving beyond DFT and Hartree-Fock methods, higher accuracy may be achieved using techniques which include the effects of excited states within the calculation. The most widespread examples of this are perturbation theory methods such as MP2, and coupled-cluster calculations. Use of these methods is limited to cases where a very small number of atoms are present, as both scale particularly poorly - MP2 calculations exhibit $\mathcal{O}(N^5)$ scaling, while CCSD(T) (the “gold standard” for coupled cluster calculations) exhibits $\mathcal{O}(N^7)$ scaling.

2.1.3 Implementation

The methods described thus far provide a set of frameworks which are widely used to perform electronic structure calculations. For each case, certain variable parameters such as the choice of exchange-correlation functional within density functional theory may be used to control the overall predictive behaviour of the calculation, while others such as the degree of mixing of old and new solutions as part of the self-consistent field procedure may help with convergence, allowing the ground-state solution to be indentified more quickly.

The most important variable parameters in the majority of calculations are those directly related to the atoms of interest. When performing quantum mechanical calculations, the relevant data to differentiate between atoms (besides their mass, which is usually a constant value built-in to the software being used) must be captured within a set of inputs. Often, the atomic data takes the form of a *basis set*, which is sometimes used in conjunction with an *effective core potential*. Each of these is a data set which has been pre-optimised for a set of target chemical species, usually chosen due to the availability of high-quality experimental data for comparison with the calculated results as well as their ability to account for a wide range of chemical behaviour within electronic structure calculations. Basis sets and effective core potentials may be chosen to provide fast, qualitative results or high levels of accuracy with a larger computational expense, depending on the goals of the study.

Basis Sets

A basis set may be defined within the context of electronic structure calculations as a collection of functions which may form molecular orbitals through their linear combination. A basis set may take a variety of forms, with the most common being atom-centred functions, widely used for molecular calculations in a vacuum. For systems containing periodic boundary conditions such as bulk crystals, plane-waves are another common choice. Alternatives, such as wavelets and sinc functions, are increasing in popularity due to their favourable scaling properties.[49] All calculations described within this thesis were performed using atom-centred basis sets, and so these will be the focus of the remaining discussion.

The basis set which most closely and simply represents the behaviour of electrons within atoms is one based on Slater functions, which take the form:

$$\phi^{SF}(r) = Nr^{(n-1)}e^{-\zeta r} \tag{2.18}$$

N is a normalisation factor, n is the principal quantum number of the electron of interest and ζ is the orbital exponent. These functions accurately reproduce both the nature of the wavefunction near the atomic nucleus and the exponential decay at long range.

While Slater-type orbital (STO) basis sets are the most suitable choice for some applications,[50] it is usually preferrable to sacrifice some of the accuracy provided by these functions in exchange for greater computational speed. Gaussian type orbital (GTO) basis sets achieve this goal as a result of the Gaussian Product Theorem, which states that the product of two Gaussian functions centred on different points is equal to the finite sum of Gaussians centred on a third point along the axis between them. Exploiting the Gaussian Product Theorem gives a significant increase in performance when compared with a calculation using the same number of Slater functions. Gaussian functions have the general form:

$$\phi^{GF}(r) = Ne^{-\alpha r} \tag{2.19}$$

N is a normalisation factor and α is the orbital exponent. The primary drawback to GTO basis sets is the need to combine multiple functions to reproduce the accuracy of an STO basis set. Fortunately, more accurate basis functions may easily be expressed as a linear combination of Gaussian functions, termed a contracted Gaussian function:

$$\phi^{CGF}(r) = \sum_{i=1}^{L} d_i \phi^{GF}(r) \tag{2.20}$$

L is the length of the contraction, or the number of primitive Gaussian functions to be included, and d_i is a contraction coefficient. In a real basis set, it is these parameters which are tuned to give the desired balance between accuracy and performance - assuming d_i has been adequately fitted for each Gaussian function used, increasing the value of L will allow the basis set to produce results which are closer to the ideal STO case, while consequently increasing the computational expense.

Effective Core Potentials

Thus far, all discussions have assumed that quantum mechanical calculations explicitly include the effect of every electron present in the system being studied. In reality, however, many of the inner electrons contribute very little to the chemical behaviour observed. Given that an all-electron model would require a significant expenditure of computational resources, it is often preferable to combine the inert core electrons with the atomic nucleus to form an effective core potential, or ECP.

Using an ECP provides a significant reduction in computational costs while usually only causing a marginal reduction in the accuracy of the calculation. In fact, the use of an ECP may sometimes improve the accuracy due to the inclusion of relativistic effects within the potential; in an all-electron calculation, relativistic corrections for heavy elements would generally prove too costly to be included, but when an ECP is used the expense associated with these corrections is shifted from the calculation being performed by the end user to the one in which the ECP is first fitted. The general form of an ECP is equivalent to that of a Gaussian basis set given in equation 2.19, with multiple contracted functions used to give an optimum representation of the effective potential generated by the nucleus and core electrons.

2.2 Molecular Mechanics

While electronic structure calculations provide access to detailed *ab initio* information for chemical systems, their high computational cost makes them ill-suited to cases where the dynamics of a large number of atoms are more important than the behaviour of individual electrons. Molecular mechanics calculations generally scale better than $\mathcal{O}(N^3)$ (between $\mathcal{O}(N^2)$ and $\mathcal{O}(N)$ in most cases), and scaling is with respect to the number of atoms rather than the number of electrons, as is the case for quantum mechanical calculations. This significant improvement in performance allows for the study of systems containing thousands of atoms with relative ease.

Calculations falling under the umbrella of molecular mechanics exploit the fact that in most cases where chemical bonds are not being broken or formed, electrons and nuclei can be condensed to a single unit to give a representation of the whole atom, which can in turn be subjected to interatomic forces in order to reproduce a real chemical environment.

Molecular mechanics calculations operate based on a pre-defined set of functions and parameters which have been fitted to either experimental or *ab initio* results. These parameters may be designed to give a reasonable representation of a wide range of chemical systems, or alternatively may be optimised to reproduce a particular system of interest to a high degree of accuracy. Collectively, the functions used to describe interactions within a molecular mechanics calculation are termed *interatomic potentials.*

2.2.1 Interatomic Potentials

The most significant contribution to a molecular mechanics calculation is generally the Coulombic term between charged species, given by:

$$U_{ij}^{coulomb} = \frac{q_i q_j}{4\pi\epsilon_0 r_{ij}} \tag{2.21}$$

The charge q may be the formal charge of an ion, or a partial charge estimated based on *ab initio* calculations.

In addition to the Coulomb term, the inclusion of additional interactions is necessary in order to accurately simulate the presence of chemical bonds and van der Waals forces. The simplest of these are two-body terms which aim to include the effects of dispersion forces which dominate at long distances, Pauli repulsion at short distances and covalent bonding at intermediate distances.

For generally non-bonding species such as the noble gases, only dispersion and Pauli repulsion need be included. The Lennard-Jones potential includes terms to reproduce each of these, with tunable parameters to set the optimum interatomic distance and maximum attractive force:

$$U_{ij}^{LJ} = \frac{C_m}{r_{ij}^m} - \frac{C_6}{r_{ij}^6} \tag{2.22}$$

The value of m determines the strength of the Pauli repulsion component, and generally lies in the range 9-12. It is often desirable to truncate the attractive component of the potential at very long distances in order to reduce the computational expense.

For ionic species, the non-Coulombic components of the interaction are generally better described by the Buckingham potential:

$$U_{ij}^{Buckingham} = Ae^{-\frac{r_{ij}}{\rho}} - \frac{C_6}{r_{ij}^6} \tag{2.23}$$

The exponential form of the repulsive part of the Buckingham potential is conceptually a better fit for the real Pauli repulsion than the r^m term used in the Lennard-Jones potential.

The Morse potential aims to reproduce the behaviour of covalent bonding interactions, and includes terms to set the desired dissociation energy (D_e) and equilibrium bond distance (r_0), as well as a term to alter the “width” of the potential energy well:

$$U_{ij}^{Morse} = D_e[(1 - e^{-a(r-r_0)})^2 - 1] \tag{2.24}$$

While the interatomic potentials described here are the most commonly used, many alternatve forms exist for 2-body interactions as well as higher order terms to reproduce bond angles, torsion effects and other more complex interactions.

2.2.2 Shell Model

The methods described thus far are generally sufficient when modelling systems where the motion of electrons and nuclei can be treated as a single unit, but in many systems the effects of polarisability must be included. In such cases, an appropriate compromise between rigid atoms and electronic structure calculations is the division of atomic species into *core* and *shell* components.[51] Each is given a charge (with the sum being equal to the charge of the rigid species), and is no longer subject to the same set of interatomic potentials. The motion of the core and shell components is coupled by the application of a spring-like potential:

$$U_{ij}^{spring} = \frac{1}{2}k_2 r^2 + \frac{1}{24}k_4 r^4 \tag{2.25}$$

Electrostatic interactions between the core and shell of the same atom are screened out to avoid the generation of an infinite Coulombic term. Also, it is usual to apply other interatomic potentials such as Buckingham and Lennard-Jones between the shell components of different species, leaving only interatomic Coulomb potentials and intraatomic spring terms acting on the core components. The shell model has been widely and successfully used in modelling ionic systems.

2.3 QM/MM Embedding

The use of a quantum mechanical/molecular mechanical hybrid calculation scheme allows for the inclusion of high-level electronic structure methods on a core subset of atoms while, maintaining a realistic representation of the surrounding environment.[52–54] QM/MM calculations are of particular importance in cases where the system being studied displays a large degree of flexibility, such as solvated organic molecules and catalytic active sites, especially enzymes. The ChemShell environment extends the QM/MM framework to include solid-state materials such as metal oxides and zeolite frameworks. The key advantage provided by the embedding scheme is the ability to study defects and adsorption processes in isolation, rather than under periodic doundary conditions as is more common in purely QM-based studies.

Most QM/MM calculations are *additive*, in that the total energy of the system is determined by taking the sum of separate QM, MM and interface terms. An alternative is the *subtractive* formulation, where an MM calculation is first performed on the whole cluster, followed by QM and MM calculations on the inner region in order to first subtract the MM contribution for these atoms, and subsequently add in the QM component.

Three methods for QM/MM embedding are accessible within ChemShell. The simplest is *mechanical embedding*, where the interaction between QM and MM atoms has no electrostatic component and is accounted for soley by interatomic potentials. In *electrostatic embedding*, the QM calculation may be polarised due to the influence of charges on MM centres. Finally, *polarised electrostatic embedding* builds upon the previous method by allowing the QM charge density to induce polarisation of the MM atoms, although this requires the use of the shell model within the MM calculation.

Two distinct boundary setups are available to handle the interface between QM and MM parts of the calculation, with the ideal choice being dependent on the type of bonding present in the material being studied. For covalently bonded materials such as zeolites, the QM and MM components are coupled via the placement of pseudoatoms on the bonds broken by the interface. The charges on atoms near the boundary are shifted in order to prevent unrealistic polarisation of the QM calculation, and forces on the link atoms are transferred to real atoms as part of any geometry optimisation necessary. For ionic materials, large core pseudopotentials are placed on cation sites surrounding the QM calculation in order to prevent electron density spilling onto the point charges in the MM region.

All calculations presented in this work are focused on ionic materials, and so use an additive coupling scheme with polarised electrostatic embedding and pseudopotentials on cations at the QM/MM boundary.

The construction of a QM/MM cluster for use within ChemShell is a multistage process. For solid-state materials, the first step is the generation of a single unit cell of the target material, relaxed to its equilibrium geometry under periodic boundary conditions using the MM code to be used in the full QM/MM calculation. This gives a ground-state starting point, which is expanded to the necessary size by ChemShell in order to allow for the cutting of a non-periodic cluster. For bulk defects and active sites within zeolites, the resultant cluster is approximately spherical, while for the study of surfaces a hemisphere is cleaved from a 2D periodic slab instead.

The outer edge of the cluster must then be modified to correct for the termination of the periodicity. This is achieved by sampling the electrostatic field of the interior of the cluster (comprising the inner atoms which will later be designated as the QM region, as well as a portion of the MM atoms), and placing a shell of point charges outside the cluster which are tuned to reproduce the bulk or surface electrostatics within the cluster as accurately as possible, and to minimise the dipoles in each of the three Cartesian directions. Additionally, the charges on atoms in the outer layer of the cluster may be modified, the most common method being to scale the values in proportion to their coordination number. For example, an atom on the cluster exterior which would have a charge of +2 in a six-coordinated bulk environment would have its charge reduced to +1.67 if its coordination number had been reduced to five.

Once a cluster has been generated, a subset of atoms must be specified as those to be included in the QM calculation, followed by the identification of the remaining atoms as MM or boundary species. In the current ChemShell implementation, the boundary atoms are those which are given large-core pseudopotentials in order to constrain the QM electron density, and are chosen by enforcing a cutoff around each QM atom, within which all MM cations are included in the boundary layer. The remaining MM atoms are then subdivided into "active" and "frozen" shells for the purposes of a QM/MM optimisation calculation. Active atoms are those surrounding the QM and boundary regions, specified by a cutoff distance from the centre of the cluster, which are allowed to relax under the influence of forces generated when changes are made to the cluster, such as the introduction of an adsorbate or creation of a defect. The frozen atoms are those outside the cutoff, which remain fixed in their bulk lattice positions in order to preserve the structural integrity of the cluster. Figure 2.1 illustrates each of the separate component layers of the QM/MM calculation and how they are nested to form the whole cluster.

Some of the most important considerations when setting up a QM/MM cluster are the choice of MM cutoff radius, which determines the extent to which the MM calculation will be polarised by changes within the QM region, and the boundary atom cutoff radius, which must be large enough to ensure that the "tails" of any diffuse functions present within the QM calculation are not unduly influenced by positive point charges in the MM region. An additional consideration is the match between the ground-state lattice parameters for the QM and MM calculations, which must be as close as possible to prevent artificial strain at the boundary.

This effect can be minimised by re-tuning the interatomic potentials to match *ab initio* results rather than experimental data.

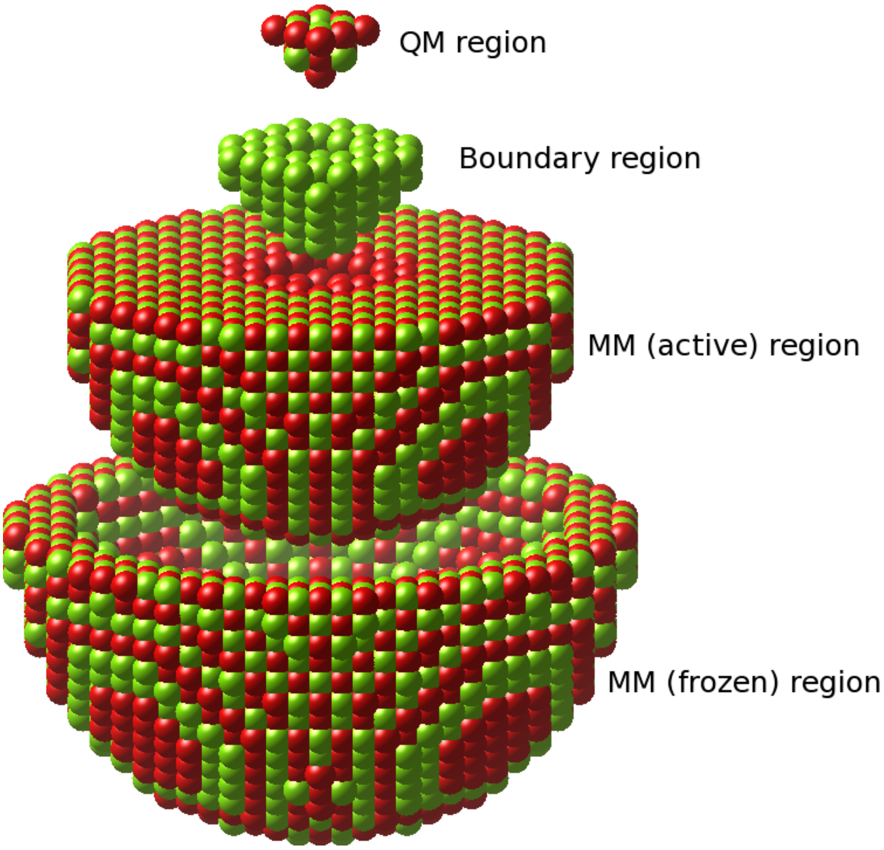

Figure 2.1: The embedded cluster setup used within ChemShell. Moving from top to bottom: the all-electron QM region; the cation-only large-core ECP region forming the QM/MM boundary; the relaxing MM ions; and the frozen MM ions. The outermost shell, containing point charges which are placed to ensure the Madelung potential in the centre of the cluster is accurately reproduced, has been omitted for clarity.sorbate species interact with the central oxygen atom or the four surface magnesium atoms.

2.4 Resources

Two QM codes, GAMESS-UK (General Atomic and Molecular Electronic Structure System)[55] and NWChem,[56] were used to perform the electronic structure calculations within the ChemShell environment. Both perform gas phase cluster calculations with a gaussian basis set and have directly comparable levels of accuracy. A single MM code, GULP (General Utility Lattice Program),[57–59] was used for all interatomic potential based calculations presented within this thesis.

Calculations were primarily performed on the UK national supercomputing facilities HECToR[60] and ARCHER.[61] Other HPC resources used included the Iridis[62] and Legion[63] clusters, as well as the Blue Joule and Blue Wonder clusters provided by industrial collaborators at the STFC Hartree Centre.[64]

Chapter 3

MgO for CO_2 Conversion Catalysis

Many investigations are currently focused on the reactivity of carbon dioxide with the aim of finding both an economical catalyst for CO_2 conversion into industrially relevant products such as methanol, and also as a means to sequester CO_2, e.g. by conversion to carbonate as an alternative to storage within geological sinks as a supercritical fluid. Rocksalt alkali-earth oxides such as CaO and MgO are amongst the most important sorbent materials currently under investigation for this purpose.[14,15]

The bulk and surface structures of magnesium oxide have been extensively studied, owing both to the simplicity of its rocksalt geometry and also the high degree of ionicity, which gives rise to a simple electronic structure. Additionally, basic oxides such as MgO are popular catalyst support materials which have been shown to display interesting reactivity when dopants or defects are included, opening up the possibility for their use as catalysts in their own right.

In this study, the mode of CO_2 adsorption on O_{5c} sites of the MgO [001] terrace is examined, along with oxygen vacancies, i.e. F-centres,[65] as adsorption sites which may exhibit different charge states due to the localization of two (F^0), one (F^+) or no electrons (F^{2+}). Oxygen vacancies containing trapped electrons have been identified as possible active sites for the conversion of CO to methanol in the Cu/ZnO/Al_2O_3, with CO_2 acting as a reactive intermediate species.[30,31,33,36,54,66] Within the reaction process, CO_2 is bound to the oxygen vacancy and undergoes a number of hydrogen addition steps, leading to the formation of methanol and the defect-free ZnO surface. The role of CO within the proposed mechanism is simply to regenerate the defect sites via its transformation to CO_2, completing the catalytic cycle. The applicability of this mechanism to other oxides besides ZnO is of interest, as it is easy to imagine that the performance of such a reaction process would be highly tunable via modification of the surface with dopants or adatoms, stabilizing the oxygen vacancy and encouraging electron localization. MgO is a useful test case as its high Madelung potential causes electrons to be highly localized at its oxygen vacancies, with the trade-off that formation of such vacancies has a very high energetic cost.

Our results for the interaction of CO_2 with MgO surface sites, as well as the subsequent investigation of the catalytic cycles accessible upon addition of H_2 to the CO_2-surface complex, have been published in peer-reviewed journals.[67,68]

3.1 Computational Approach for MgO

All calculations use the QM/MM approach described in Section 2.3. The full QM/MM cluster measured 60Å in diameter, and was centred on an oxygen atom which was to be used as the site for adsorption or defect formation. In total, around 3700 atoms were free to undergo ionic relaxation in each calculation. The outermost 5Å of the cluster had all atoms frozen in their bulk positions (as determined by prior relaxation using GULP), whilst all other atoms within a radius of 25Å of the cluster origin were allowed to relax. The accuracy of the treatment of the outermost 7Å of relaxing MM atoms is reduced due to their interatomic potential cutoff values lying outside the range of frozen atoms present. However, the remaining 18Å thick region surrounding the defect site remains, giving an accurate reproduction of the effect of long range polarization. The interatomic potential (provided in appendix B) consisted of Lennard-Jones and Buckingham terms, with rigid ion Mg atoms and polarizable shells on O atoms, optimised for embedded cluster calculations. The interatomic potential correctly reproduces the relaxation and rumpling of the MgO surface. No additional potential terms were included to account for the interactions of the adsorbate with the surface, as the CO_2 molecule was always located directly above the QM part of the surface, with the closest MM atoms at least 5Å away.

The innermost QM region comprised those atoms described by the all-electron density functional theory calculation and ranged in size from 22 to 26 atoms depending on the presence of vacancies or adsorbate molecules. This QM region size was chosen to minimise computational cost while providing a calculation comparable with work already available in the literature. Tests were performed to determine how the F^{2+} defect formation energy varied with QM region size from one to six nearest neighbour shells surrounding the central oxygen atom, with no significant improvement found for cases larger than four nearest neighbour shells, leading to this value being chosen.

The B3LYP[69–71] exchange-correlation functional was used throughout this study due to its good representation of both molecular species and oxides in previous work.[72]

These calculations employed a modified version of the Def2[73] triple-zeta valence plus polarization (TZVP) basis set for O and H atoms, and a similarly modified quadruple-zeta valence plus polarization (QZVP) basis set for Mg and C. The modification consisted of removing the most diffuse functions, specifically those uncontracted gaussians extending beyond 5Å, to prevent the artificial spreading of charge density outside the QM region. Stuttgart effective core potentials[74] were placed on cations at the border of the QM region for the same purpose.

The cluster used in this study displays behaviour which is 4-fold symmetric around the z-axis, with equivalent positions displaying a variance in their total charge of less than $0.001e$. Bond distances between surface layer Mg and O atoms vary by less than 0.02Å between the QM and MM regions after relaxation, suggesting that the interatomic potential provides a good match for the relaxation characteristics of the B3LYP functional.

3.2 Defect Formation on MgO

The neutral F^0 surface defect site, which corresponds to the removal of a neutral oxygen atom from the lattice to leave two electrons localized at the vacancy, was created by removing the central oxygen atom and maintaining the formal charge of the cluster. For the F^+ and F^{2+} cases, the total charge of the cluster was increased by 1 and 2 e respectively, equivalent to the removal of O^- and O^{2-}. As the O^{2-} ion only exists within the solid phase and the conduction band for bulk MgO is above the vacuum level,[75,76] the most common means of determining defect formation energies is to relate the energies of the defective clusters to pure MgO, a neutral oxygen atom, and isolated electrons, as in:

$$E_f = E(defect)^{n+} + E(O_{at}) + nE(e^-) - E(MgO_s) \tag{3.1}$$

where $E(\text{defect})^{n+}$ is the energy of the cluster (which may be neutral or positively charged), $E(O_{at})$ is the energy of a neutral gas-phase oxygen atom, E(MgO) is the energy of a neutral relaxed cluster and $E(e^-)$ is the energy of an electron at the vacuum level, defined as zero. The positions of the defect states in relation to the MgO valence band and the vacuum level are shown in Figure 3.2.

When a charged defect was being modelled (i.e. F^+ and F^{2+} centres), an additional corection term[36,54] was included *a posteriori* to account for the polarization of atoms outside the sphere of relaxing MM atoms, given by Equation 3.2

$$E_{corr} = -\frac{Q^2}{2R}\frac{(\varepsilon - 1)}{(\varepsilon + 1)}, \tag{3.2}$$

Q denotes the total charge of the defect, R is the radius of the relaxed region, and ε is the dielectric constant of MgO.

Defect formation energies for each of the charge states are given in Table 3.1 with results from previous work for comparison.[77–79] The similarity between results presented in this thesis and those already published strongly suggests that the current cluster model provides a suitable representation of the system. Results in Reference 78 were obtained using an embedded cluster method similar to ours, with special attention paid to the optimization of an added set of basis functions sited on the vacancy, which allow for better representation of electrons localized at the defect site. Reference 79 also used an embedded cluster, but neither set of previous results included the full effects of long range relaxation, both having considerably fewer point charges outside the QM region than the cluster in use here has MM atoms, with no shell model to account for the electronic polarization of these distant ions. Reference 77 has results most readily comparable with ours, being based on a very similar embedded cluster technique with polarizable shells outside the QM region. The most significant differences in this case are in the number of point charges outside the relaxing region and the overall shape of the cluster.

In Figure 3.1, it is possible to see how the charge of the oxygen vacancy affects the relaxation of atoms in the surrounding area. Comparing images 3.1a-3.1c with their counterparts 3.1d-3.1f, it is observed that the extent of relaxation is somewhat greater along the surface plane than down into the bulk. For comparison, a periodic supercell calculation would need dimensions of at least 4x4x2 unit cells (for F^0) or 8x8x3 unit cells (for F^{2+}) in order to capture the same information.

Defect	Uncorrected	Corrected	[77][a]	[78][b]	[79][c]
F^0	9.23	9.23	9.07	9.35	7.67
F^+	11.14	10.90	11.57	10.78	12.38*
F^{2+}	14.44	13.51	16.07	14.07	22.08*

Table 3.1: Defect formation energies for F^0, F^+ and F^{2+} states of the oxygen vacancy. "Corrected" terms include the *a posteriori* Jost correction to account for the truncation of the region undergoing ionic relaxation.[36,54] [a] DFT (B3LYP) embedded cluster calculations with polarizable shells and *a posteriori* correction. [b] "Perturbed cluster embedding" Hartree-Fock calculations with no long-range polarization [c] Hartree-Fock calculations with no long-range relaxation effects or boundary ECPs included. * Not given directly in reference as the authors used a different formalism for calculating defect formation energies. Value calculated from data given in Table 2 of Reference 79.

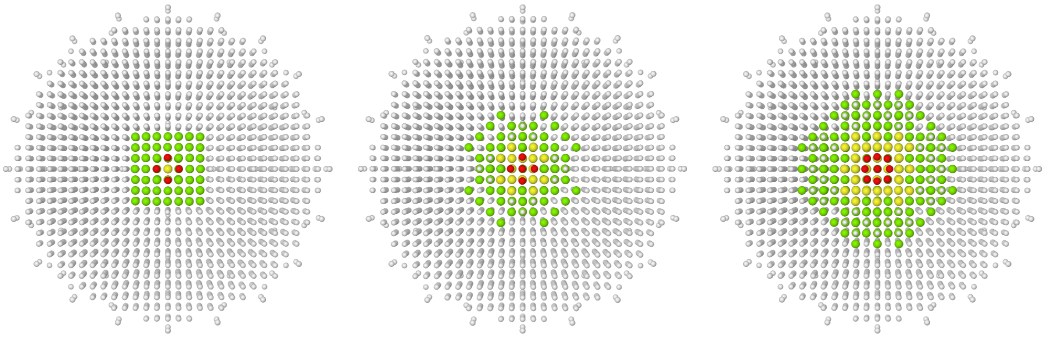

(a) F^0 (b) F^+ (c) F^{2+}

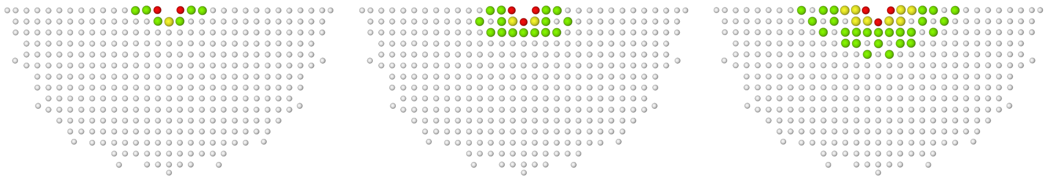

(d) F^0 (e) F^+ (f) F^{2+}

Figure 3.1: From left to right: atomic displacements surrounding surface F^0, F^+ and F^{2+} centres. The top row (a-c) show the cluster surface (x-y plane), and the bottom row (d-f) show a slice through the cluster (x-z plane). Atoms with displacements lower than 0.01 Å shown in white, 0.01-0.04 Å in green, 0.04-0.08 Å in yellow and greater than 0.08 in red. The angular nature of the displaced regions is an artefact of the cutoffs chosen for colour coding, and the fact that a spherically-symmetric phenomenon is being observed on a cubic grid of points.

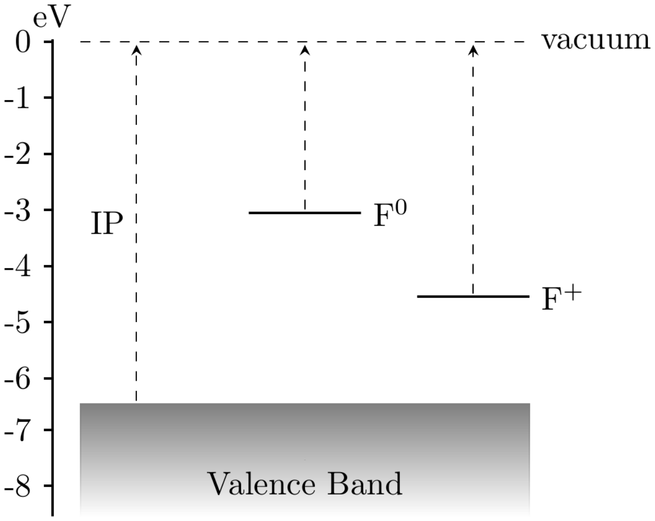

Figure 3.2: Positions of defect levels of MgO and their vertical ionization potentials. MgO (100) terrace IP: 6.46 eV, F^0: 3.05 eV, F$^+$: 4.55 eV. Relaxation to the ground states corresponding to MgO$^+$, F$^+$ and F^{2+} gave values for the adiabatic ionization potentials of 5.52, 1.91 and 3.30 eV respectively.

3.3 CO_2 Adsorption on the MgO (100) Surface

A great deal of work has been performed over the past 30 years focused on the interactions between CO_2 and MgO, the most notable examples of which are outlined below.

Previous computational studies of the interaction between CO_2 and MgO have generally found the 5-coordinated oxygen on the [001] terrace to be an unfavourable adsorption site, with the 4 and 3-coordinated oxygens located at corners and edges being the preferred positions for chemical interactions to take place.[80–82] The commonly stated reason for this difference between surface and defect sites is identical to the proposed cause of differing reactivities between MgO and CaO - the strength of the Madelung potential at the 5-coordinate oxygen atoms in the surface layer (O_{5c}) of MgO is so large that electron transfer onto the CO_2 is thought to be unfavourable. Although this general conclusion has been reached by a number of authors, more recent work includes notable exceptions, which find CO_2 adsorption at these sites to be weakly favourable.[83,84]

Experimental work on this topic is even less clear. Using measurements of oxygen exchange and infra-red spectra[85–87] authors of references 85–88 tend to support the current theoretical models, which propose that carbonate formation only occurs at defect sites, i.e. kinks, corners, steps and vacancies, although there is no clear concensus as to what form the carbonate takes (monodentate, bidentate etc.)[88] or which sites play a role in the interaction. Other experimental work using temperature programmed desorption measurements suggests that the CO_2 interaction with MgO is reasonably strong at 9.4 kcal/mol (0.41 eV, 39.33 kJ/mol) although the authors interpret this result as a purely physical interaction.[89] A combined experimental and theoretical investigation by Yanagisawa et al. found two distinct carbonate species on the MgO surface after room temperature adsorption of CO_2, and identified one as monodentate while the other was suspected to include bidentate or tridentate character.[90]

Before results of this work are presented in further detail, attention should be drawn to a common approximation being made for the surface-adsorbate interactions. The calculations presented here, like any other employing a localised basis set, suffer from the effects of basis set superposition error (BSSE), a phenomenon which arises where the electron density of a species benefits from the additional degrees of freedom provided by the basis functions of a second nearby species, leading to an artificial reduction of the energy of the interacting system relative to its isolated components. This work has made use of the functional counterpoise correction procedure[91,92] to estimate the effect of BSSE. An upper bound for the BSSE energy was obtained by making the approximations that the magnitude of BSSE is proportional to the distance between the two components in the cluster-adsorbate complex, and that the error is maximised in cases where the orientations of the involved species cause the overlap of diffuse functions to be maximised. Single point calculations for a range of distances were performed, each with orientations such that maximum overlap was achieved. The upper estimate for the BSSE as a function of distance was then used to determine the maximum necessary value of the counterpoise correction term. Figure 3.3 shows how the calculated BSSE varied with distance, and the linear fit used throughout the study to determine counterpoise corection values. For calculations involving the interaction of CO_2 with the MgO surface, the approximate counterpoise correction value was determined from the linear fitted function shown in Figure 3.3, based on the surface-adsorbate separation distance after relaxation. These corrections generally fell within the range 0.15-0.18 eV. Final adsorption energies are corrected for BSSE, while NEB profiles are instead scaled relative to the energy of the non-adsorbed geometry with no correction. It is likely therefore that barrier heights shown are underestimated by approximately 0.10-0.15 eV (9.65-14.47 kJ/mol) depending on the orientation and elevation of the transition state structure.

Two physisorption geometries, shown in Figure 3.4, were identified for CO_2 over the MgO(100) surface: one with an orientation perpendicular to the surface plane

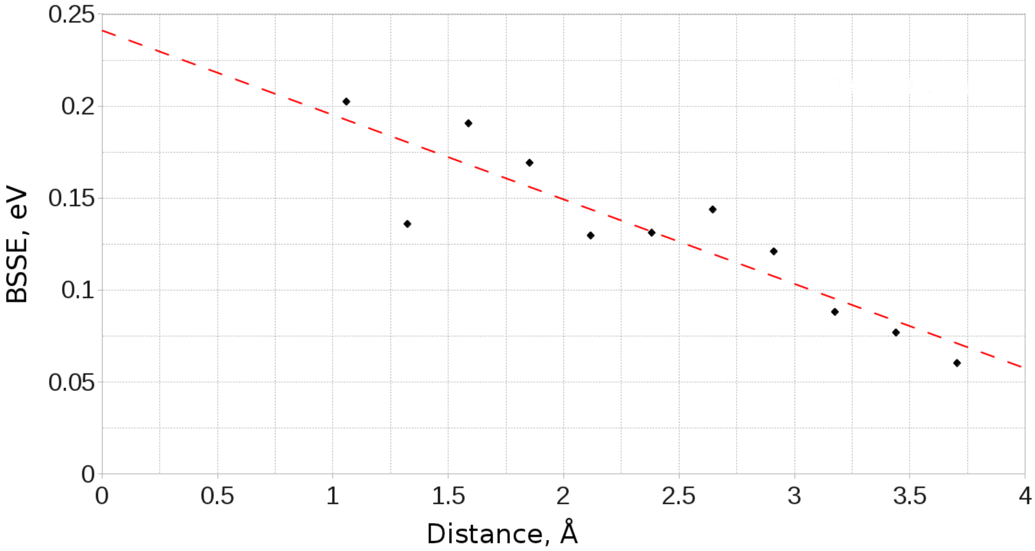

Figure 3.3: Variation of the basis-set superposition error with the distance between surface and adsorbate components for the unmodified MgO surface and a parallel orientated CO_2 molecule.

located over a 5-coordinate surface magnesium site (Mg_{5c}), the other parallel to the surface but rotated 45° to the lattice axes and bridging two nearest-neighbour Mg_{5c} sites. The interaction energies for the two structures after counterpoise correction were 0.075 eV (7.24 kJ/mol) and -0.046 eV (-4.44 kJ/mol), corresponding to corresponding to a repulsive interaction and an attractive interaction, respectively. As no van der Waals correction term is included in the density functional theory part of this QM/MM calculation, it is likely that both structures are in reality more strongly adsorbed than this result would suggest. An estimate of 0.2-0.3 eV (19.30-28.5 kJ/mol) for the van der Waals correction based on calculations of small molecules,[93] for example, would completely outweigh the effects seen in the present calculations. Also, the magnitude of BSSE for the perpendicular orientation is likely to be significantly overestimated compared to the parallel geometry due to a different degree of overlap between basis functions. Assuming a stronger van der Waals correction for the parallel orientation but also a greater BSSE, it is suggested that the parallel orientation will be the more favourable of the two.

Experimental work by Meixner et al. suggests that CO_2 adsorbs on single crystal MgO with an energy of 29.7-39.3kJ/mol.[89] The energies measured experimentally may be modified by lateral interactions between adsorbate molecules, but these effects are likely to be smaller than the discrepancy between calculations and experiment, and it is proposed that the experimental result is more closely aligned with the chemisorption model proposed below than the physisorption values calculated, even after the inclusion of a van der Waals correction and vibrational effects. It should be noted, however, that the above conclusions are based on the expectation that experimental adsorption results were dominated by the effects of the defect-free surface, with lower coordinated sites such as edges and corners playing only a minor role in the measured adsorption behaviour. This assumption has more validity for comparison with single crystal experimental work than experiments using powder samples.

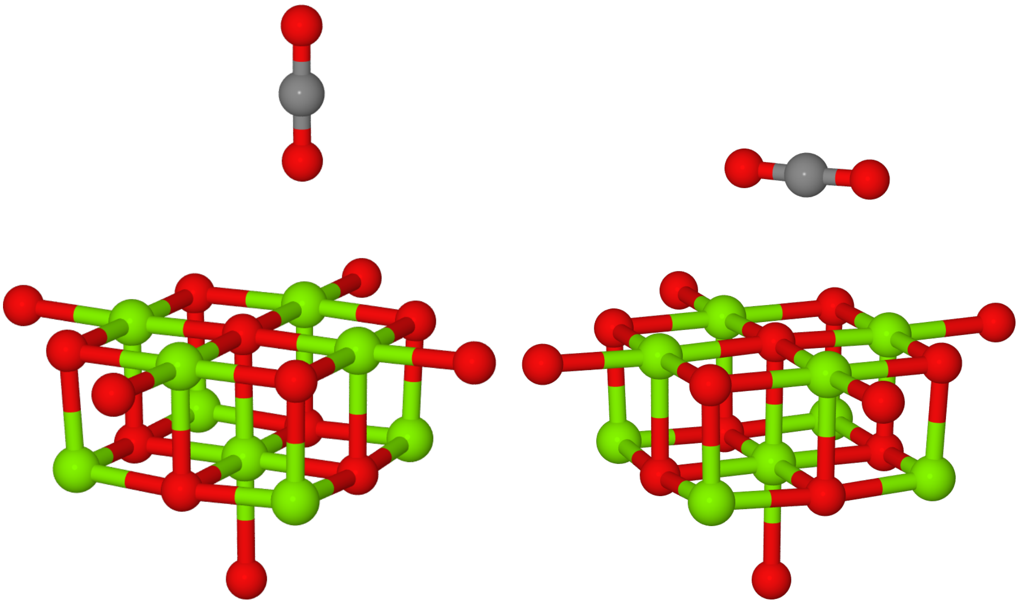

(a) Perpendicular

(b) Parallel

Figure 3.4: Physisorption structures identified for CO_2. In both cases, the oxygen atoms of the adsorbate are coordinated to surface Mg atoms. In the perpendicular case, the Mg_s-O_{ads} distance for the minimum energy structure was found to be 2.50Å , while for the parallel structure the two Mg_s-O_{ads} were equal at 2.76Å . O atoms shown in red, Mg in green and C in grey.

Stable chemisorbed geometries have been located for the interaction of CO_2 with the MgO (100) terrace O_{5c} site, as well as F-centres in a number of charge states - these are shown in Figure 3.5, Figure 3.10 and Figure 3.12. In each case, the starting configurations corresponded to a CO_2 molecule aligned perpendicular or parallel to the surface plane, with the latter aligned along the axes of the lattice. Initial structures for the "adsorbed" and "elevated" CO_2 were obtained by placing the molecule a fixed distance above the surface and allowing the structure to relax to a local minimum. For "adsorbed" structures, a starting point with the CO_2 around 1Å above the surface was chosen, while for the "elevated" starting point a number of surface-adsorbate distances were attempted until the "elevated" structure no longer relaxed to the same position as the "adsorbed" structure.

The adsorbate undergoes at least one favourable interaction with each of the O_{5c}, F^0 and F^+ sites, with the identified structures in general agreement with previous work.[81,94] In the case of the doubly positive charged oxygen vacancy F^{2+} however, neither parallel nor perpendicular alignments of CO_2 resulted in any significant interaction with the defect. In both cases a repulsive interaction was observed between the CO_2 and the surface as the separation was decreased, with no local minima or barriers. Given the lack of reactivity and significantly higher defect formation energy, it can be safely assumed that the F^{2+} site plays no significant role in the adsorption of CO_2 on MgO. Results for all sites considered are summarised in Table 3.2, with previous results also included for reference. Negative adsorption energies correspond to a favourable interaction relative to the isolated cluster and adsorbate. Vibrational frequencies for the structure where adsorption occurred are given in Table 3.3.

The interaction of a CO_2 with the terrace O_{5c} site is the most commonly studied of the reactions described in this work. Previous studies find the same carbonate-like adsorption geometry shown in Figure 3.5a. Until recently the structure has generally been disregarded however, as it was found to be unstable with respect to dissociation. By contrast, the results presented here suggest that the monoden-

Defect	Orientation	This Work	Previous Work
None	Parallel	-0.68 (-65.61)	0.77 (74.29),[82] 0.62 (59.82),[81] 0.135 (13),[80] -0.09 (-8.68),[95] -0.38 (-36.69)[84]
	Perpendicular	0.12 (11.58)	n/a
F^0	Parallel	-2.36 (-227.71)	-1.85 (-178.50)[94]
	Perpendicular	-3.52 (-339.63)	-3.23 (-311.65)[94]
F^+	Parallel	-0.71 (-68.50)	-0.23 (-22.19)[94]
	Perpendicular	-1.11 (-107.10)	-1.04 (-100.35)[94]
F^{2+}	Parallel	0.11 (10.61)	n/a
	Perpendicular	0.04 (3.86)	n/a

Table 3.2: Summary of results for the adsorption energies of CO_2 with various terrace sites on MgO. All energies in eV (kJ/mol). Reference 84 outlines results obtained using a periodic slab calculation, while all others were obtained using clusters embedded in a point charge array.

Structure	Frequencies (cm^{-1})							
O_{5c}+CO_2 (mono.)	601	610	702	707	846	922	1291	1669
O_{5c}+CO_2 (tri.)	603	611	692	694	864	907	1295	1666
F^0+CO_2 (par.)	588	597	600	604	608	801	1284	1429
F^++CO_2 (par.)	594	595	611	613	643	741	1296	1789
F^++CO_2 (perp.)	589	592	595	605	637	765	1216	1712

Table 3.3: Vibrational frequencies for the surface-adsorbate complexes found to show stable adsorption. None of the structures displayed imaginary frequencies, suggesting that all structures represent local minima of the potential energy landscape. Highest 8 frequencies shown for each structure; lower values are assumed to correspond to surface phonons and are excluded.

tate geometry is thermodynamically stable (by around 0.68 eV, 65.61 kJ/mol). A NEB calculation to determine the reaction profile for adsorption, shown in Figure

3.6, reveals a small barrier of around 0.1 eV (9.65 kJ/mol), which increases to around 0.2 eV (19.30 kJ/mol) if the effects of BSSE are included.

The difference in energy between results shown here and those of earlier investigators is particularly striking given the similarity of the adsorbed structures. A significant number of early studies were carried out using the Hartree-Fock (HF) methodology, as opposed to the hybrid Density Functional Theory (DFT) approach used in this work. HF calculations do not include electron correlation effects, leading to the possibility that this discrepancy could account for the difference in total energy observed. However, by repeating calculations for CO_2 adsorption at an O_{5c} site using the same QM/MM system but with the DFT-based QM stage replaced by a HF calculation, it has been confirmed that this is not the case. E_{ads} for a HF QM/MM calculation was found to be around -1.43 eV (-137.97 kJ/mol), suggesting that the inclusion of correlation actually destabilises the surface-adsorbate complex rather than stabilising it. Other effects must therefore be responsible for the difference in energy between the results presented here and those published previously.

Previous studies do not include such a large relaxing volume around the active site, leading to the possibility that long-range polarization is responsible for the observed differences. Given that early work which found the interaction to be most unfavourable included small clusters of QM atoms embedded in a static point charge array,[82] and that the most recent comparable study which found the surface-adsorbate complex to be somewhat favourable used a larger 90-atom supercell,[84] this appears at first glance to be a reasonable proposal.

Additional test calculations were performed in an attempt to verify this conjecture, involving the use of clusters with reduced relaxing MM regions. For a relaxation radius of 18Å, an E_{ads} of -0.68 eV (-65.61 kJ/mol) was calculated, identical to the original cluster. Given that approximately the same energy is found when the relaxation radius is further reduced to 15Å, it can be concluded that the polarization within the smallest relaxing region considered is accurately calculated. Indeed, the polarization of the cluster during CO_2 adsorption would be expected to be comparable to that seen for the F^0 defect formation in Figure 3.1, although with lower symmetry due to the orientation of the molecule. A relaxed region with a radius of at least 10-12Å would therefore be expected to be necessary, and the inclusion of any extra atoms within the MM part of the cluster would have had a negligible effect - hence the lack of distinction between results for the 15, 18 and 25Å MM region radii that were tested. The use of the shell model potential gives these cluster calculations a significant advantage in this regard, as it allows for the inclusion of both ionic and electronic polarization effects for a large number of atoms with minimal additional cost.

The number of non-QM atoms in the calculation may still be a contributing factor even if polarization is not as significant as expected - the larger embedded cluster calculations performed in the past included less than half the number of point charges relative to the number of MM atoms used in the QM/MM model described here, and no additional point charges on the border of the cluster to reproduce the Madelung potential in the central region. The beneficial effect of this improved Madelung potential representation is likely to be small, but taken together with the effects of polarization within the 10-12Å region identified as significant and a high-quality QM calculation, could be enough to explain the difference in adsorption energy between the work presented here and previous studies.

The extent to which the polarization of the surface influences the final energy can be estimated using the Born-Onsager model for solvation of a dipole, given by Equation 3.3.

$$E_{dip} = \frac{(\epsilon - 1)\mu^2}{(2\epsilon - 1)a^3} \tag{3.3}$$

The dipole is formed by the adsorbed CO_2 and the oxygen atom at the center of the cluster. A single Mg-O bond length (3.98 a.u.) is taken as the cavity radius a, and the total dipole moment change between the chemisorbed structure and a

CO_2 at large separation from the MgO surface, μ, is 1.8 a.u. ϵ is the dielectric constant of MgO.

Modification of the Born-Onsager model is necessary in this case, as the "solvent" environment surrounding the cavity is hemispherical rather than spherical. Given that this term is analogous to the Jost correction described earlier (which accounts for polarization due to the presence of a charged species), and that the Jost term for a surface lies between 50 and 100% of the bulk value depending on the dielectric medium,[36] we can be confident that the component of the total energy due to relaxation around the dipole is no less than half the calculated value of E_{dip}. Taking this approximation into account, a conservative value for the component of the adsorption energy due to relaxation around the dipole of 0.29 eV (28.37 kJ/mol)is obtained. This accounts for over 40% of the adsorption energy of CO_2 at an O_{5c} site, and provides a strong indication that the inclusion of longer-range relaxation effects is essential in order to obtain an accurate description of molecular adsorption energetics, even at the simplest surface sites.

A second adsorption geometry for the O_{5c} site, which is defined here as tridentate, is shown in Figure 3.5b. The structure is a local minimum, around 0.18 eV (17.37 kJ/mol) less stable than the aforementioned monodentate configuration, with a barrier of 0.09 eV (8.68 kJ/mol) for the tridentate-monodentate conversion (0.27 eV (26.05 kJ/mol) for the reverse conversion) as shown in Figure 3.7. The consideration of BSSE is not necessary in the case of monodentate-tridentate conversion shown in Figure 3.7 as both structures would receive an approximately equal counterpoise correction. Only one case[96] was identified where a structure similar to the tridentate geometry of Figure 3.5b has been identified previously, and the small cluster size used makes the results of the earlier study more easily comparable to those for low-coordinated edge and corner sites. Vibrational frequency calculations (table 3.3) identify modes at 922, 1291, 1669 cm^{-1} for the monodentate structure and 907, 1295, 1666 cm^{-1} for the tridentate structure, suggesting that distinguishing between the two would be very difficult using vibrational spectroscopy.

Despite speculation in previous experimental reports,[86,88] no bidentate adsorbed structures have been observed in computational investigation of CO_2 on the MgO (100) terrace, although recent work[95] has shown that a pre-formed carbonate could adopt a bridging structure. We attempted to find a structure similar to that postulated and shown in Scheme 1 of reference 86 and Figure 6 of reference 88 where the carbon atom and one oxygen of CO_2 are coordinated to adjacent O and Mg atoms, but in each case the bidentate starting structure relaxed to the monodentate form shown in Figure 3.5a. Likewise, attempts to find a bridging bidentate structure between two adjacent Mg atoms resulted in the formation of either the tridentate chemisorbed configuration 3.5b or weakly physisorbed CO_2 as in Figure 3.4b.

Given that the physisorbed and tridentate configurations have reasonably similar adsorbate oxygen atom positions, it is reasonable to postulate that the tridentate structure (Figure 3.5b) could behave as an intermediate state between the physisorbed structure shown in Figure 3.4b and the chemisorbed monodentate structure shown in Figure 3.5a. A NEB adsorption pathway for this physisorbed-tridentate conversion is shown in Figure 3.8, and a complete pathway from the physisorbed structure to the monodentate chemisorbed structure is given in Figure 3.9. The multi-step adsorption route has an activation barrier which is slightly higher than that of direct adsorption to the monodentate structure from the gas phase, and so its relevance will depend heavily on the nature of the physisorption precursor when van der Waals forces are included, as they would be likely to shift both the physisorbed local minimum and the barrier to a lower energy.

In the case of the neutral F^0 defect with two electrons localised within the vacancy, only one structure (shown in Figure 3.10a) corresponding to CO_2 adsorption in a parallel orientation was identified, with an adsorption energy of -2.36 eV (-227.71 kJ/mol) - a considerably more favourable interaction than seen by Florez et al,[94]

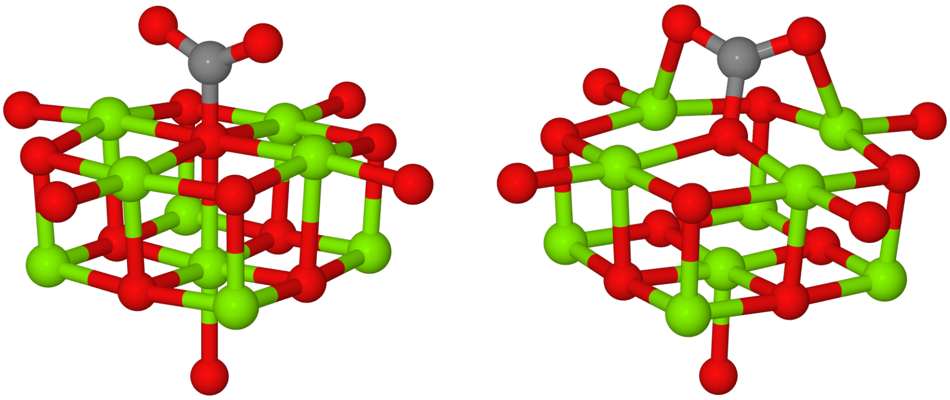

(a) Monodentate (b) Tridentate

Figure 3.5: Adsorption geometies for CO_2 coordinated to an O_{5c} site. Structure 3.5a is generally described as monodentate, although it could be considered as a linear tridentate structure with the adsorbate O atoms coordinated to first-nearest-neighbour Mg atoms in the surface. Structure 3.5b is a less stable local minimum obtained by rotating and tilting the monodentate structure. In the monodentate structure, the O_s-C_{ads} distance is 1.41Å and the OCO angle is 131.3°. For the tridentate structure, the C-O bonding distance between the adsorbate and the surface is preserved, while the internal angle is reduced to 128.8°. The two Mg_s-O_{ads} bond distances are measured as 2.10Å . O atoms shown in red, Mg in green and C in grey.

but as the minimum energy structures found in the two studies are essentially identical, we can conclude that the energy difference has a similar origin to that seen for the O_{5c} site. The exothermic adsorption process seen here has no activation barrier in nudged elastic band calculations (Figure 3.11). Mulliken analysis suggests that there is charge transfer onto the adsorbate, with approximately an additional 1.2 electrons being located on CO_2 in the adsorbed geometry when compared to the molecule at a large degree of elevation above the surface.

The relaxation of perpendicularly oriented CO_2 (shown in Figure 3.10b) in close proximity to the defect leads to the unactivated dissociation of CO_2 to CO and

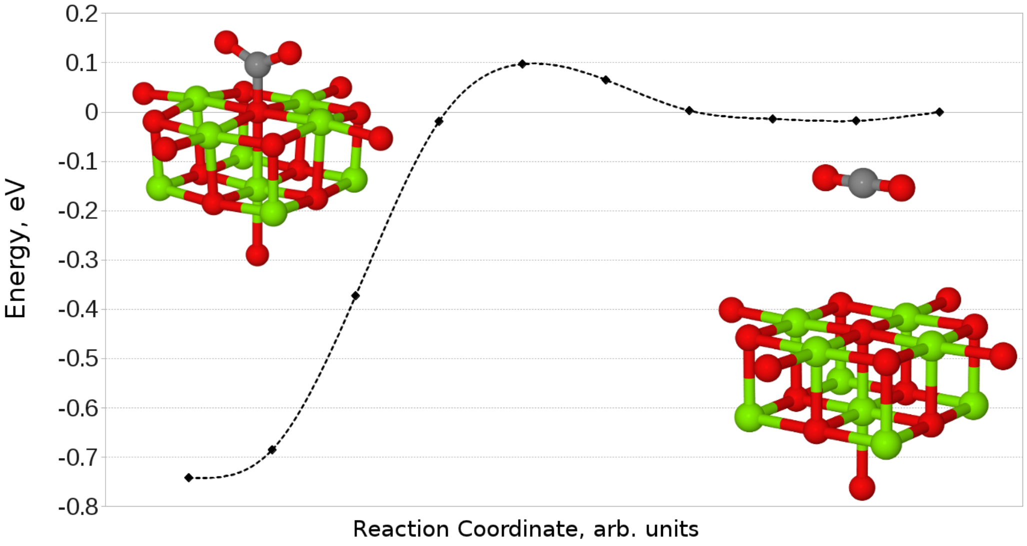

Figure 3.6: Reaction profile for the adsorption of CO_2 at an O_{5c} site obtained using the NEB method with 10 images. Counterpoise corrections not included.

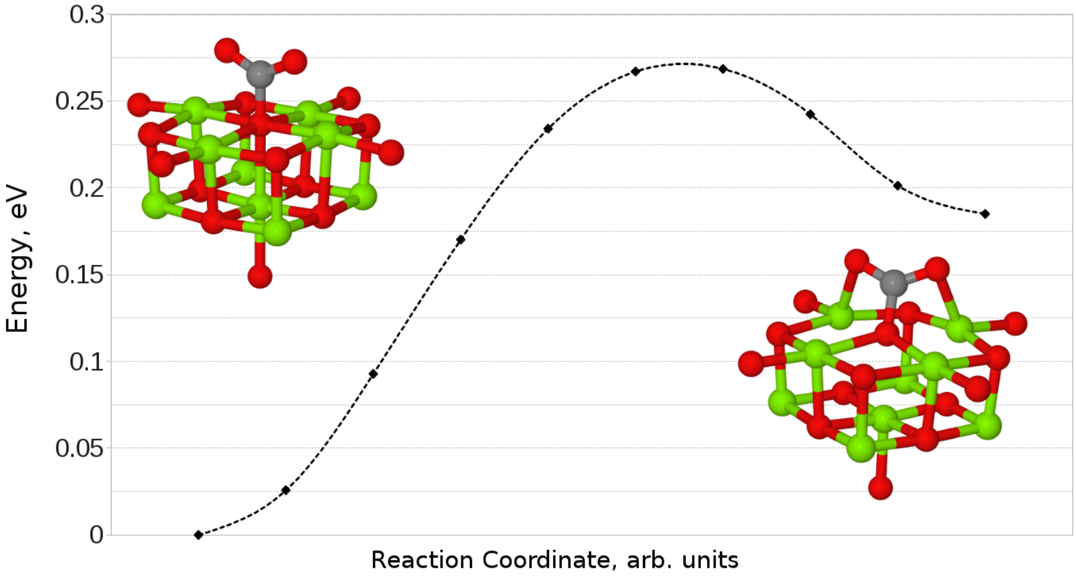

Figure 3.7: Reaction profile for the conversion between mono- and tridentate adsorbed CO_2 geometries at an O_{5c} site obtained using the NEB method with 10 images. A barrier of 0.27 eV (26.05 kJ/mol) is observed for the monodentate-tridentate conversion, while the reverse reaction exhibits a barrier of 0.09 eV (8.68 kJ/mol).

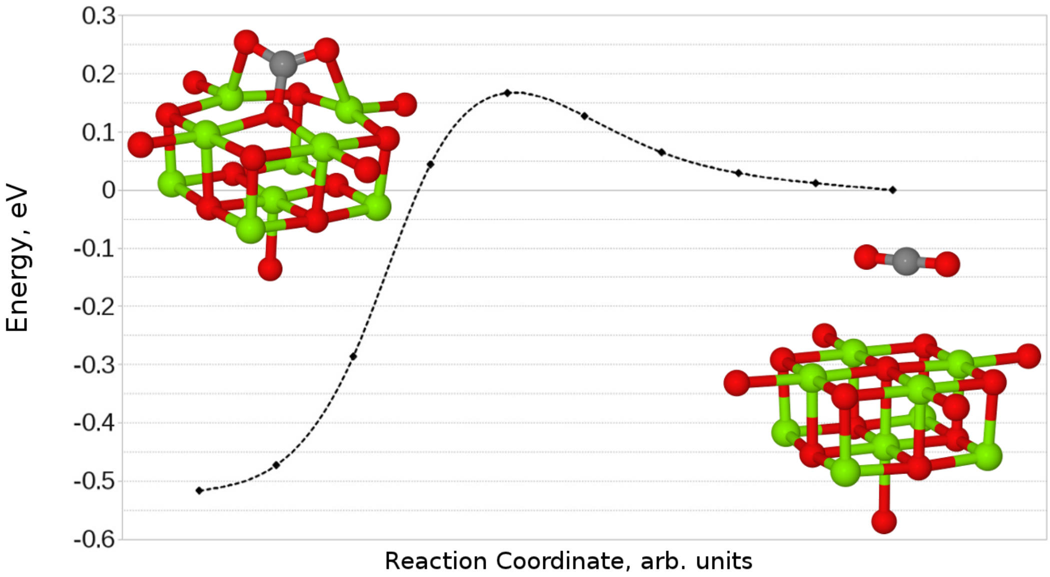

Figure 3.8: Reaction profile for the conversion between parallel physisorbed and tridentate adsorbed CO_2 geometries on the defect-free MgO (100) terrace obtained using the NEB method with 10 images. A barrier of 0.17 eV (17.40 kJ/mol) is observed for the adsorption process.

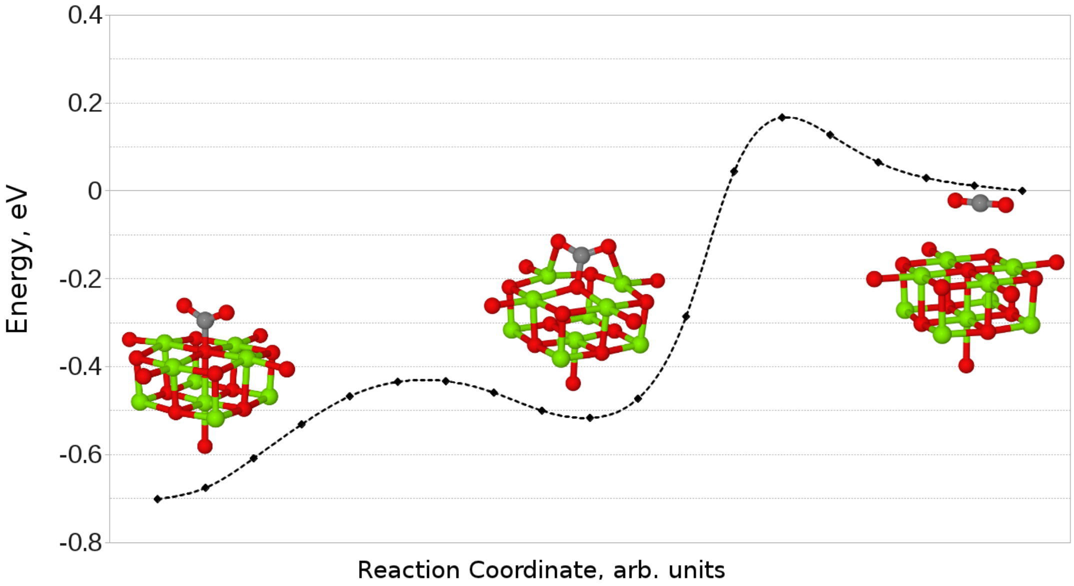

Figure 3.9: Reaction profile for an alternative adsorption process, from physisorbed CO_2 to the monodentate chemisorbed species via a tridentate intermediate.

O_{at}, with the oxygen atom filling the vacancy and reconstructing an unmodified MgO surface, in agreement with recent theoretical work.[94]

Based on the results described, the usefulness of F^0 centres for CO_2 conversion catalysis is expected to be limited: although the parallel adsorbed structure could feasibly behave as a reactive intermediate if another small molecule such as H_2 were introduced, the reaction of the perpendicularly orientated adsorbate to form CO and a defect-free surface would poison the catalyst. The reverse reaction to generate an F^0-centre by introducing CO is highly endothermic, and is therefore unlikely to make catalysis viable even if there were a highly efficient route from the parallel adsorbed CO_2 complex to a useful product such as methanol.

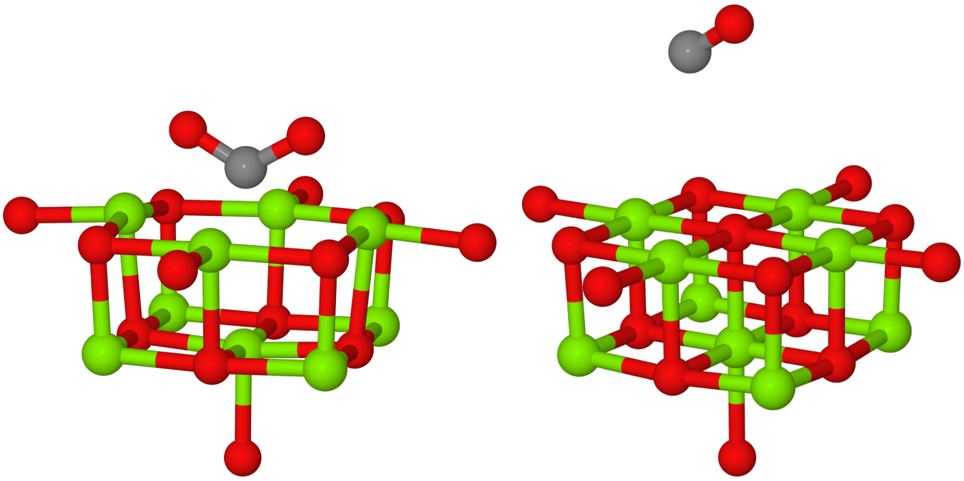

(a) Parallel (b) Perpendicular

Figure 3.10: Structures obtained after relaxation of CO_2 in proximity to an F^0 centre. The internal angle of the adsorbate when in the parallel orientation is 120.8°, while the two Mg_s-O_{ads} distances are 2.01Å . In the perpendicular case, a defect-free MgO surface is formed and the CO molecule does not remain in close proximity to the surface. O atoms shown in red, Mg in green and C in grey.

Finally, the case of an oxygen vacancy with a single localised electron, designated as an F^+ defect, was considered. The parallel adsorption of CO_2 leads to a similar structure to that observed for an F^0 site (Figure 3.12a), with a reduction of charge transfer onto the adsorbate from 1.2 to 0.6 electrons. Mulliken analysis reveals that the majority of this electron localization occurs at the carbon atom. The

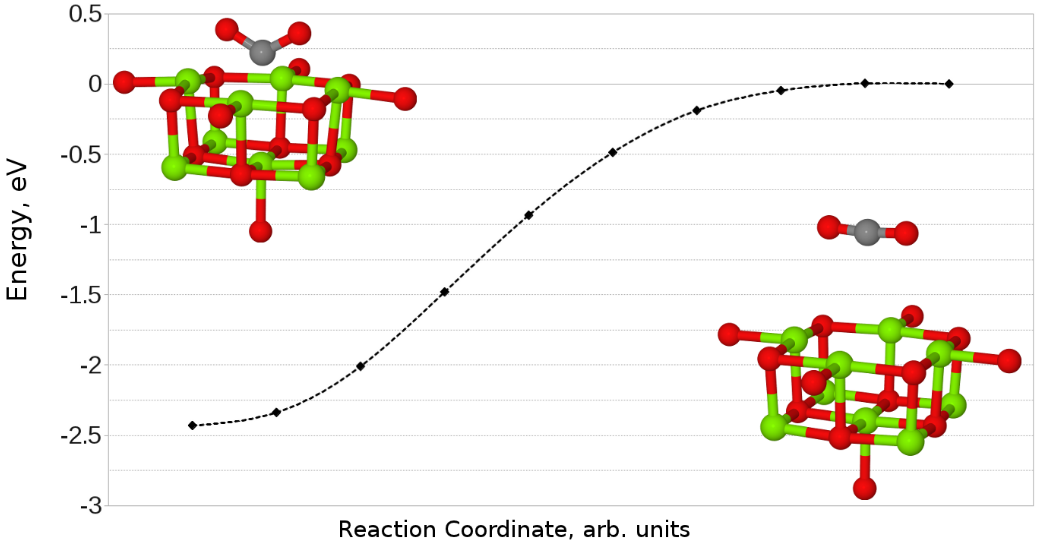

Figure 3.11: Structures obtained after relaxation of CO_2 in proximity to an F^0 centre on the MgO (100) terrace, obtained using the NEB method with 10 images. No barrier to adsorption is observed. Counterpoise corrections not included.

adsorption energy for this interaction was found to be -0.71 eV (-68.50 kJ/mol), with a barrier of around 0.05 eV (4.82 kJ/mol)

In the case of perpendicular adsorption (Figure 3.12b), the observed structure is somewhat reminiscent of the CO_2 anion bound to a surface oxygen vacancy in ZnO[33] and identified by Preda et al. as part of the reaction of CO_2 with low-coordinated, electron rich sites at the MgO surface.[97] An adsorption energy of -1.11 eV (-107.10 kJ/mol) shows that this is the preferred interaction orientation for CO_2 over an F^+ centre, being favoured over the parallel geometry by 0.4 eV (38.59 kJ/mol). However, the barrier for perpendicular adsorption of around 0.16 eV (15.44 kJ/mol) is approximately 0.1 eV (9.65 kJ/mol) higher than that for parallel adsorption. A greater degree of spin localization on the adsorbate is observed in the perpendicular case, with $0.72e$ located on the carbon atom and a further $0.15e$ on the upper oxygen atom.

Given that neither interaction of CO_2 with the F^+ site leads directly to the regeneration of the defect-free surface, it is possible that subsequent reaction with a small molecule such as H_2 could form part of a catalytic cycle for the transformation of CO_2. Such a mechanism will require preserving or regenerating the single-electron F^+ centre during later reaction steps, although the high defect formation energy (10.90 eV, 1051.70 kJ/mol) could lead to preferential regeneration of the defect-free MgO (100) surface and the production of a cationic molecule. Giordano et al. have shown that in ultrathin MgO/Ag(100) films, F^+ sites can be made to be more stable than F^0 due to the occurrence of significant lattice distortion and polarization of the metal.[98]

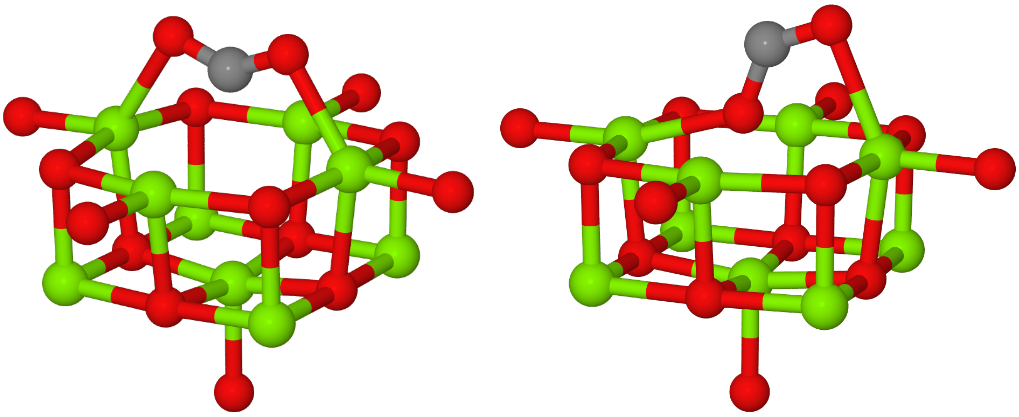

(a) Parallel

(b) Perpendicular

Figure 3.12: Geometies obtained after relaxation of CO_2 in proximity to an F^+ centre. The internal angle of the adsorbate when in the parallel orientation is 138.9°, while the two Mg_s-O_{ads} distances are 2.18Å . For the perpendicular orientation, the lower oxygen atom lies close to the vacant lattice site but slightly elevated, with a shortest Mg_s-O_{ads} distance of 2.24Å . The upper oxygen atom appears to be coordinated to another surface magnesium with a bonding distance of 2.36Å . The internal angle of the CO_2 adsorbate in this orientation is 128.8° O atoms shown in red, Mg in green and C in grey.

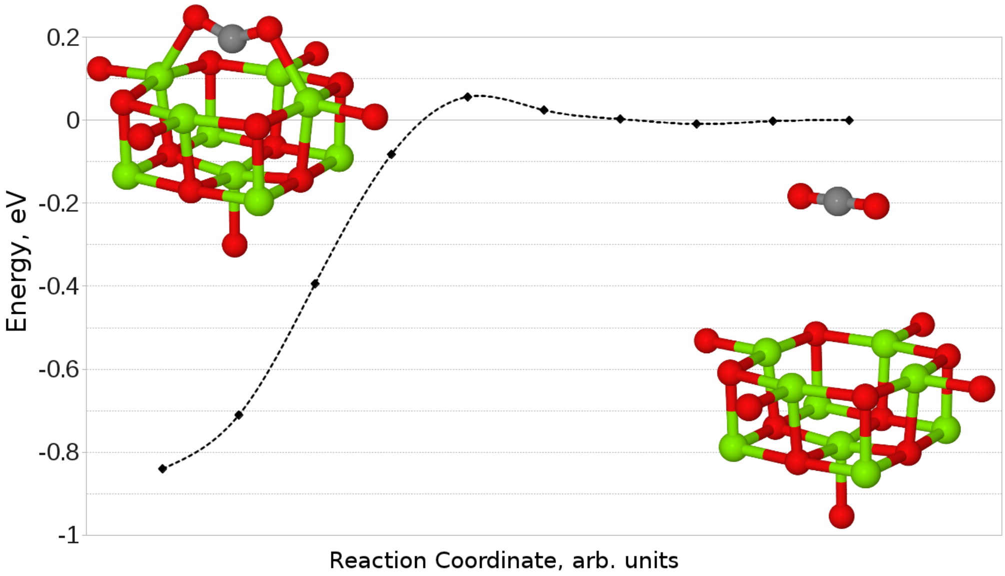

Figure 3.13: Reaction profile for the parallel adsorption of CO_2 at an F^+ centre on the MgO (100) terrace, obtained using the NEB method with 10 images. Counterpoise corrections not included.

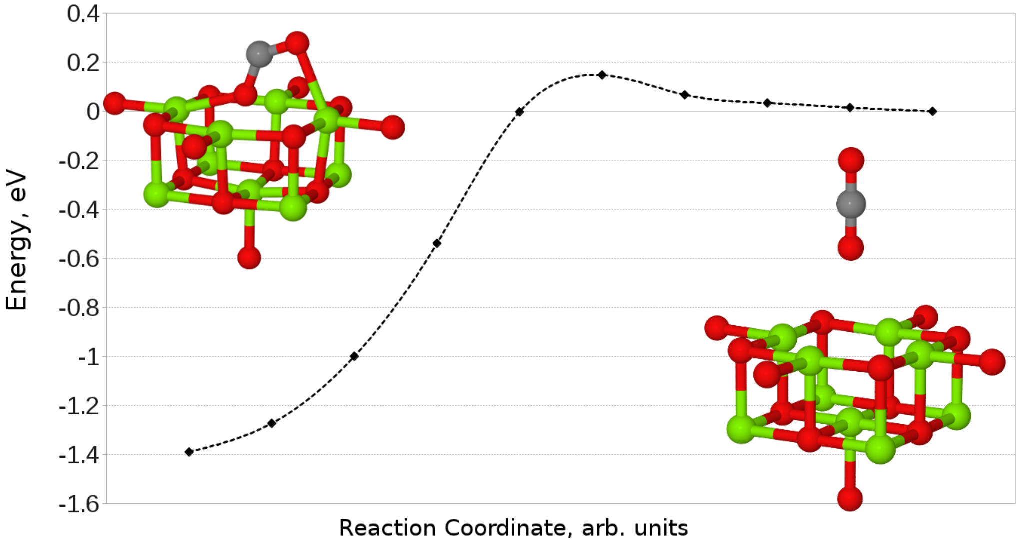

Figure 3.14: Reaction profile for the perpendicular adsorption of CO_2 at an F^+ centre on the MgO (100) terrace, obtained using the NEB method with 10 images. Counterpoise corrections not included.

3.4 Addition of H_2 to Adsorbed CO_2

In the work already described, it was determined that the most likely candidate for use in a catalytic reaction was the CO_2 chemisorbed at an F^+-centre, aligned normal to the surface, shown in Figure 3.12b. CO_2 adopting this structure displayed exothermic binding to the defect site as well as a high degree of electron localization onto the adsorbate molecule. It may be noted that a localized single electron at a surface oxygen vacancy site has been proposed as the active site for CO_2 conversion to methanol on ZnO.[33] Other possible sites such as CO_2 adsorbed at the F^0-centre were considered in the first hydrogen addition stage; however none gave rise to a more thermodynamically stable product and they were therefore not considered further.

In the calculations described in this section, pairs of hydrogen atoms were seqentially introduced to the CO_2-MgO surface-adsorbate complex, corresponding to the addition of up to three H_2 molecules. In each case, H_2 was introduced to the surface-adsorbate complex calculation by adding a hydrogen molecule in the vicinity of likely adsorption sites (e.g. near the carbon atom of the surface bound CO_2), as well as in starting configurations which do not preserve the bonding of the hydrogen molecule (e.g. one H atom bound to the surface, the second to the adsorbate), before relaxation. Reaction processes requiring pre-adsorption and heterolytic dissociation of H_2 were not considered, as this process has a relatively high energy cost on the MgO (100) terrace of 77.71kJ/mol based on calculations using a defect-free cluster (other sources place this value even higher at around 173.7kJ/mol).[99] Heterolytic dissociation may however play a role in reactivity at low-coordinated sites.[100,101] Dissociation at a neighbouring F^+-centre was also considered, having a lower energy cost of 25.07kJ/mol. However, adsorption and dissociation of H_2 at such a defect would have the disadvantage of deactivating the catalytic site, as one hydrogen atom fills the vacant oxygen position while the other forms a nearby OH group. Given their high formation energy and mutual electrostatic repulsion, the terrace is expected to be free from F^+-centres. Any that do exist will be transient and isolated, and so migration of hydrogen atoms between them can be expected to play little or no role in the reaction processes described here.

The minimum energy structure obtained after hydrogen adsorption was carried forward to the next H_2 addition step, with other higher energy routes also considered if they were thought to lead towards a significantly more stable species. Due to the number of possible hydrogen atom positions and adsorbate orientations, there were several elementary steps between each of the identified minima and therefore activation barriers are not considered: instead, the aim is to chart a range of intermediates in the CO_2 conversion reaction and identify alternative or competing catalytic cycles.

The proposed cycle is shown in Figure 3.15. The first step involved the adsorption of CO_2 at the F^+-centre to give structure B, with an exothermic adsorption energy of -132.3kJ/mol. This is followed by the addition of one hydrogen atom to the carbon of the adsorbed CO_2 to give a surface-bound formate ion, with the second hydrogen forming an O-H bond with the surface, as shown in structure C. Other structures investigated included the addition of both H atoms to the adsorbate (on either the carbon or upper oxygen atom) as well as the shift of the surface-bonded hydrogen to other O_{5c} sites. Configurations with both hydrogen atoms bonded to the adsorbate were generally not stable, relaxing to the structure shown or to one with an alternative surface hydroxyl site (structures with one hydrogen bound to the CO_2 and the other to the surface are approximately equal in energy regardless of the positioning of the surface hydroxyl group). All structures investigated in this initial stage were stable with respect to molecular H_2, with the lowest energy geometry having a chemisorption energy for H_2 of around -115.1kJ/mol.

The addition of a second pair of hydrogen atoms led in the most favourable case to the dissociation of the CO_2 adsorbate to a molecule of H_2O and a formaldehyde molecule bound to the defect site via the oxygen atom, which sits close to the position necessary in order to re-form the defect-free (100) surface. The structure (labelled D) shown in Figure 3.15 was the most stable configuration examined, but formation was unfavourable with respect to dissociation of the second pair of hydrogen atoms to form H_2 by around 3.2kJ/mol. Localization of the unpaired electron onto the carbon atom was enhanced by the breaking of the upper C-O bond. The removal of water and formaldehyde from structure D could in principle lead to the regeneration of the F^+-centre to give a closed cycle, although this step is endothermic by 273.6kJ/mol.

On addition of a third pair of hydrogen atoms, the most energetically favoured process identified was the regeneration of a defect-free MgO surface with an OH-group coordinated to a surface magnesium ion and two protons forming hydroxyl groups with surface oxygen anions, plus the formation of the CH_3 radical, shown in structure E. A reaction energy of -66.8kJ/mol (relative to the previous structure and a gas phase H_2 molecule) was calculated. The formation of methanol over a positively charged MgO surface with two adsorbed hydrogen atoms was also identified and found to be exothermic (structure F), although to a lesser extent than the first structure at approximately -29.6kJ/mol, suggesting that a reaction process to form methanol is possible, although the major product will be the CH_3 species and products of its subsequent reactions with other small molecules.

Formation of a surface-bound methoxy group (-O-CH_3) was not found to be favourable on the vacant site at any stage of the sequential H_2 adsorption process, which is probably a consequence of the positive charge and unpaired electron, which lead to the dissociation of a methoxy group to CH_3 and OH in the presence of hydrogen atoms adsorbed at the surface.

The addition of a fourth H_2 to the surface in the presence of the radical species enables the formation of a methane molecule and release of H_2O from the surface, leaving two hydrogen atoms adsorbed to MgO^+, the same structure seen after the formation and desorption of methanol. The final stage necessary to close the reaction cycle after formation of either methanol or methane is the regeneration of the F^+ site and removal of the two hydrogen atoms adsorbed to the surface.

Previous work has however shown that for an F^0-centre water desorption would be an endothermic process[102] and is therefore likely to be a significant limiting step, an observation which can be confirmed with the determination that desorption of H_2O to leave behind the required F^+-centre is endothermic by 170kJ/mol. Within both structures F and G, the unpaired electron density is distributed over the surface-layer magnesium atoms in the first nearest-neighbour shell around the filled vacancy.

The three catalytic cycles can be summarised as follows:
$CO_2 + 2H_2 \rightarrow CH_2O + H_2O$, $\Delta E = 29.47$kJ/mol (endothermic)
$CO_2 + 3H_2 \rightarrow CH_3OH + H_2O$, $\Delta E = -76.77$kJ/mol (exothermic)
$CO_2 + 4H_2 \rightarrow CH_4 + 2H_2O$, $\Delta E = -201.89$kJ/mol (exothermic)

As in the case of methanol synthesis over ZnO, the greatest challenge appears to arise due to the tendency for oxygen atoms to remain bound to defect sites after the initial reaction processes are complete. In the ZnO case, this effect causes the cycle to be shifted from the catalytic conversion of CO_2 to the consumption of CO, although a cycle such as those described here where an additional molecule of H_2 is used to regenerate the active site is also feasible.

For MgO, the route is altered by the need for ionization to give the desired single-electron oxygen vacancy. This shortcoming can be in principle be avoided through the use of alkali-metal doping, such as in the well-studied case of Li-MgO;[103] however the presence of paramagnetic centres due to Li-doping is disputed.[104] An additional factor which may contribute to the viability of single-electron oxygen vacancies as active sites is the use of ultrathin MgO films, which have been shown to allow for F^+-centres to be favoured over the generally more stable F^0 oxygen vacancy with two localized electrons.[98] It has been noted[105] that the populations of F^0 and F^+ defects, particularly on the (100) terrace, are expected to be very low and therefore of limited relevance to an operating catalytic system.

The alternative single-electron site proposed by Pacchioni, the $(H^+)(e^-)$ species, should be considered in relation to CO_2 reactivity in the future.

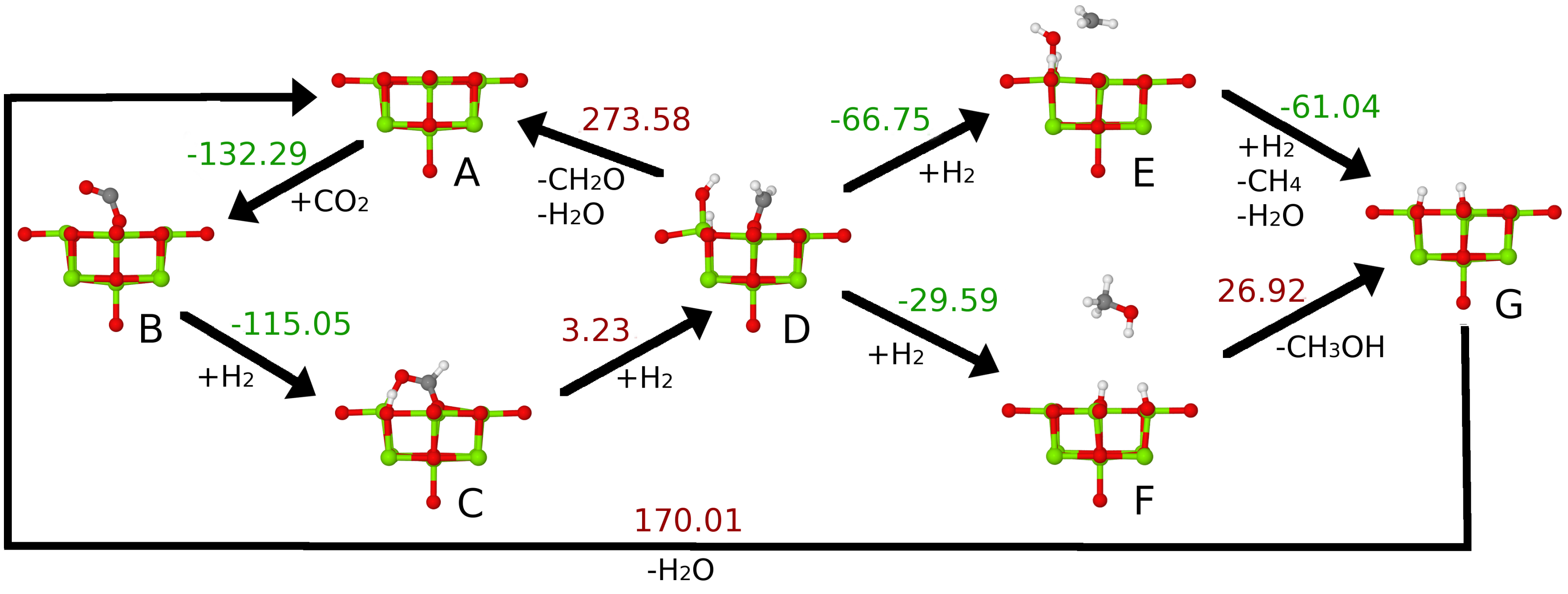

Figure 3.15: Catalytic cycles identified for the addition of CO_2 and H_2 to an F^+-centre. O atoms shown in red, Mg in green, H in white and C in grey. Energy changes for each step given in kJ/mol, with green and red representing exothermic and endothermic processes respectively. Key structures are as follows: A - Unmodified F^+-centre, B - CO_2 adsorbed at F^+-centre, C - 2×H adsorbed on structure B (one on the MgO surface, one on the CO_2 adsorbate), D - H + OH adsorbed on MgO surface, CH_2O bound to F^+-centre, E - 2×H + OH adsorbed on MgO surface, CH_3 radical formed, F - 2×H adsorbed on MgO^+ surface, CH_3OH formed, G - 2×H adsorbed on MgO^+ surface. Unpaired electron density for structures A, F and G is distributed over the surface-layer magnesium atoms in the first nearest-neighbour shell around the filled vacancy. For all other structures, the spin density is predominantly localised on the carbon atom of the adsorbate/product.

Chapter 4

Mn-doped MgO for CO_2 Conversion Catalysis

Moving beyond the simple alkali earth oxide model, further studies were performed on MgO surface sites modified by the addition of a single transition metal dopant atom. The effect of this dopant on oxygen vacancy formation and CO_2 adosrption were considered with reference to the undoped system.

Manganese was selected as the transition metal dopant to provide a systematic step between earlier work on MgO and a full transition metal oxide. Technical challenges, which will be described in the next chapter, necessitate the choice of a transition metal with unambiguous d-orbital occupancy and well understood magnetic properties - making Mn^{2+} an ideal candidate.

Mn-doped MgO has been extensively investigated in recent years with the aim of finding a dilute magnetic semiconductor (DMS) for use in spintronic applications.[106–112] It is common for these studies to make use of electronic structure methods, but focused on the doping and defect formation properties within the MgO bulk rather than at the surface. Very little attention has been paid to the effect of a manganese ion dopant on the surface reactivity of MgO. Part of the reason for this may simply be that the Mn^{2+} ion, which would be the species expected to form within an MgO lattice in order to maintain charge neutrality, is relatively stable due to the presence of five d-electrons, giving a half-filled shell. For the defect-free surface and F^0-centres, Mn-doped MgO is therefore expected to produce results which are qualitatively similar to undoped MgO. For F^+ and F^{2+}-centres, however, it is possible that electrons may be transferred from the manganese atom to the oxygen vacancy as follows:

$$\mathrm{Mn}^{2+} + F^{+} \rightleftharpoons \mathrm{Mn}^{3+} + F^{0} \tag{4.1}$$

$$\mathrm{Mn}^{2+} + F^{2+} \rightleftharpoons \mathrm{Mn}^{3+} + F^{+} \rightleftharpoons \mathrm{Mn}^{4+} + F^{0} \tag{4.2}$$

Whether any of these electron transfer processes occurs depends on the ionization energies of the F-centres and that of the Mn^{2+} (and Mn^{3+}) ions within the octahedrally coordinated lattice.

The study of Mn-doped MgO and its interactions with CO_2 proceeded in a similar manner to the work on MgO already described. Due to the need to consider alternative doping positions (below the central oxygen atom as well as in the surface layer adjacent to it), certain CO_2 adsorption configurations such as the physisorbed and tridentate structures were excluded, and calculations focused on those structures where potential onwards reactivity with other species was most likely.

4.1 Computational Approach for Mn-doped MgO

Calculations involving Mn-doped MgO were performed using a hemispherical QM/MM cluster setup similar to that described in Section 3.1, with a total radius of 30Å centred on an oxygen atom or oxygen vacancy. The radius of the relaxing MM region was reduced from 25Å to 15Å as a result of findings for MgO, suggesting that the impact of relaxing atoms beyomd 12-15Å was negligible. This reduction resulted in a total of around 850 atoms undergoing ionic relaxation, with the remainder frozen in the lattice positions obtained from a pre-optimisation using the MM code GULP.

The interatomic potential, provided in appendix B, was based on that of Lewis & Catlow,[113] with modifications to extend the cut-off radius and tune the O_{shell}–O_{shell} interaction to an appropriate value in order to reproduce the dielectric constant of MgO as accurately as possible. Unlike the potential used in the earlier work on undoped MgO, the doped system included shell components on cations as well as anions with the aim of improving the description of electronic polarisation within the system. No additional potential terms were included to account for the interactions of the adsorbate with the surface, as the CO_2 molecule was always located directly above the QM part of the surface, with the closest MM atoms at least 5Å away.

Both the B3LYP[69–71] and B97-3[114] functionals were used throughout this section of work. Results obtained using B3LYP provided a direct comparison with undoped MgO, while B97-3 results were obtained to provide a second data set using a similar amount of Hartree-Fock exchange (20% for B3LYP versus 27% for B97-3), but where the functional was directly fitted to thermochemical data.

In contrast with calculations performed on undoped MgO which used a mixture of quadruple and triple-zeta basis sets, these calculations employed the default Def2[73] triple-zeta valence plus polarization (TZVP) basis set for all atoms except

Mn, where a modified Stuttgart relativistic small core (RSC) basis set designed for use with an ECP was used instead. As was the case for undoped MgO, the modification consisted of removing the most diffuse functions to prevent the artificial spreading of charge density outside the QM region. The reduced basis set was chosen to provide greater consistency with later work on the pure transition metal oxide system, where it became desirable to minimise computational cost. As was the case for the previous MgO cluster, effective core potentials[74] were placed on cations at the border of the QM region to act as the QM/MM boundary. Additionally, an ECP representation of the manganese core electrons was used in order to include relativistic corrections.[115]

The presence of a redox-active species within the cluster opens up the possibility of a number of different electronic configurations, particularly in the case of the charged oxygen vacancies F^+ and F^{2+}. These were explored by varying the multiplicity of the calculations and comparing total energies and adsorbate geometries.

4.2 The Mn-doped MgO (100) Surface

While calculations related to the MgO [100] surface were mostly performed for benchmarking and testing purposes, the equivalent work for Mn-doped MgO is a necessary precursor to the addition of an adsorbate due to uncertainty over the effect of dopant position and possible variation in spin states when defects were introduced. The goal of the Mn-doped MgO study is to focus on differences in adsorption behaviour which are induced by the presence of a high magnetic moment on a metal atom near the adsorption site. This effect is expected only to influence the adsorption behaviour indirectly, but should be considered separately to any structural influences which may arise when moving away from rocksalt-structured materials.

Dopant Positions

Two different QM/MM clusters, each having a different dopant position, were used as the starting point for all calculations based on Mn-MgO. The first had the manganese atom situated in the first subsurface layer directly beneath the central oxygen atom, while the second had the manganese dopant in the surface layer adjacent to the central oxygen atom. These two configurations will be referred to as "below" and "side" respectively, and are illustrated in Figure 4.1. The Cartesian axes of the cluster were defined relative to the dopant positions such that the manganese atom in the "below" position occupied the magnesium lattice position [0,0,-z]. The the manganese atom in the "side" position occupied the magnesium lattice position [-x,0,0] and the primary oxygen lattice site (O_{5c} or F-centre) was situated at [0,0,0].

Formation energies for each doping configuration, given in Table 4.1, were calculated relative to the undoped MgO surface and isolated metal atoms:

$$E_f = E(MgO_s) - E(Mg_{at}) + E(Mn_{at}) - E(MnMgO_s) \tag{4.3}$$

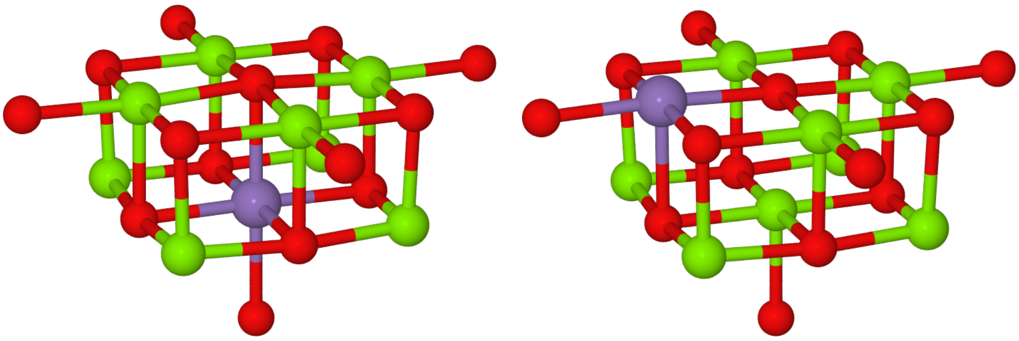
(a) Below (b) Side

Figure 4.1: QM cluster for Mn-MgO dopant positions considered. O atoms shown in red, Mg in green and Mn in purple.

	B3LYP	B97-3
Below	4.782 (461.387)	5.354 (516.566)
Side	5.292 (-510.635)	5.881 (567.407)

Table 4.1: Energy of Mn doping for Mn-MgO in eV (kJ/mol)

As might be expected, doping in the surface layer is favoured relative to doping in the subsurface position due to the additional degrees of freedom allowed during relaxation of the structure, minimising the effect of strain induced by the size discrepancy between manganese and magnesium. No Jahn-Teller distortion is expected as Mn^{2+} in an octahedral coordination environment has a half-filled d-shell with no degenerate occupancy configurations.

For the “below” dopant configuration, Mn-O bonds in the xy (sub-surface) plane were found to be elongated relative to the adjacent Mg-O bonds at 2.17 and 2.06Å respectively. The lower Mn-O bond (between the second and third atomic layers) was elongated further at 2.19Å, as was the Mn-O bond between the central surface oxygen and the dopant at 2.22Å. The O-Mn-O bond angles within the xy plane were maintained at 90°, while the elongation of the lattice parameter in the z-axis near the defect caused the bond angles in the xz and yz planes to be distorted to 90.6°.

For the “side” dopant position, Mn-O bonds in the surface (xy) atomic layer were once again 2.17Å, while the Mn-O bond in the z-direction was elongated to 2.26Å. Bond angles are also more significantly distorted in the “side” dopant case, being between 87 and 96° in the vicinity of the manganese atom.

Oxygen Vacancy Formation

The formation energy for each type of oxygen vacancy was calculated in a similar manner to earlier work on MgO, relative to the doped (but defect-free) surface and an isolated oxygen atom, with excess electrons set to the vacuum level:

$$E_f = E(F^{n+}MnMgO) + E(O_{at}) + nE(e^-) - E(MnMgO_s) \tag{4.4}$$

For the F^0-centre a single electronic configuration was considered, with a pair of electrons occupying the oxygen vacancy and the manganese ion maintaining its high-spin d^5 state. When ionized to an F^+-centre, there are a number of possible configurations depending on whether the electrons within the vacancy or on the manganese ions are preferentially removed. Finally, for F^{2+}, a second electron may be removed from the same location as in the F^+ case, or the charge may be delocalised over both dopant and vacancy by removing one electron from each. By comparing the Mulliken spin polulations for high and low-spin configurations of each charged vacancy, the ground state electronic configuration may be identified for each case.

Defect formation energies for each dopant position and functional are given in Table 4.2. Mulliken population analysis for the F^0-centres revealed the expected electronic configuration with two electrons occupying the oxygen vacancy (delocalised over diffuse magnesium functions) and five unpaired electrons occupying the same spin channel on manganese. For both high and low-spin varieties of the F^+-centre with B3LYP, as well as high-spin with B97-3, the electronic configurations correspond to the ionization of the oxygen vacancy. In the high-spin case,

	Below		Side	
	B3LYP	B97-3	B3LYP	B97-3
F^0	8.793	8.545	8.823	8.561
F^+ (LS)	10.644	12.321	10.696	12.599
F^+ (HS)	10.939	10.799	10.976	10.834
F^{2+} (LS)	15.322	15.369	15.879	16.498
F^{2+} (HS)	14.638	14.541	14.711	14.639

Table 4.2: Defect formation energies for Mn-MgO in eV. For the F^+ and F^{2+}-centres, both high-spin and low-spin configurations were considered.

all electrons on manganese as well as within the vacancy occupy the alpha spin channel, while in the low-spin case the alpha channel on manganese and beta channel of the vacancy are occupied. The lower energy of the low-spin cases seen for B3LYP may be attributed to the inclusion of additional degenerate configurations including the mixing of alpha and beta occupancy on both the vacancy and manganese ion, as opposed to the single possible configuration accessible for the high-spin F^+-centre. Finally, the F^{2+}-centre was found to preferentially adopt the high-spin configuration where both electrons necessary for double ionization are removed from the vacancy rather than the manganese ion.

Results for low-spin F^+ with the B97-3 functional are anomalous, with Mulliken analysis showing that the ionization process removes the beta-channel electron from the oxygen vacancy (indicated by the partial population of alpha channels on first nearest-neighbour magnesium atoms), forcing the manganese atom to adopt a low-spin configuration to maintain the target multiplicity. F^0 and F^+-centres were found to have a lower formation energy than the equivalent defect in undoped MgO, while for F^{2+} the formation energy increases in the doped system. A possible explanation for this observation is that electrons within the vacancy benefit from additional variational freedom provided by manganese basis functions, an effect which is negated in the F^{2+} case by the lack of electrons within the vacancy.

4.3 CO_2 Adsorption on Mn-doped MgO (100) Surface

For each combination of dopant position and defect site described in Section 4.2, a number of CO_2 adsorption processes were considered. For clusters with the dopant in the “below” position, the C_{4v} symmetry of the cluster was preserved and adsorbate molecules were aligned with their O-C-O axis along either the Cartesian x or z directions of the cluster, corresponding to the “parallel” and “perpendicular” orientations described in Section 3.3. For clusters having the “side” dopant position, the symmetry of the cluster was reduced to C_s, necessitating the inclusion of a third set of adsorbate orientations with the O-C-O axis aligned along the cluster y-direction.

Based on the findings outlined in Section 4.2, both high and low-spin configurations were used for the study of CO_2 adsorbates interacting with F^+-centres, while a high-spin configuration was maintained throughout all work on O_{5c} sites as well as F^0 and F^{2+} defects. As the CO_2 adsorbate begins as a closed-shell system, electron transfer into either alpha or beta channels is equally likely, with no spin-flip transitions necessary.

Due to the number of dopant, defect, CO_2 orientation and multiplicity configurations available, work was limited to the determination of adsorbed structures and analysis of any electron transfer taking place, with adsorption profiles and barriers excluded due to the prohibitively high cost of performing NEB calculations on a large number of systems.

Energetic data are provided for both B3LYP and B97-3 functionals for comparison. Unless a significant discrepancy in the Mulliken charges or ground-state structure are observed, all other results are focused on B3LYP.

O_{5c} Site

The ground state adsorbed structure for CO_2 over MgO with an Mn dopant in the subsurface position is shown in Figure 4.2, while structures for the surface-layer doped cluster are shown in Figure 4.3. Based on results for undoped MgO, no significant interaction between the O_{5c} site and CO_2 aligned with the z-axis was expected; data shown in Table 4.3 confirms this to be the case, with a weakly repulsive interaction being present.

For the x- and y-axis aligned adsorbates, the interaction with the O_{5c} site was found to be essentially identical to that observed for MgO, leading to the formation of a carbonate-like species. Partial redistribution of charge density onto the adsorbate is observed in each case, although it is the O_{5c} oxygen site and neighbouring magnesium atoms which are consequently depleted, while the manganese dopant retains its half-filled d-subshell.

Comparison of the different functionals consistently shows more favourable binding for B97-3, with exothermic interactions being around 10% stronger for B97-3 than B3LYP, while the weak repulsive interactions are slightly less endothermic. This result is consistent with the expectation that the inclusion of more Hartree-Fock exchange causes electrons to become more localised, strengthening the newly formed bonds.

Dopant Position	Adsorbate Orientation	B3LYP	B97-3
Below	X	-0.753 (-72.639)	-0.819 (-79.100)
	Z	0.047 (4.545)	0.039 (3.826)
Side	X	-0.616 (-59.402)	-0.705 (-67.987)
	Y	-0.699 (-67.404)	-0.759 (-73.327)
	Z	0.045 (4.306)	0.032 (3.094)

Table 4.3: Energy of CO_2 adsorption on Mn-MgO O_{5c} sites in eV (kJ/mol).

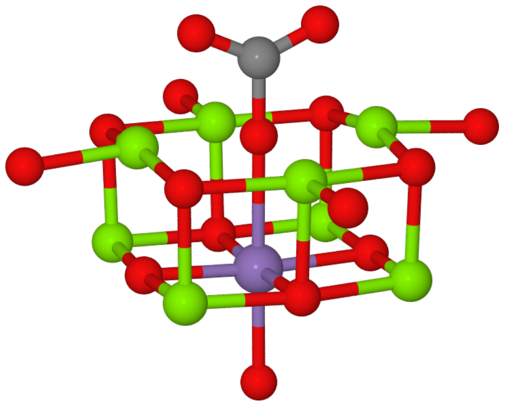

Figure 4.2: CO_2 adsorbed on the Mn-doped MgO(100) surface, where the dopant is situated in the second atomic layer. O atoms shown in red, Mg in green, Mn in purple and C in grey.

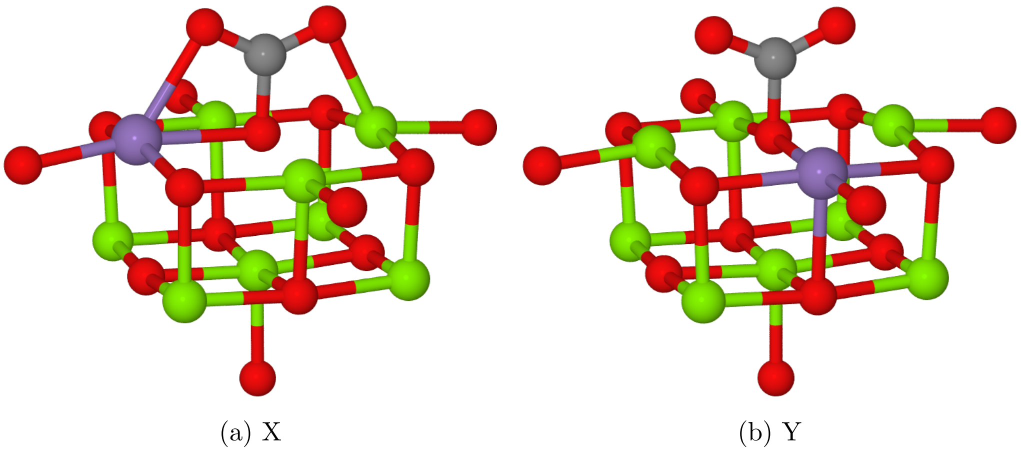

(a) X

(b) Y

Figure 4.3: CO_2 adsorbed on the Mn-doped MgO(100) surface, where the dopant is situated in the first atomic layer. O atoms shown in red, Mg in green, Mn in purple and C in grey.

F^0-Centre

The ground state adsorbed structures for CO_2 over Mn-MgO with an F^0-centre and the dopant located in the sub-surface and surface layers are shown in Figure 4.4 and Figure 4.5, respectively. The observed adsorption processes exhibit the same general behaviour as seen for undoped MgO, with the F^0-centre causing vertically aligned CO_2 to dissociate, producing a defect-free surface and a CO molecule. Table 4.4 shows that as for MgO, the process is strongly exothermic due to the healing of the oxygen vacancy.

Adsorbates aligned along the x- and y-axes are also strongly adsorbed, each forming the same bent geometry as seen previously for F^0-centres. As for adsorption at the O_{5c} site, the structural change is accompanied by a shift of electron density onto CO_2 from magnesium atoms in the first nearest neighbour shell surrounding the vacancy. Once again, the manganese atom does not appear to contribute electron density to the adsorbate. Unlike the undoped MgO surface, the CO_2 in the adsorbed structures over Mn-MgO are rotated such that the carbon atom is directed towards a surface magnesium atom rather than downwards into the vacancy. The same rotation is observed regardless of the dopant position, although it is notable that in the y-axis orientation where the CO_2 had the possibility to rotate towards either manganese or magnesium, the latter is favoured.

Dopant Position	Adsorbate Orientation	B3LYP	B97-3
Below	X	-2.200 (-212.289)	-1.938 (-186.958)
	Z	-3.154 (-304.361)	-2.829 (-272.915)
Side	X	-1.961 (-189.177)	-1.702 (-164.227)
	Y	-2.210 (-213.237)	-1.946 (-187.788)
	Z	-3.096 (-298.734)	-2.766 (-266.915)

Table 4.4: Energy of CO_2 adsorption on Mn-MgO F^0-centres in eV (kJ/mol).

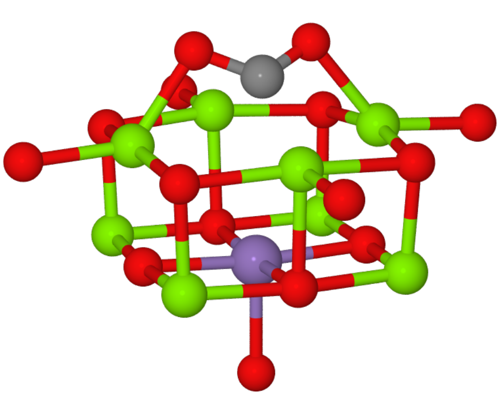
(a) X

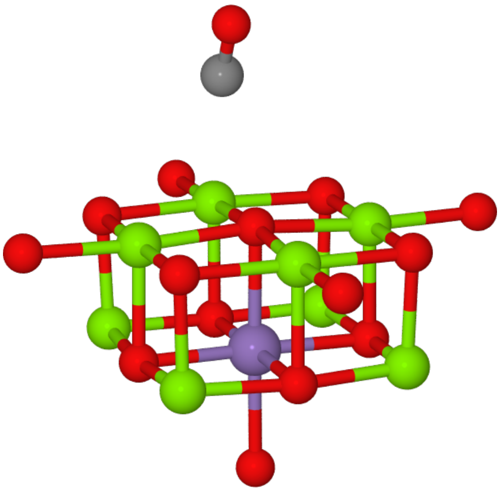
(b) Z

Figure 4.4: CO_2 adsorbed on the Mn-doped MgO(100) surface at an F^0-centre, where the dopant is situated in the second atomic layer. O atoms shown in red, Mg in green, Mn in purple and C in grey.

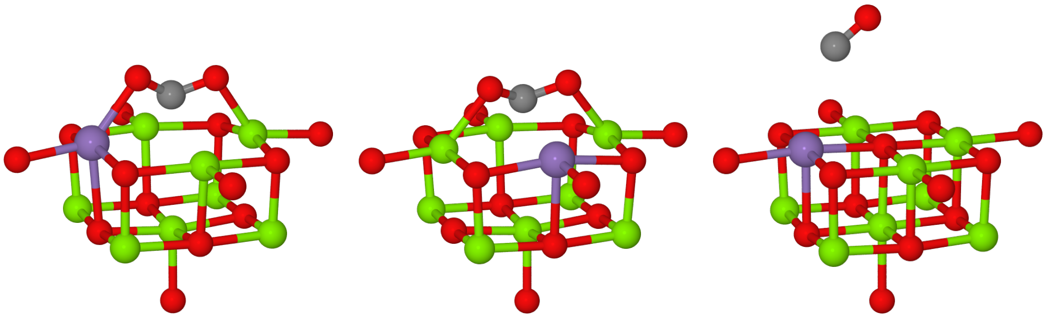
(a) X (b) Y (c) Z

Figure 4.5: CO_2 adsorbed on the Mn-doped MgO(100) surface at an F^0-Centre, where the dopant is situated in the first atomic layer. O atoms shown in red, Mg in green, Mn in purple and C in grey.

F^+-Centre

Both high and low-spin electronic configurations were considered for the addition of CO_2 to an an F^+-centre on the Mn-MgO surface. High spin results are reported in Table 4.5, while low spin results are presented in Table 4.6.

Comparing the E_{ads} data in the two tables, it is clear that some cases are directly equivalent, such as the x-axis aligned adsorbate over a subsurface doped cluster with the B3LYP functional. In these cases, the high spin configuration always gived the lowest energy. Other pairs of calculations, such as those for the cluster described above but using the B97-3 functional, give energies which are substantially different and have the opposite trend. Comparison of the Mulliken populations in these cases provides an explanation: the adsorbate-free defect was able to adopt a low-spin configuration by losing an electron from the vacancy with opposite spin to the electrons on the manganese atom, giving a structure which is nominally "low-spin" but without the pairing of any electrons on the manganese atom.

Enforcing the same low-spin multiplicity for the surface-adsorbate complex causes the alpha channel of the manganese atom to become depleted rather than the vacancy, accompanied by the transfer of a second alpha-channel electron from manganese to the adsorbate. This gives an electronic configuration which is effectively equivalent to ${CO_2}^-/F^0/Mn^{4+}$. Calculations with similar energies for high and low spin configurations simply have one spin channel depleted by the ionization process, while the other channel has its unpaired electron transferred to the adsorbate. The low-spin calculations therefore do not allow for a like-for-like comparison between the surface and surface-adosrbate complex.

The ground state adsorbed structures for CO_2 over Mn-MgO with an F^+-centre and the dopant located in the subsurface position are shown in Figure 4.6. Equivalent structures for the surface-layer dopant are given in Figure 4.7. Regardless of the electron configuration observed, structures for the surface-adsorbate complexes are qualitatively the same - this is not unexpected, as all calculations result in electron transfer onto the adsorbed CO_2 molecule, giving the same bent structures as previously identified for MgO.

Dopant Position	Adsorbate Orientation	B3LYP	B97-3
Below	X	-0.811 (-78.203)	-0.656 (-63.292)
	Z	-1.143 (-110.265)	-1.01 (-97.586)
Side	X	-0.579 (-55.925)	-0.449 (-43.417)
	Y	-0.766 (-73.921)	-0.606 (-58.506)
	Z	-1.077 (-103.888)	-0.939 (-90.653)

Table 4.5: Energy of CO_2 adsorption on high spin Mn-MgO F^+-centres in eV (kJ/mol).

Dopant Position	Adsorbate Orientation	B3LYP	B97-3
Below	X	-0.596 (-57.275)	-2.264 (-218.417)
	Z	-0.948 (-91.501)	-0.932 (-89.925)
Side	X	-1.959 (-189.072)	-2.175 (-209.879)
	Y	-1.340 (-129.376)	-3.049 (-294.142)
	Z	-0.863 (-83.280)	-0.891 (-85.953)

Table 4.6: Energy of CO_2 adsorption on low spin Mn-MgO F^+-centres in eV (kJ/mol).

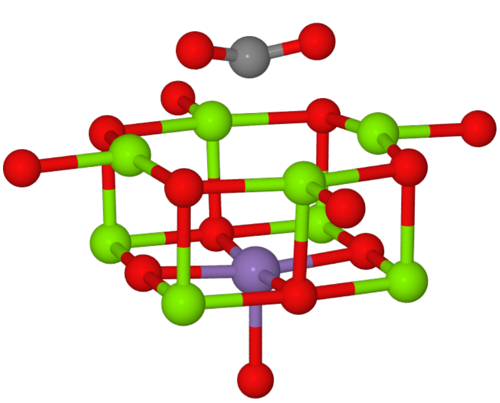

(a) X (b) Z

Figure 4.6: CO_2 adsorbed on the Mn-doped MgO(100) surface at an F^+-Centre, where the dopant is situated in the second atomic layer. O atoms shown in red, Mg in green, Mn in purple and C in grey.

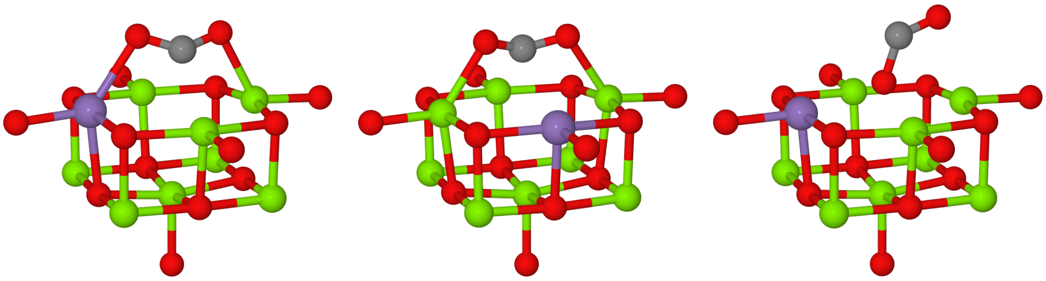

(a) X (b) Y (c) Z

Figure 4.7: CO_2 adsorbed on the Mn-doped MgO(100) surface at an F^+-Centre, where the dopant is situated in the first atomic layer. O atoms shown in red, Mg in green, Mn in purple and C in grey.

F^{2+}-Centre

The ground state adsorbed structures for CO_2 over Mn-MgO with an F^{2+}-centre are shown in Figure 4.8 and Figure 4.9 for clusters with the Mn dopant located in the subsurface and surface layers respectively.

Both the adsorbed structures for z-axis aligned CO_2 (Figure 4.8b and Figure 4.9c) and the corresponding E_{ads} values given in Table 4.7 suggest that no significant interaction between the surface and adsorbate occurs, a finding which is consistent with results for undoped MgO.

For the interactions between the F^{2+}-centre and CO_2 aligned with the x- or y-axes bent adsorbate geometries are observed, corresponding to electron transfer from manganese. The effective electronic configuration has therefore shifted from $CO_2/F^{2+}/Mn^{2+}$ to $CO_2^{-}/F^{2+}/Mn^{3+}$,although part of the charge density does appear to reside on surface magnesium atoms, so the alternative description of $CO_2^{(1-\sigma)-}/F^{(2-\sigma)+}/Mn^{3+}$ may also be appropriate. E_{ads} is positive for each of these adsorbed structures, suggesting a thermodynamically unfavourable local minimum. The energetic balance between Mn^{2+} oxidation and partial reduction of the charge of the F-centre may explain why these minima exist rather than the simple non-interaction observed for MgO.

Dopant Position	Adsorbate Orientation	B3LYP	B97-3
Below	X	0.290 (27.993)	0.553 (53.382)
	Z	-0.081 (-7.818)	-0.095 (-9.149)
Side	X	0.939 (90.591)	1.181 (113.963)
	Y	0.544 (52.537)	0.038 (3.689)
	Z	-0.048 (-4.657)	-0.068 (-6.524)

Table 4.7: Energy of CO_2 adsorption on Mn-MgO F^{2+}-centres in eV (kJ/mol).

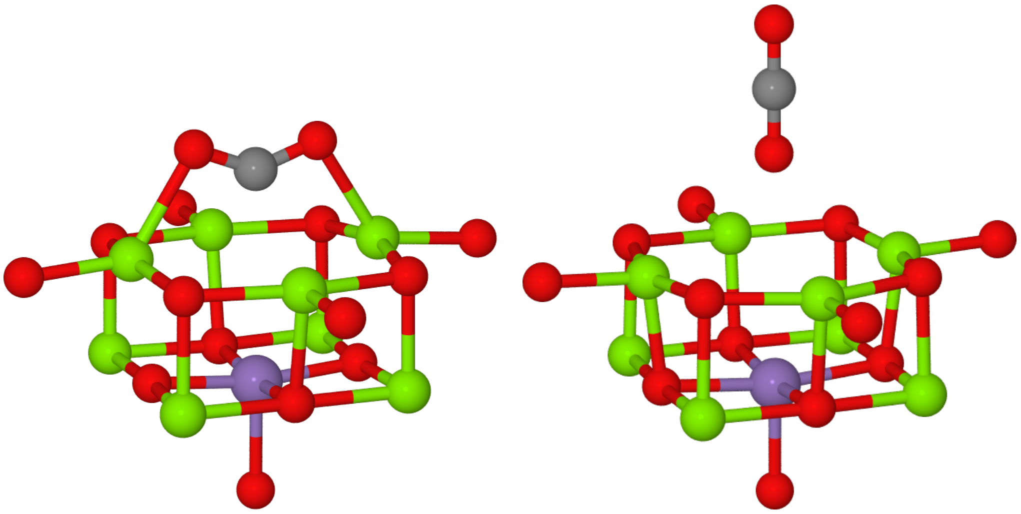

(a) X (b) Z

Figure 4.8: CO_2 adsorbed on the Mn-doped MgO(100) surface at an F^{2+}-Centre, where the dopant is situated in the second atomic layer. O atoms shown in red, Mg in green, Mn in purple and C in grey.

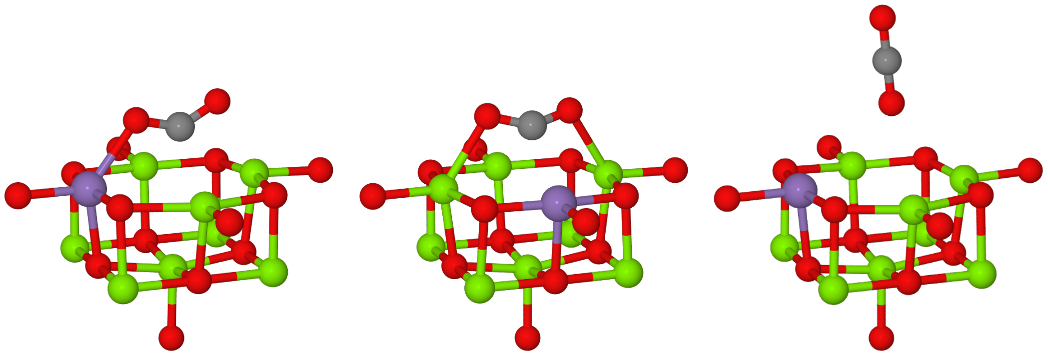

(a) X (b) Y (c) Z

Figure 4.9: CO_2 adsorbed on the Mn-doped MgO(100) surface at an F^{2+}-Centre, where the dopant is situated in the first atomic layer. O atoms shown in red, Mg in green, Mn in purple and C in grey.

4.4 Summary and Implications for Catalysis

Results for the interaction of CO_2 with each of the surface sites considered for Mn-doped MgO are broadly in agreement with those seen for MgO, both in terms of the calculated values for E_{ads} and the ground-state structures observed. The only notable difference is the F^{2+}-centre, where the presence of a redox-active metal does appear to allow for electron transfer onto the adsorbate which would otherwise not be possible.

Calculations for low-spin Mn-MgO do not provide a consistent picture of how electrons may be redistributed during the adsorption process. Taking this into account along with knowlegdge that the high-spin configuration of Mn^{2+} is the experimentally favoured structure in metal oxides, it is clear that a much better representation of the system is provided by calculations for the high spin case, where both the defect formation energies and E_{ads} values are more consistent with results for undoped MgO.

Formation energies for each of the oxygen vacancy defects are reduced by the presence of a manganese dopant. Taken together with the consistent transfer of electrons onto the adsorbate for all defect charge states and most adsorbate geometries, it can be concluded that any catalytic activity observed for MgO would be more likely to be enhanced than degraded by the presence of transition metal dopants.

Chapter 5

MnO for CO_2 Conversion Catalysis

Following the successful application of the QM/MM model to MgO and Mn-doped MgO, work was extended to include calculations on transition metal oxide surface sites. Due to the need for a closed-shell boundary ECP with a similar ionic radius to the transition metal being considered, and the need to ensure that this limitation of having no d-electrons at the boundary would not significantly influence the interaction between the oxide surface and CO_2, work was limited to manganese (II) oxide.

Besides a non-ideal QM/MM boundary, MnO presents the additional complication that the zero kelvin structure reproduced by electronic structure calculations is significantly distorted from that observed at room temperature, adopting a rhombohedral unit cell rather than face-centred cubic. Given that the available interatomic potentials were fitted to room temperature experimental data, their use in a QM/MM calculation without modification would result in a high degree of strain at the interface between the QM and MM regions, reducing the achievable accuracy and possibly preventing the convergence to the ground state entirely. This problem was circumvented *via* the fitting and use of an additional interatomic potential term between nearest-neighbour manganese ions within the MM calculation, leading to the accurate reproduction of the distorted unit cell parameters.

The correlation between structural distortion and antiferromagnetic ordering at the Neel temperature in transition metal oxides has been well understood for some time.[116] In MnO, metal atoms lying within the same (111) plane are found to share the same spin orientation,[117] although it is believed that the magnetic unit cell contains four pairs of AFM-oriented manganese ions, the magnetism of each pair uncorrelated with the other three.[118] Given the complexity of the suggested magnetic cell and the limited impact magnetic ordering was expected to have on catalytic activity, no attempt was made to reproduce the non-collinearity of spins in the present model.

Similarly to Mn-doped MgO, a large proportion of work performed on MnO focuses on bulk magnetic properties, with dilute magnetic semiconductors once again being an important target application.[119] More recently, studies have also highlighted the potential use of MnO for photocatalytic water splitting and CO_2 reduction applications when alloyed with ZnO.[120] Additionally, the (100) MnO surface has been considered for CO_2 adsorption as part of a systematic study of transition metal monoxides.[121] Adsorption on MnO and oxides of heavier first-row transition metals was found to be relatively weak, with the stable half-filled shell of Mn^{2+} being noted as the likely cause of the particularly poor reactivity seen on MnO. Nevertheless, calculations on this relatively stable transition metal oxide (TMO) form an important link between alkali earth oxides and other TMO materials which have lower coordinated surface sites or more readily accessible d-electrons.

As with previous catalytic systems, once challenges related to the implementation of the system of interest within the QM/MM environment had been addressed, the focus of the work moved to oxygen vacancy formation and CO_2 adsorption.

5.1 Computational Approach for MnO

Calculations for the MnO system were performed using the same hemispherical QM/MM cluster setup as that described in Section 4.1, with a total radius of 30Å centred on an oxygen atom or oxygen vacancy. The radius of the relaxing MM region was fixed at 15Å giving a total of around 750 atoms free to undergo ionic relaxation, with the remainder frozen in the lattice positions obtained from a pre-optimisation using the MM code GULP. The number of relaxing atoms was less for MnO clusters than in calculations based on MgO due to the difference in lattice parameters.

The interatomic potential, provided in appendix B, was based on that of Lewis & Catlow,[113] with modifications to extend the cut-off radius and tune the O_{shell}–O_{shell} interaction to an appropriate value in order to reproduce the dielectric constant of MnO as accurately as possible. Additional modifications were necessary to account for the distortion of the structure from the cubic unit cell observed at room temperature (and reproduced by the Lewis-Catlow potential) to the zero kelvin rhombohedral structure. This distortion was included *via* the decomposition of the manganese atoms into two sub-lattices occupying alternating cation sites. Each sub-lattice was given a separate label allowing for the addition of a Lennard-Jones interatomic potential term to include the interaction between manganese atoms with opposing d-electron orientations. By restricting this Mn-Mn term to a 5Å radius, only nearest-neighbour cations having opposite labels were allowed to interact, making the model as faithful as possible to the real super-exchange interaction without the need for a more complex three-body term.

No additional potential terms were included to account for the interactions of the adsorbate with the surface, as the CO_2 molecule is always located directly above the QM part of the surface, with the closest MM atoms at least 5Å away.

Both the B3LYP[69–71] and B97-3[114] functionals were used throughout this section of work to provide a direct comparison with Mn-doped MgO. Unless a specific discrepancy between the two functionals arises, results described will be focused on B3LYP for consistency with earlier work. Similarly, these calculations employed the Def2[73] triple-zeta valence plus polarization (TZVP) basis set for all atoms except Mn, where the same modified version of the Stuttgart RSC basis set was used.

Core electrons for Mn atoms within the QM region of the cluster were represented by a standard ECP.[115] No large-core ECP for Mn^{2+} was available to fulfill the QM/MM boundary role, and so the same Mg^{2+} effective core potentials[74] as used in earlier MgO and MnMgO work were placed on cations at the border of the QM region. This approach is identical to that used in previous studies,[120] and is considered appropriate due to the similarity between Mg^{2+} and Mn^{2+} ionic radii.

As was the case for the Mn-doped MgO cluster, the presence of redox-active transition metal atoms opens up the possibility for a number of different electronic configurations, particularly in the case of the charged oxygen vacancies F^+ and F^{2+}. However, early calculations showed that changes to the multiplicity of the cluster were not reflected by a change in the oxidation state of a single manganese ion, but rather a shift in the magnetic moment for all cations in the QM cluster. Based on the above, as well as findings for MnMgO where the low spin configurations sometimes produced unrealistic results upon the addition of an adsorbate, analysis was restricted to high spin configurations.

Unlike previous calculations, work on MnO required the use of a pre-constructed “initial guess”, in the form of an NWChem molecular orbital vector input file, for the QM calculation due to the AFM ordering of manganese d-electron spins. The starting molecular orbitals for the QM/MM calculation were generated by first performing atomic calculations for each atom within the QM component of the calculation, with each atom having its charge and magnetic moment forced to adopt the value expected within MnO, and then manually constructing an

NWChem input based on the molecular orbital fragments produced by these atomic calculations.

5.2 The MnO (100) Surface

The QM cluster used in MnO calculations closely resembles that for MgO and Mn-MgO, and is shown in Figure 5.1a. Deviation of the lattice constants from the ideal rocksalt structure is reproduced successfully in both QM and MM parts of the calculation, with the resultant cell angle $\alpha = 90.6°$. Figure 5.1b illustrates the arrangement of two antiferromagnetically aligned subdomains each containing cations on alternating (111) planes and how this arrangement is manifested within a small cluster of atoms. The magnetic moments assigned to each set of cations during the assembly of the initial guess were set to have the alpha channel occupied for the five manganese ions shown in purple, while the beta channel was occupied for the remaining four. The total multiplicity was therefore set to six for the unmodified surface as well as F^0 and F^{2+} cases, and seven for the F^+-centre.

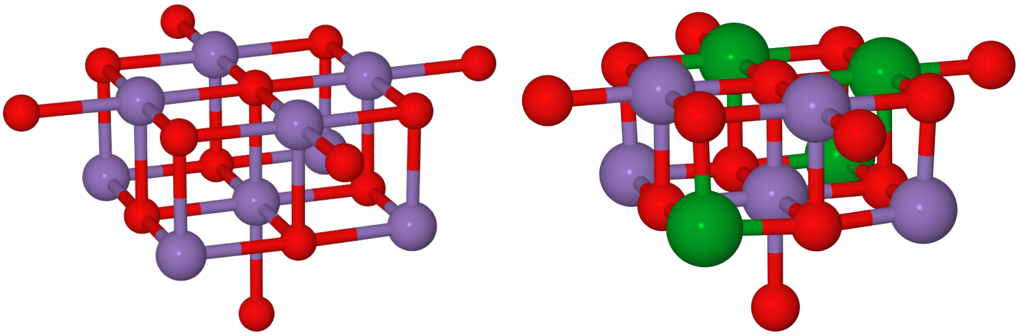
(a) Surface (b) AFM Ordering

Figure 5.1: The QM cluster for an MnO surface. O atoms shown in red, Mn in purple (a) and purple/green depending on magnetic moment (b).

Defect formation energies for oxygen vacancies at the MnO surface are given in Table 5.1. Values are in good agreement with those seen for Mn-doped MgO, suggesting that the addition of extra transition metal centers has minimal impact on the energy required to remove an oxygen atom. This finding suggests that even though the Madelung potential of MnO is expected to be lower than that of MgO, oxygen vacancy formation still results in the localisation of electrons within the defect to give F-centres.

	B3LYP	B97-3
F^0	8.546	8.299
F^+	10.932	10.862
F^{2+}	14.572	14.635

Table 5.1: Defect formation energies for MnO in eV.

As mentioned in Section 5.1, the Mulliken charges observed for oxygen vacancies on MnO suggest that shifts in electron density are averaged over the cations rather than being localised at a single redox site. This may indicate the need for a functional where more Hartree-Fock exchange is included than those used for this study.

5.3 CO_2 Adsorption on the MnO (100) Surface

In a similar manner to the interaction of CO_2 with the O_{5c} site of MgO and Mn-doped MgO, the CO_2-MnO complex forms a carbonate-like structure where electron density is transferred from the surface (primarily the central oxygen atom) onto the adsorbate. The resultant structure, shown in Figure 5.2, has structural features which are essentially identical to those seen on other surfaces. The energy of adsorption, E_{ads}, is somewhat less for MnO than the MgO-based systems, at -0.602 eV (-58.047 kJ/mol) for B3LYP and -0.652 eV (-62.938 kJ/mol) for B97-3. The reduction in stability of the adsorbed species may be attributed to the expansion of the lattice parameter for MnO relative to MgO, resulting in weaker interactions between the surface metal sites and oxygen atoms of the adsorbate.

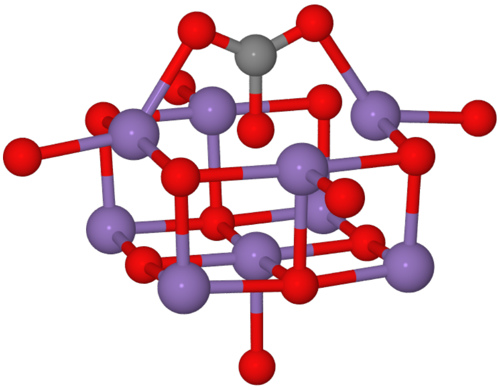

Figure 5.2: CO_2 adsorbed on the MnO(100) surface. O atoms shown in red, Mn in purple and C in grey.

Moving to the electron-rich oxygen vacancies on MnO, results begin to differentiate from earlier work. As before, two adsorbate orientations were considered: one in which the O-C-O axis was aligned along the cluster x-axis ("parallel" orientation) and one where the molecular bonding axis was aligned with the cluster z-direction ("perpendicular" orientation). Despite starting in different orientations, Figure 5.3 shows that both calculations result in the adsorbate occupying a bent and rotated geometry over the F^0 defect. Comparison of E_{ads} for the two systems (table 5.2) confirms that they are essentially identical.

	B3LYP	B97-3
X	-2.568 (-247.736)	-2.234 (-215.589)
Z	-2.567 (-247.668)	-2.232 (-215.356)

Table 5.2: Energy of CO_2 adsorption on the MnO F^0-centre in eV (kJ/mol).

The adsorption energies are approximately the same as those seen when CO_2 dissociates to CO over MgO, suggesting that while electron transfer from the vacancy onto the lower oxygen makes the interaction strongly favourable, interactions between the surface cations and the remaining adsorbate atoms also have a significant contribution. Both manganese subdomains interact with the adsorbate atoms, suggesting that the adsorbed structure is independent of magnetic properties.

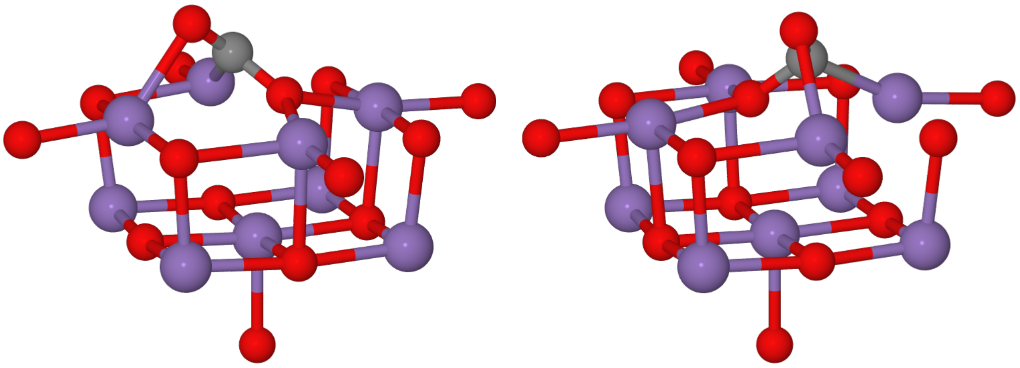
(a) X

(b) Z

Figure 5.3: CO_2 adsorbed on the MnO(100) surface at an F^0-centre. O atoms shown in red, Mn in purple and C in grey.

Progressing to the F^+-centres, we once again see structures which do not depend on the initial orientation of the adsorbate. It is also clear from Figure 5.4 that the same effects seen for the two-electron vacancy are present in the one-electron case, with adsorbed structures being essentially identical to those seen for the F^0-centre. E_{ads} values are somewhat lower at around -1.559 eV (-150.414 kJ/mol), suggesting that the presence of the adsorbate stabilises the localisation of more than one electron - a finding consistent with the MgO surfaces, where both electrons are transferred as part of the dissociation process to CO and a filled vacancy.

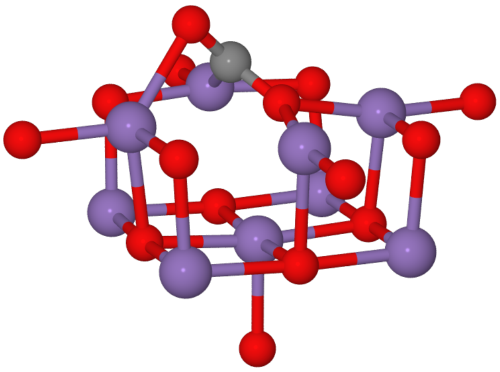
(a) X
(b) Z

Figure 5.4: CO_2 adsorbed on the MnO(100) surface at an F^+-centre. O atoms shown in red, Mn in purple and C in grey.

Finally, results for the F^{2+}-centre show that unlike Mn-MgO where some potential redox activity was observed, the electron deficient oxygen vacancy of MnO is unreactive towards CO_2 in the same manner as MgO. This result would suggest that both the redox site and the stronger Madelung potential provided by the MgO lattice are necessary to induce electron transfer in the F^+ case. E_{ads} values are slightly endothermic for the x-axis aligned structure shown in Figure 5.5a at 0.019 eV (1.836 kJ/mol), while E_{ads} for the tilted structure originally aligned along the z-axis shown in Figure 5.5b are slightly exothermic at -0.0242 eV (-2.334 kJ/mol).

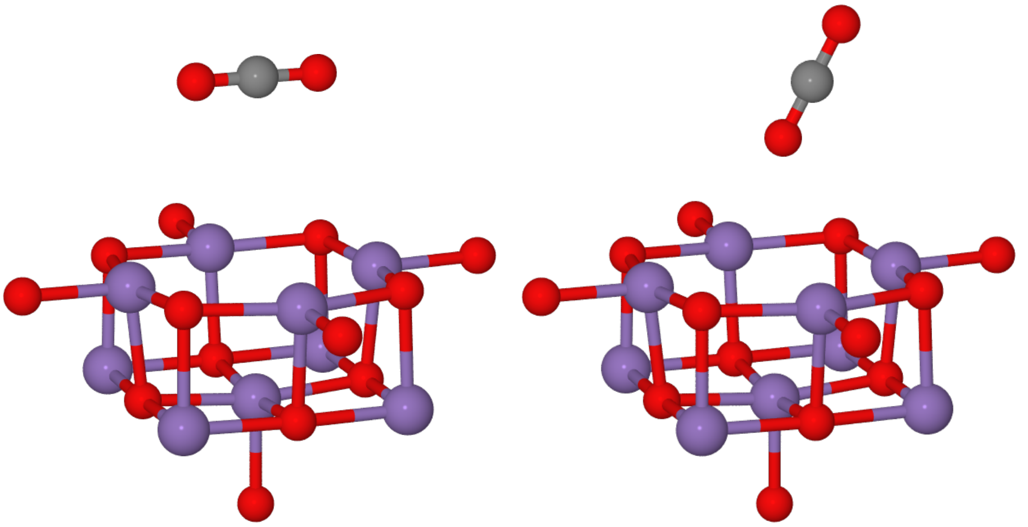

(a) X (b) Z

Figure 5.5: CO_2 adsorbed on the MnO(100) surface at an F^{2+}-centre. O atoms shown in red, Mn in purple and C in grey.

5.4 Summary and Implications for Catalysis

The results for CO_2 adsorption on MnO have shown some important differences relative to the MgO-based surfaces. Firstly, while the defect formation energies for each of the F-centres are approximately the same as seen for Mn-doped MgO, the behaviour of adsorbed CO_2 suggests that electrons are less strongly localised within the vacancy. In particular, the surface-adsorbate complex seen for F^0-centres is interesting because it suggests that an MnO catalyst where oxygen vacancies are an important active site would be less likely to be degraded as a result of CO_2 being decomposed to CO and an oxygen atom to fill the anion site.

The high E_{ads} values for the identical structures seen for F^0 and F^+-centres are significant because they indicate that a CO_2^- activated species at the MnO surface would be fairly stable and long-lived. Also, the rotation of the adsorbed species relative to the CO_2^- intermediates seen for MgO and Mn-MgO brings the carbon atom closer to the surface, making it more accessible to adsorbed hydrogen or other species and aiding the initiation of onwards reactions such as those described in Section 3.4.

Chapter 6

Oxidative Coupling of Methane

As already described in Section 1.3, the conversion of methane to more valuable hydrocarbon products has the potential to to play a crucial role in the future usage of synthetic fuels, as well as optimising the utilisation of current fossil fuel reserves. Here, we investigate the role played by the QM/MM embedding environment in the calculation of reaction barriers with reference to a recent study by Kwapien et al.[29] and earlier ChemShell work on the Li-doped MgO catalyst.[66] Owing to the conceptually simple mechanism for C-H bond activation by LiMgO proposed by Lunsford[27] (but not yet confirmed as the correct one), a significant quantity of work has already been performed for this catalyst system.

Li-doping of MgO for catalytic purposes is usually discussed with reference to the (100) surface owing to its stability. However theoretical work by Scanlon et al. has highlighted the possibility that their lower energies for lithium incorporation may allow other surface terminations to play a role in catalysis.[122]

The importance of lattice polarisation in the Li-MgO system has been discussed previously by Shluger et al.[123] One of the key advantages of ChemShell calculations is the ability to include polarisation effects explicitly within the model rather than relying on *a posteriori* corrections, a factor which may contribute to explaining the differences observed between embedded cluster and periodic slab calculations.

Despite the theoretical interest in this catalyst, experimental work does not generally support the conclusion that localised holes at the oxide surface are responsible for initiating the reaction. A combined experimental and theoretical study found that while Li dopants within MgO preferentially segregate towards the surface, EPR measurements do not support the presence of Li^+O^- centres. The formation of oxygen defects is preferred at low temperatures, with Li_xO surface clusters formed after annealing and then subsequently being desorbed when the temperature is increased further.[104] These findings support earlier experimental work, which suggests that the role of lithium doping in the OCM reaction with an MgO catalyst is to enhance the formation of F-centres.[124] On the other hand, the exchange of hydrogen between surface hydroxyl groups and CH_4 has been observed *via* isotopic labelling, strengthening the argument that the catalyst plays an active role in the reaction process rather than simply bringing reactants together.[125] Regardless of the real role (or lack thereof) played by Li-MgO in CH_4 conversion catalysis, the problem provides an interesting benchmark case for theoretical studies.

6.1 Computational Approach for Li-doped MgO

As with all previous calculations, work on Li-doped MgO made use of a hemispherical QM/MM cluster setup with a total radius of 30Å centred on an oxygen atom. The radius of the relaxing MM region was fixed at 15Å resulting in a total of around 850 atoms undergoing ionic relaxation with the remainder frozen in the lattice positions obtained from a pre-optimisation using the MM code GULP. The QM region consisted of four nearest-neighbour shells around an oxygen atom at the centre of the cluster, with a total of around 25 atoms included depending on the nature of the adsorbate.

The interatomic potential, provided in appendix B, was based on that of Lewis & Catlow,[113] with modifications to extend the cut-off radius and tune the O_{shell}–O_{shell} interaction to an appropriate value in order to reproduce the dielectric constant of MgO as accurately as possible. An additional term for the Li–O interaction was taken from the work of Bush et al.[126] and modified to have the same 12Å cut-off as all other atoms.

In the same vein as Mn-doped MgO and MnO, the Li-MgO system included shell components on cations as well as anions with the aim of improving the description of electronic polarisation within the system. No additional potential terms were included to account for the interactions of the adsorbate with the surface, as the H_2 and CH_4 molecules were always located directly above the QM part of the surface, with the closest MM atoms at least 5Å away. The B3LYP[69–71] used throughout this section of work, in order to provide a direct comparison with recent work by Kwapien et al.[29]

Li-doped MgO calculations employed the Def2[73] triple-zeta valence plus polarization (TZVP) basis set for all atoms. No modification of the basis set was deemed necessary as the TZVP basis set for light elements (H, Li, C and Mg in particular) do not contain a significant number of highly diffuse functions, an effect which also allows us to disregard the effect of basis set superposition errors. As was the case for previous MgO-based clusters, effective core potentials[74] were placed on cations at the border of the QM region to act as the QM/MM boundary.

As the catalytic mechanism for LiMgO proposed by Lunsford is reliant on the presence of an $O^{\bullet-}$ species,[27] all calculations employed a doublet electronic configuration.

6.2 Homolytic Dissociation of H_2

In order to test the effectiveness of the QM/MM setup for the catalytic system being investigated in this section of the work, a series of prototype calculations were performed in which the CH_4 adsorbate was replaced with H_2:

$$\mathrm{O}^{\bullet-} + 2\,\mathrm{H}_2 \leftrightharpoons \mathrm{OH}^- + \mathrm{H}^\bullet \tag{6.1}$$

The similarity between C-H and H-H bonds allows us to conclude that if H_2 dissociation is observed with a reasonable reaction pathway and transition state, the calculations will also perform well for CH_4. Using H_2 as a prototypical system provides the minor advantage of having a slightly less complex electronic structure than CH_4, but the primary benefit is due to the increased symmetry of the system, from C_{3v} to C_{4v}. The higher symmetry structure for each stage of the H_2 dissociation process makes the optimisation of a transition state pathway somewhat simpler, allowing for the analysis of all other aspects of the calculation without the unnecessary expense of a lengthy nudged elastic band calculation.

Previous calculations focused on the interaction of H_2 with MgO and LiMgO have confirmed that the presence of the lithium dopant opens up the possibility for homolytic dissociation of the hydrogen molecule.[127] Within the calculations presented here, analysis of the Mulliken spin density for the surface before H_2 dissociation confirms the presence of a single unpaired electron (and, by extension, an electron hole) localised on the oxygen atom at the cluster origin. 93% of the unpaired electron density is found on the oxygen atom, with the remainder distributed over the nearest neighbour surface magnesium atoms. Once the homolytic dissociation of H_2 is complete, the unpaired electron density is completely localised on the gas-phase hydrogen atom. The high degree of electron localisation observed in both the initial and final structures suggests that the B3LYP functional includes a sufficient quantity of Hartree-Fock exchange to correctly model the homolytic dissociation reaction.

The calculated dissociation energy for H_2 over a Li-doped MgO (100) surface was -0.308 eV (-29.658 kJ/mol). The energy barrier identified for the reaction was 0.109 eV (10.525 kJ/mol). This barrier is shown in Figure 6.1, along with the initial, transition state and final structures shown in 6.2.

Previous theoretical studies of the interaction between Li-doped MgO and H_2 have focused on lower coordinated sites such as O_{3c} and O_{4c} using Hartree-Fock and MP2 methods, and are therefore not directly comparable with the work presented here.[128] However, the results presented in this section allow us to be confident that similar calculations for CH_4 will be effective at providing insight into the proposed catalytic mechanism for the oxidative coupling of methane, as the systems essentially differ only in their computational complexity.

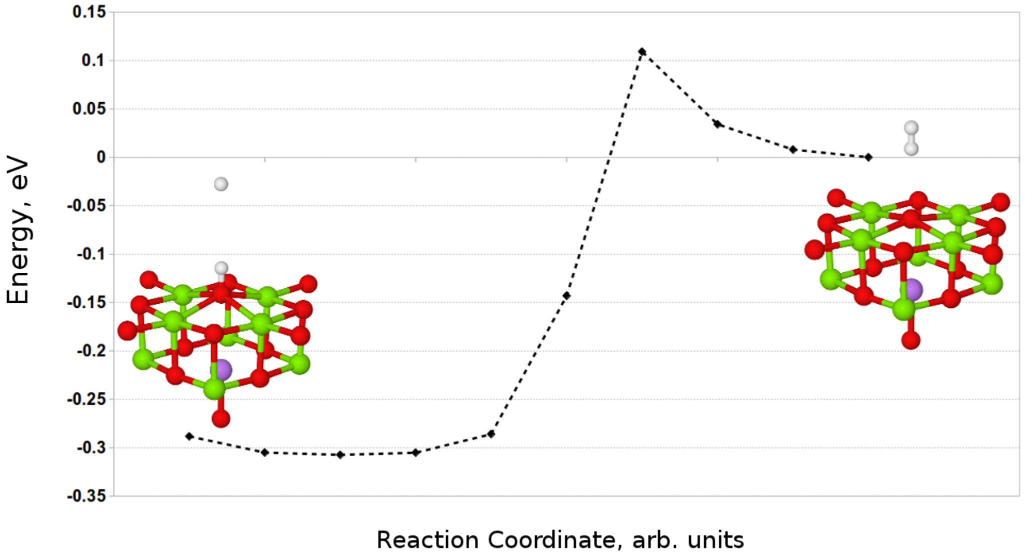

Figure 6.1: Reaction profile for the adsorption of H_2 at the (100) surface of LiMgO, obtained using the NEB method with 10 images. Counterpoise corrections not included.

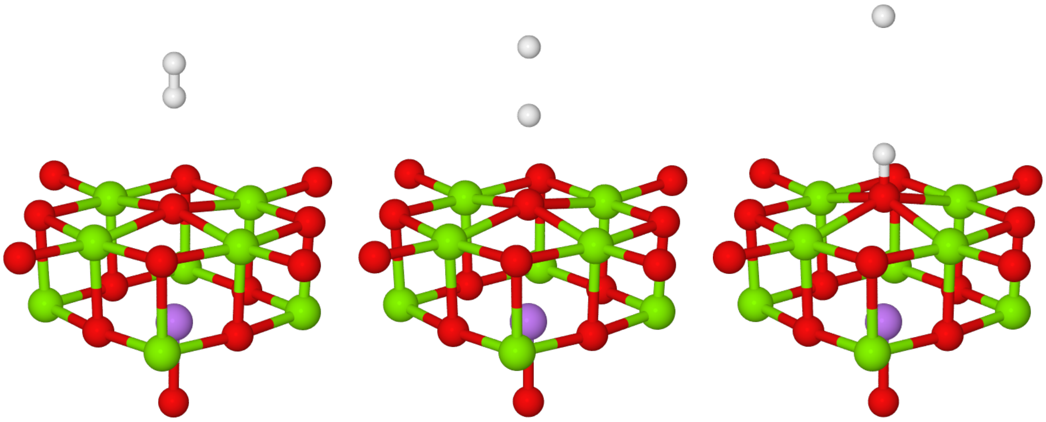

(a) Elevated (b) Transition state (c) Adsorbed

Figure 6.2: QM region structures for H_2 dissociation at the LiMgO (100) surface. O atoms shown in red, Mg in green, Li in purple and H in white.

6.3 Homolytic Dissociation of CH_4

As already noted, some debate exists regarding the energy barrier for the homolytic C-H bond splitting reaction over a Li-doped MgO catalyst. While experimental work has generally suggested that the [Li^+O^-] active site does not play a pivotal role in the reaction process, there is value in studying the reaction as a method for gaining a better understanding of how various components of a calculation setup influence the results. In the comparative study presented by Kwapien et al., the effect of the embedding environment (or lack thereof, in the case of small cluster calculations) on the homolytic dissociation activation barrier was investigated.[29] These results were at odds with earlier Chemshell work,[66] which used a similar embedding environment to that used throughout this thesis, but which did not include a complete relaxation of the reaction pathway using the nudged elastic band method. Work presented in this section aims to reconcile the observed difference.

Analysis of the Mulliken spin density for the surface before CH_4 dissociation shows unpaired electron localisation behaviour which is essentially identical to that seen for H_2, with a single electron (and, by extension, an electron hole) localised on the oxygen atom at the cluster origin. As seen previously, 93% of the unpaired electron density is found on the oxygen atom, with the remainder distributed over the nearest neighbour surface magnesium atoms. Homolytic dissociation of CH_4 leads to the complete localisation of the unpaired electron on the gas-phase CH_3 species.

The dissociation energy for the reaction was found to be -0.315 eV (-30.411 kJ/mol), in good agreement with earlier Chemshell calculations.[66] However, the energy barrier identified for the homolytic dissociation of CH_4 by the LiMgO catalyst was 0.311 eV (29.962 kJ/mol). This result is in good agreement with that seen by Kwapien et al. using an embedded cluster model with no dispersion correction, but is significantly lower than that observed in the previous Chemshell study. The barrier for CH_4 dissociation is shown in Figure 6.3, along with the initial, transition state and final structures shown in 6.4. Comparing the reaction pathway in Figure 6.3 with that in Figure 8 of reference 66, it may be noted that the observed shape and position of the transition state relative to the initial and final structures is similar, but with a more abrupt transition, i.e. the nudged elastic band pathway had fewer intermediate structures with energies which were elevated relative to the starting structure. The reaction pathway obtained in reference 66 did not use a nudged elastic band method, with the transition state instead being determined *via* relaxation of the structure for a range of fixed surface-adsorbate separation distances. The procedure used in the previous work does not allow for the same degree of structural flexibility in the transition between tetrahedral CH_4 and planar CH_3 as a nudged elastic band calculation, providing one possible explanation for the difference in barriers observed. No reaction pathway was provided by Kwapien et al. in reference 29 for comparison. When commenting on the discrepancy between their work and the earlier Chemshell calculations, Kwapien et al. speculated that both the lack of a full reaction pathway optimisation and the lack of dispersion corrections in the Chemshell work may have been contributing factors. While we agree that the first effect is likely to have played a role, the close agreement between results presented here and those of Kwapien et al. suggests that dispersion corrections do not play a critical role in explaining the discrepancies observed - a conclusion supported by the relatively small effect of including dispersion shown in Table 1 of reference 29.

The results presented here, combined with those of references 29 and 66, allow us to conclude that the use of an embedded cluster or periodic boundary condition calculation is a requirement for obtaining accurate reaction barriers. We can also state with some confidence that a simple linearly interpolated reaction pathway is not sufficient to provide the correct result, with the nudged elastic band or a similar method being required. Additional work should be performed using other functionals with better theoretical grounding than B3LYP, or alternatively a higher level of theory such as MP2 or CCSD(T), in order to confirm the accuracy of the calculated barrier.

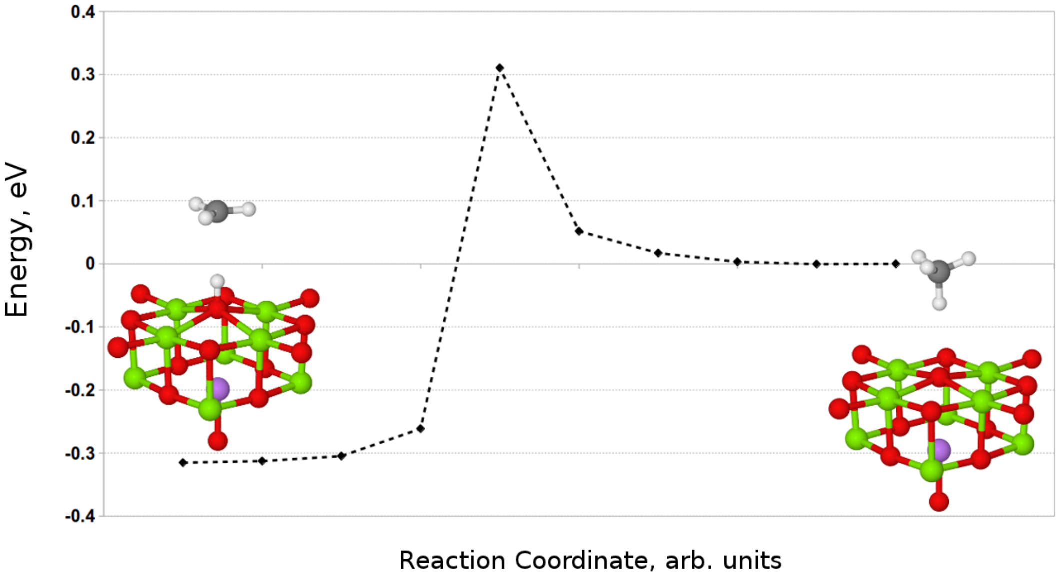

Figure 6.3: Reaction profile for the adsorption of CH_4 at the (100) surface of LiMgO, obtained using the NEB method with 10 images. Counterpoise corrections not included.

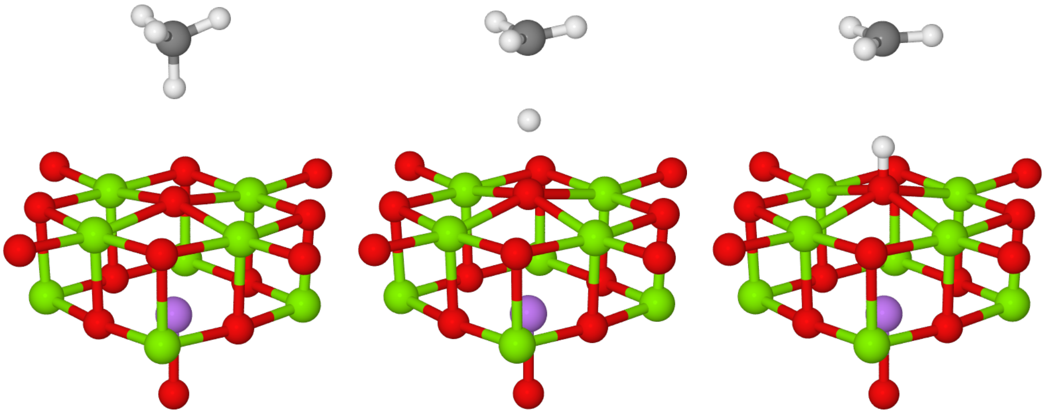

(a) Elevated (b) Transition state (c) Adsorbed

Figure 6.4: QM region structures for CH_4 dissociation at the LiMgO (100) surface. O atoms shown in red, Mg in green, Li in purple, H in white and C in grey.

Chapter 7

Conclusions

This final chapter provides a summary of the work described in Chapters 3, 4, 5 and 6, in addition to some comments on possible future extensions to the study.

7.1 Summary

In Chapter 3, initial work to understand the interaction between CO_2 and various sites at the MgO (100) terrace is described. The results show a stronger interaction between the adsorbate and the five-coordinate oxygen site than observed in earlier work, and a range of different behaviour for the interaction between CO_2 and an oxygen vacancy which primarily depends on the charge state of the defect. In particular, the interaction between an F^+-centre and CO_2 results in the formation of a CO_2^- ion, which may undergo subsequent reactions with hydrogen to form useful products such as methane and methanol.

In Chapter 4, the work was extended to include a transition metal dopant in the vicinity of the adsorption site or oxygen defect. Formation energies for each of the F-centres are lowered by the presence of a Mn^{2+} ion, and the tendency for electrons to be transferred onto the adsorbed CO_2 is maintained. We therefore conclude that transition metal doping should enhance any catalytic activity observed for MgO, but note that even with an alternative transition metal dopant which is more able to undergo redox reactions than manganese, the formation energy of oxygen vacancies is still likely to be too high to allow MgO to achieve high levels of catalytic activity.

In Chapter 5, the concept of improving the catalytic performance of an oxide by adding redox centres is extended to a full transition metal oxide, MnO. MnO was found to have a similarly high formation energy for oxygen vacancies as seen in MgO and Mn-doped MgO, suggesting that the high Madelung potential of rock-salt structured ionic compounds cannot be overcome by simple redox reactions in this case. Other transition metal oxides in which the cation may more readily be converted to the 3+ oxidation state must be examined to confirm the extent of this limitation, but even if an oxygen vacancy can be formed cheaply at a TMO surface it is likely that the catalytic activity of the system would benefit from the active site having a lower coordination number. Adsorption of CO_2 at the five-coordinate oxygen surface site of MnO was qualitatively the same as the interaction with MgO or Mn-doped MgO, but weaker. Where the adsorption site was an F-centre, identical adsorbed geometries were observed regardless of whether the vacancy contained one or two localised electrons.

Chapter 6 attempts to address an open question related to the role of lithium doping in the oxidative coupling of methane reaction. We find, in agreement with a recent theoretical study, that the observed reaction barrier is lower than previously thought and the difference observed between results presented here and earlier work using the Chemshell model is most likely due to the use of a more rigorous reaction pathway optimisation.

Overall, we have shown that even simple metal oxide surfaces may display a wide range of behaviours when an adsorbate capable of receiving an electron is present. Factors such as the charge state of a vacancy, presence of a redox-active cation and distortion from the ideal cell geometry all influence the tendency of the surface to donate an electron. The cost for the formation of an oxygen vacancy and corresponding thermodynamic driving force to return the surface to its defect-free state will remain a problem and there will be a need to study systems where this energy is reduced. The present study, by focussing on some of the fundamental factors relating to CO_2 activation over oxides, will give valuable guidance as to the development of new materials able to effect this crucial process.

7.2 Future Work

The following is a list of possible future directions for ChemShell-based work on catalysis at oxide surfaces.These include work which may be performed immediately using the current version of ChemShell as well as technical developments which would allow the code to be applied to a wider range of problems.

Other Alkali Earth Oxides

While MgO is by far the most studied of the alkali earth oxides within the field of computational chemistry, comparisons with CaO and SrO often prove useful in illustrating how significant the effect of the Madelung potential at oxide surface sites can be. Comparisons of CO_2 adsorption at each of these surfaces has been a feature of a number of previous theoretical and experimental studies.[80,82,86] Given that the presented results for MgO differ substantially from those seen in the past, it would be worthwhile to repeat the QM/MM study performed here for more polarisable materials in order to determine if the effect of long-range interactions is consistent.

A set of results for MgO, CaO and CrO using the same interatomic potentials would allow for the effect of cation polarisation on CO_2 adsorption to be analysed, as well as extending our knowledge of solid chemisorption materials which may be used for carbon capture and storage in the future.

Jost-type Correction for a Dipole

Given the importance of surface polarisation observed within this work, and the fact that many other codes (in particular, those employing periodic boundary conditions) do not have the capability to include this effect directly, it may be beneficial to develop a new *a posteriori* correction for use in cases where QM/MM calculations are not feasible. This would combine elements of the Jost correction (eq. 3.2) and the Born-Onsager description of dipole solvation (eq. 3.3).

Development of an analytic expression for surface dipole effects would benefit from the work described above in which other alkali earth oxides are considered. Once formulated, an analytic expression for dipolar effects could be used to quantify the extent to which periodic boundary conditions introduce errors into many calculations and determine the optimum cell size to provide a balance between accuracy and computational cost.

Low-coordinated Sites

A common extension to earlier work on the interaction between CO_2 and MgO is the inclusion of corner and step sites, which more capable of undergoing changes to their electronic or physical structure than terrace sites. Although low-coordinated sites represent only a small fraction of the available crystal surface in many cases, theire relevance to catalytic processes has increased greatly as the preparation of nanostructured materials has become commonplace. It would therefore be highly desirable to include a procedure for generating surface sites other than terraces for use within a QM/MM calculation.

For materials such as MgO which are relatively unreactive, the edge and corner sites have particular significance as they are often the only sites where defects and vacancies can be observed to exist experimentally. The ability to model these sites is therefore crucial to obtaining a reasonable match between experimental and theoretical adsorption energies and reaction barriers.

Two distinct routes could be taken to adapt the ChemShell cluster generation routine to allow for calculations on low coordinated sites. By removing the boundary point charges and producing a QM/MM cluster with a shape approximating that of a real crystal rather than a sphere or hemisphere, any arbitrarily chosen surfaces or low coordinated sites may be investigated. The primary disadvantage of this method is the loss of a well-defined method for guaranteeing the electrostatics of the QM region are accurate due to the removal of the fitted point charges at the cluster boundary. The second route to obtaining low-coordinated sites is based on generating a standard ChemShell cluster and cleaving along a series of planes, removing atoms until a sub-cluster remains with the desired set of surfaces, edges and corner sites. The second method has the advantage of perserving the fitted point charges, but is much more labour intensive.

Alternative Transition Metal Dopants

In Chapter 4 the effects of a transition metal on the potential activity of CO_2 were discussed, but with reference to a cation which by virtue of its stable half-filled d-subshell was resistant to changes in its oxidation state. Other metals, while providing a worse fit to the lattice parameters of MgO, would be more capable of significantly altering the electronic structure of F-centres and subsequently providing alternative reaction pathways once CO_2 is introduced. It is unlikely, however, that transition metal doping with a more redox-active cation would be sufficient to make MgO a viable catalyst for CO_2 recycling, as we have shown that even in MnO the formation of oxygen vacancies is energetically costly.

Fitted ECPs for Transition Metals

The next stage of development for the QM/MM model within ChemShell includes a procedure to fit new ECPs for use within the embedding environment. In the initial stage, this allows for the fitting of large-core ECPs for transition metals which include the effect of d-electrons within the average potential. A further development, which allows a different ECP to be applied to each of the alpha and beta spin channels, allows magnetic effects such as the AFM ordering observed within MnO to be maintained across the QM/MM boundary region. Implementation of the new ECPs has been completed by Dr Andrew Logsdail at UCL and will be used in future studies of transition metal oxides following tests on MnO where the fitted ECPs are compared to the magnesium boundary region used within this work.

References

[1] G. A. Olah, G. K. S. Prakash and A. Goeppert, *J. Am. Chem. Soc.*, 2011, **133**, 12881–12898.

[2] A. Goeppert, M. Czaun, J.-P. Jones, G. K. Surya Prakash and G. A. Olah, *Chem. Soc. Rev.*, 2014, 7995–8048.

[3] R. J. Pearson, M. D. Eisaman, J. W. G. Turner, P. P. Edwards, Z. Jiang, V. L. Kuznetsov, K. A. Littau, L. Di Marco and S. R. G. Taylor, *Proc. IEEE*, 2012, **100**, 440–460.

[4] NOAA/ESRL data, see http://www.esrl.noaa.gov/gmd/ccgg/trends/.

[5] J. Petit, J. Jouzel, D. Raynaud, N. Barkov, J. Barnola, I. Basile, M. Bender, J. Chappellaz, M. Davis, G. Delaygue, M. Delmotte, V. Kotlyakov, M. Legrand, V. Lipenkov, C. Lorius, L. Pepin, C. Ritz, E. Saltzman and M. Stievenard, *Nature*, 1999, **399**, 429–436.

[6] IPCC findings, see http://www.ipcc.ch/publications_and_data/ar4/wg1/en/tssts-2.html.

[7] T. W. Patzek and G. D. Croft, *Energy*, 2010, **35**, 3109 – 3122.

[8] G. A. Olah, *Angew. Chem. Int. Ed.*, 2005, **44**, 2636–2639.

[9] T. B. Reed and R. M. Lerner, *Science*, 1973, **182**, pp. 1299–1304.

[10] Z. Jiang, T. Xiao, V. L. Kuznetsov and P. P. Edwards, *Philos. Trans. R. Soc. A-Math. Phys. Eng. Sci.*, 2010, **368**, 3343–3364.

[11] T. A. Semelsberger, R. L. Borup and H. L. Greene, *J. Power Sources*, 2006, **156**, 497 – 511.

[12] K. S. Lackner, S. Brennan, J. M. Matter, A.-H. A. Park, A. Wright and B. van der Zwaan, *Proc. Natl. Acad. Sci. U.S.A.*, 2012, **109**, 13156–13162.

[13] K. S. Lackner, *Energy*, 2013, **50**, 38 – 46.

[14] S. Wang, S. Yan, X. Ma and J. Gong, *Energy Environ. Sci.*, 2011, **4**, 3805–3819.

[15] S. Choi, J. H. Drese and C. W. Jones, *ChemSusChem*, 2009, **2**, 796–854.

[16] G. Liu, D. Willcox, M. Garland and H. Kung, *J. Catal.*, 1985, **96**, 251 – 260.

[17] Y. Choi, K. Futagami, T. Fujitani and J. Nakamura, *Appl. Catal. A*, 2001, **208**, 163 – 167.

[18] M. Saito, T. Fujitani, M. Takeuchi and T. Watanabe, *Appl. Catal. A*, 1996, **138**, 311 – 318.

[19] Y. Zhang, Q. Sun, J. Deng, D. Wu and S. Chen, *Appl. Catal. A*, 1997, **158**, 105 – 120.

[20] J. Tabatabaei, B. H. Sakakini and K. C. Waugh, *Catal. Lett.*, 2006, **110**, 77–84.

[21] K. C. Waugh, *Catal. Lett.*, 2012, **142**, 1153–1166.

[22] M. Kurtz, J. Strunk, O. Hinrichsen, M. Muhler, K. Fink, B. Meyer and C. Woll, *Angew. Chem.-Int. Edit.*, 2005, **44**, 2790–2794.

[23] J. Nakamura, T. Uchijima, Y. Kanai and T. Fujitani, *Catal. Today*, 1996, **28**, 223 – 230.

[24] H. Sakurai and M. Haruta, *Catal. Today*, 1996, **29**, 361 – 365.

[25] M. Haruta, A. Ueda, S. Tsubota and R. T. Sanchez, *Catal. Today*, 1996, **29**, 443 – 447.

[26] H. Sakurai, S. Tsubota and M. Haruta, *Appl. Catal. A*, 1993, **102**, 125 – 136.

[27] J. H. Lunsford, *Angew. Chem. Int. Ed.*, 1995, **34**, 970–980.

[28] D. Lewis, R. Grimes and C. Catlow, *J. Mol. Catal. A-Chem.*, 1995, **100**, 103–114.

[29] K. Kwapien, J. Paier, J. Sauer, M. Geske, U. Zavyalova, R. Horn, P. Schwach, A. Trunschke and R. Schlgl, *Angew. Chem. Int. Ed.*, 2014, **53**, 8774–8778.

[30] S. French, A. Sokol, S. Bromley, C. Catlow and P. Sherwood, *Top. Catal.*, 2003, **24**, 161–172.

[31] S. Bromley, S. French, A. Sokol, C. Catlow and P. Sherwood, *J. Phys. Chem. B*, 2003, **107**, 7045–7057.

[32] Y. Yang, J. Evans, J. A. Rodriguez, M. G. White and P. Liu, *Phys. Chem. Chem. Phys.*, 2010, **12**, 9909–9917.

[33] S. French, A. Sokol, S. Bromley, C. Catlow, S. Rogers, F. King and P. Sherwood, *Angew. Chem.-Int. Edit.*, 2001, **40**, 4437–4440.

[34] G. Dutta, A. A. Sokol, C. R. A. Catlow, T. W. Keal and P. Sherwood, *ChemPhysChem*, 2012, **13**, 3453–3456.

[35] T. W. Keal, P. Sherwood, G. Dutta, A. A. Sokol and C. R. A. Catlow, *Proc. R. Soc. A-Math. Phys. Eng. Sci.*, 2011, **467**, 1900–1924.

[36] A. Sokol, S. Bromley, S. French, C. Catlow and P. Sherwood, *Int. J. Quantum Chem.*, 2004, **99**, 695–712.

[37] S. French, A. Sokol, J. To, C. Catlow, N. Phala, G. Klatt and E. van Steen, *Catal. Today*, 2004, **93-5**, 535–540.

[38] K. Fink, *Phys. Chem. Chem. Phys.*, 2006, **8**, 1482–1489.

[39] H. Nakatsuji and Z.-M. Hu, *Int. J. Quantum Chem.*, 2000, **77**, 341–349.

[40] Z.-M. Hu and H. Nakatsuji, *Chem. Phys. Lett.*, 1999, **313**, 14 – 18.

[41] X. Ding, L. De Rogatis, E. Vesselli, A. Baraldi, G. Comelli, R. Rosei, L. Savio, L. Vattuone, M. Rocca, P. Fornasiero, F. Ancilotto, A. Baldereschi and M. Peressi, *Phys. Rev. B*, 2007, **76**, 195425.

[42] T. Kakumoto and T. Watanabe, *Catal. Today*, 1997, **36**, 39 – 44.

[43] J. Ye, C. jun Liu, D. Mei and Q. Ge, *J. Catal.*, 2014, **317**, 44 – 53.

[44] P. Liu, Y. Choi, Y. Yang and M. G. White, *J. Phys. Chem. A*, 2010, **114**, 3888–3895.

[45] B. Chan and L. Radom, *J. Am. Chem. Soc.*, 2006, **128**, 5322–5323.

[46] ChemShell, a Computational Chemistry Shell, see www.chemshell.org.

[47] P. A. M. Dirac, *Math. Proc. Cambridge*, 1930, **26**, 376–385.

[48] D. M. Ceperley and B. J. Alder, *Phys. Rev. Lett.*, 1980, **45**, 566–569.

[49] C. Skylaris, P. Haynes, A. Mostofi and M. Payne, *J. Chem. Phys.*, 2005, **122**, year.

[50] M. Gell, J. M. Luis, M. Sol and M. Swart, *J. Phys. Chem. A*, 2008, **112**, 6384–6391.

[51] B. G. Dick and A. W. Overhauser, *Phys. Rev.*, 1958, **112**, 90–103.

[52] S. Metz, J. Kstner, A. A. Sokol, T. W. Keal and P. Sherwood, *WIREs Comput Mol Sci*, 2014, **4**, 101–110.

[53] J. Kaestner, J. M. Carr, T. W. Keal, W. Thiel, A. Wander and P. Sherwood, *J. Phys. Chem. A*, 2009, **113**, 11856–11865.

[54] P. Sherwood, A. de Vries, M. Guest, G. Schreckenbach, C. Catlow, S. French, A. Sokol, S. Bromley, W. Thiel, A. Turner, S. Billeter, F. Terstegen, S. Thiel, J. Kendrick, S. Rogers, J. Casci, M. Watson, F. King, E. Karlsen, M. Sjovoll, A. Fahmi, A. Schafer and C. Lennartz, *Theochem-J. Mol. Struct.*, 2003, **632**, 1–28.

[55] M. Guest, I. Bush, H. Van Dam, P. Sherwood, J. Thomas, J. Van Lenthe, R. Havenith and J. Kendrick, *Mol. Phys.*, 2005, **103**, 719–747.

[56] M. Valiev, E. Bylaska, N. Govind, K. Kowalski, T. Straatsma, H. V. Dam, D. Wang, J. Nieplocha, E. Apra, T. Windus and W. de Jong, *Comput. Phys. Commun.*, 2010, **181**, 1477 – 1489.

[57] J. Gale, *J. Chem. Soc.-Faraday Trans.*, 1997, **93**, 629–637.

[58] J. Gale and A. Rohl, *Mol. Simul.*, 2003, **29**, 291–341.

[59] J. Gale, *Z. Kristall.*, 2005, **220**, 552–554.

[60] http://www.hector.ac.uk.

[61] http://www.archer.ac.uk.

[62] http://www.cfi.ses.ac.uk/iridis.

[63] https://wiki.rc.ucl.ac.uk/wiki/Legion.

[64] http://www.stfc.ac.uk/Hartree/Default.aspx.

[65] G. Pacchioni, *ChemPhysChem*, 2003, **4**, 1041–1047.

[66] C. Catlow, S. French, A. Sokol and J. Thomas, *Philos. Trans. R. Soc. A-Math. Phys. Eng. Sci.*, 2005, **363**, 913–936.

[67] C. A. Downing, A. A. Sokol and C. R. A. Catlow, *Phys. Chem. Chem. Phys.*, 2014, **16**, 184–195.

[68] C. A. Downing, A. A. Sokol and C. R. A. Catlow, *Phys. Chem. Chem. Phys.*, 2014, **16**, 21153–21156.

[69] A. Becke, *J. Chem. Phys.*, 1993, **98**, 5648–5652.

[70] C. Lee, W. Yang and R. Parr, *Phys. Rev. B*, 1988, **37**, 785–789.

[71] P. Stephens, F. Devlin, C. Chablowski and M. Frisch, *J. Phys. Chem.*, 1994, **98**, 11623–11627.

[72] J. Paier, M. Marsman and G. Kresse, *J. Chem. Phys.*, 2007, **127**, 024103.

[73] F. Weigend and R. Ahlrichs, *Phys. Chem. Chem. Phys.*, 2005, **7**, 3297–3305.

[74] P. Fuentealba, L. Vonszentpaly, H. Preuss and H. Stoll, *J. Phys. B-At. Mol. Opt. Phys.*, 1985, **18**, 1287–1296.

[75] P. Cox and A. Williams, *Surf. Sci.*, 1986, **175**, L782–L786.

[76] P. Sushko, J. Gavartin and A. Shluger, *J. Phys. Chem. B*, 2002, **106**, 2269–2276.

[77] P. Sushko, A. Shluger and C. Catlow, *Surf. Sci.*, 2000, **450**, 153–170.

[78] E. Scorza, U. Birkenheuer and C. Pisani, *J. Chem. Phys.*, 1997, **107**, 9645–9658.

[79] A. Ferrari and G. Pacchioni, *J. Phys. Chem.*, 1995, **99**, 17010–17018.

[80] M. Jensen, L. Pettersson, O. Swang and U. Olsbye, *J. Phys. Chem. B*, 2005, **109**, 16774–16781.

[81] G. Pacchioni, *Surf. Sci.*, 1993, **281**, 207–219.

[82] G. Pacchioni, J. Ricart and F. Illas, *J. Am. Chem. Soc.*, 1994, **116**, 10152–10158.

[83] W. Schneider, *J. Phys. Chem. B*, 2004, **108**, 273–282.

[84] J. Baltrusaitis, C. Hatch and R. Orlando, *J. Phys. Chem. A*, 2012, **116**, 7950–7958.

[85] D. Ochs, M. Brause, B. Braun, W. Maus-Friedrichs and V. Kempter, *Surf. Sci.*, 1998, **397**, 101–107.

[86] H. Tsuji, A. Okamura-Yoshida, T. Shishido and H. Hattori, *Langmuir*, 2003, **19**, 8793–8800.

[87] H. Tsuji and H. Hattori, *ChemPhysChem*, 2004, **5**, 733–736.

[88] H. Tsuji, T. Shishido, A. Okamura, Y. Gao, H. Hattori and H. Kita, *J. Chem. Soc. Faraday Trans.*, 1994, **90**, 803–807.

[89] D. Meixner, D. Arthur and S. George, *Surf. Sci.*, 1992, **261**, 141–154.

[90] Y. Yanagisawa, K. Takaoka and S. Yamabe, *J. Chem. Soc.-Faraday Trans.*, 1994, **90**, 2561–2566.

[91] S. Boys and F. Bernardi, *Mol. Phys.*, 1970, **19**, 553–&.

[92] R. Grimes, C. Catlow and A. Stoneham, *J. Phys.-Condes. Matter*, 1989, **1**, 7367–7384.

[93] R. W. Williams and D. Malhotra, *Chem. Phys.*, 2006, **327**, 54–62.

[94] E. Florez, P. Fuentealba and F. Mondragon, *Catal. Today*, 2008, **133**, 216–222.

[95] D. Cornu, H. Guesmi, J.-M. Krafft and H. Lauron-Pernot, *J. Phys. Chem. C*, 2012, **116**, 6645–6654.

[96] Y. Yanagisawa, K. Takaoka, S. Yamabe and T. Ito, *J. Phys. Chem.*, 1995, **99**, 3704–3710.

[97] G. Preda, G. Pacchioni, M. Chiesa and E. Giamello, *J. Phys. Chem. C*, 2008, **112**, 19568–19576.

[98] L. Giordano, U. Martinez, G. Pacchioni, M. Watkins and A. L. Shluger, *J. Phys. Chem. C*, 2008, **112**, 3857–3865.

[99] H.-Y. T. Chen, L. Giordano and G. Pacchioni, *J. Phys. Chem. C*, 2013, **117**, 10623–10629.

[100] S. Coluccia, F. Boccuzzi, G. Ghiotti and C. Morterra, *J. Chem. Soc., Faraday Trans. 1*, 1982, **78**, 2111–2119.

[101] A. L. Shluger, J. D. Gale and C. R. A. Catlow, *J. Phys. Chem.*, 1992, **96**, 10389–10397.

[102] Y. Wang, H. N. Nguyen and T. N. Truong, *Chem.-Eur. J.*, 2006, **12**, 5859–5867.

[103] S. Arndt, G. Laugel, S. Levchenko, R. Horn, M. Baerns, M. Scheffler, R. Schloegl and R. Schomaecker, *Catal. Rev.-Sci. Eng.*, 2011, **53**, 424–514.

[104] P. Myrach, N. Nilius, S. Levchenko, A. Gonchar, T. Risse, K.-P. Dinse, L. Boatner, W. Frandsen, R. Horn, H.-J. Freund, R. Schlgl and M. Scheffler, *ChemCatChem*, 2010, **2**, 854–862.

[105] G. Pacchioni and H. Freund, *Chem. Rev.*, 2013, **113**, 4035–4072.

[106] V. Sharma, G. Pilania and J. E. Lowther, *AIP Adv.*, 2011, **1**, 032129.

[107] L.-J. Shi, *Phys. Lett. A*, 2010, **374**, 1292–1296.

[108] S. Azzaza, M. El-Hilo, S. Narayanan, J. J. Vijaya, N. Mamouni, A. Benyoussef, A. El Kenz and M. Bououdina, *Mater. Chem. Phys.*, 2014, **143**, 1500–1507.

[109] S. Meskine, A. Boukortt, R. Hayn and A. Zaoui, *Phys. Status Solidi B*, 2014, **251**, 845–849.

[110] P. Wu, G. Cao, F. Tang and M. Huang, *Comp. Mater. Sci.*, 2014, **86**, 180–185.

[111] P. Panigrahi, T. Hussain, C. M. Araujo and R. Ahuja, *J. Phys.: Condens. Matter*, 2014, **26**, 265801.

[112] P. Panigrahi, C. M. Araujo, T. Hussen and R. Ahuja, *Sci. Technol. Adv. Mater.*, 2014, **15**, 035008.

[113] G. Lewis and C. Catlow, *J.Phys.C Solid State Phys.*, 1985, **18**, 1149–1161.

[114] T. Keal and D. Tozer, *J. Chem. Phys.*, 2005, **123**, year.

[115] M. Dolf, U. Wedig, H. Stoll and H. Preuss, *J. Chem. Phys.*, 1987, **86**, 866–872.

[116] H. Rooksby and N. Tombs, *Nature*, 1951, **167**, 364.

[117] D. Rodbell and J. Owen, *J. Appl. Phys.*, 1964, **35**, 1002–1003.

[118] P. Anderson, *Phys. Rev.*, 1950, **79**, 350–356.

[119] N. Guskos, G. Zolnierkiewicz, J. Typek, D. Sibera, U. Narkiewicz and W. Lojkowski, *Acta. Phys. Pol. A*, 2011, **120**, 1074–1079.

[120] D. K. Kanan and E. A. Carter, *J. Phys. Chem. C*, 2012, **116**, 9876–9887.

[121] R. Hammami, A. Dhouib, S. Fernandez and C. Minot, *CATALYSIS TODAY*, 2008, **139**, 227–233.

[122] D. O. Scanlon, A. Walsh, B. J. Morgan, M. Nolan, J. Fearon and G. W. Watson, *J. Phys. Chem. C*, 2007, **111**, 7971–7979.

[123] A. Shluger, E. Kotomin and L. Kantorovich, *J. Phys. C*, 1986, **19**, 4183–4199.

[124] M. Wu, C. Truong, K. Coulter and D. Goodman, *J. Am. Chem. Soc.*, 1992, **114**, 7565–7567.

[125] I. Balint and K. Aika, *Appl. Catal. A*, 2000, **196**, 209–215.

[126] T. Bush, J. Gale, C. Catlow and P. Battle, *J. Mater. Chem.*, 1994, **4**, 831–837.

[127] J. Anchell and E. Glendending, *J. Phys. Chem.*, 1994, **98**, 11582–11587.

[128] J. L. Anchell, K. Morokuma and A. C. Hess, *J. Chem. Phys.*, 1993, **99**, 6004–6013.

Appendix A

List of Publications

The following publications were produced directly from results which form part of this thesis:

- C.A. Downing, A.A. Sokol and C.R.A. Catlow "The reactivity of CO_2 on the MgO (100) surface", *Phys. Chem. Chem. Phys.*, 2014, **16**, 184–195
- C.A. Downing, A.A. Sokol and C.R.A. Catlow "The Reactivity of CO_2 and H_2 at Oxygen Vacancies on the MgO (100) Surface", *Phys. Chem. Chem. Phys.*, 2014, **16**, 21153–21156

The following additional publications resulted from work on separate projects undertaken during the same time period as the work in this thesis:

- C. A. Downing, B. Ahmady, C. R. A. Catlow & N. H. de Leeuw "The interaction of hydrogen with the (010) surfaces of Mg and Fe olivine as models for interstellar dust grains: a density functional theory study", *Phil. Trans. R. Soc. A.*, 2013, **371**
- R. Su, R. Tiruvalam, A.J. Logsdail, Q. He, C.A. Downing, M.T. Jensen, N. Dimitratos, L. Kesavan, P.P. Wells, R. Bechstein, H.H. Jensen, S. Wendt, C.R.A. Catlow, C.J. Kiely, G.J. Hutchings, and F. Besenbacher "Designer Titania Supported Au-Pd Nanoparticles for Efficient Photocatalytic Hydrogen Production", *ACS Nano*, 2014, **8**, 3490–3497

Appendix B

Calculation Parameters

Basis Sets

All basis sets used as part of the calculations described within this thesis are reproduced in full. Work described in Chapter 3 used the GAMESS-UK code for QM calculations, while work described in Chapters 4–6 used the NWChem code. For simplicity, all basis sets are given in the NWChem format.

MgO

Mg atoms - Modified Def2 QZVP

```
Mg    S
605967.7875300              0.000014430176617
 90569.0946920              0.00011249871807
 20574.2528440              0.00059264972450
  5818.6284865              0.0024988770424
  1895.6296075              0.0090230775141
```

```
   683.45941021           0.028579919806
   266.18219762           0.079064453923
   110.11220010           0.18269337814
    47.777041234          0.32157193967
    21.542166149          0.35028259389
Mg     S
   174.12136378           0.022931111278
    53.484972498          0.19151777552
    20.500213307          0.61155711055
Mg     S
     9.8056826922         1.0000000
Mg     S
     3.5402989348         1.0000000
Mg     S
     1.5450850046         1.0000000
Mg     S
     0.66540195432        1.0000000
Mg     S
     0.14355439071        1.0000000
Mg     S
     0.066624673468       1.0000000
Mg     S
     0.029772648266       1.0000000
Mg     P
   893.20460829           0.00034958267428
   211.78258286           0.0029811890111
    68.443200537          0.015517845758
    25.727265349          0.057578659557
    10.606634281          0.15610307853
     4.5934126484         0.29230912580
     2.0100469807         0.37219024072
```

```
     0.87384841536           0.27578088891
Mg     P
     0.35615076666           1.0000000
Mg     P
     0.18995954356           1.0000000
Mg     D
     3.8100000               1.0000000
Mg     D
     0.6500000               1.0000000
Mg     D
     0.2000000               1.0000000
Mg     D
     0.0520000               1.0000000
```

Functions removed from standard Def2 QZVP basis set for Mg:

```
Mg     P
     0.074580135669          1.0000000
Mg     P
     0.029221641309          1.0000000
Mg     F
     0.1600000               1.0000000
```

O atoms - Modified Def2 TZVP

```
O      S
 27032.3826310               0.00021726302465
  4052.3871392               0.0016838662199
   922.32722710              0.0087395616265
   261.24070989              0.035239968808
```

```
    85.354641351            0.11153519115
    31.035035245            0.25588953961
O     S
    12.260860728            0.39768730901
     4.9987076005           0.24627849430
O     S
     1.1703108158           1.0000000
O     S
     0.46474740994          1.0000000
O     S
     0.18504536357          1.0000000
O     P
    63.274954801            0.0060685103418
    14.627049379            0.041912575824
     4.4501223456           0.16153841088
     1.5275799647           0.35706951311
O     P
     0.52935117943          1.0000000
O     P
     0.17478421270          1.0000000
O     D
     2.31400000             1.0000000
O     D
     0.64500000             1.0000000
```

Functions removed from standard Def2 TZVP basis set for O:

```
O     F
     1.42800000             1.0000000
```

C atoms - Modified Def2 QZVP

```
C     S
 67025.0710290               0.000038736308501
 10039.9865380               0.00030107917575
  2284.9316911               0.0015787918095
   647.14122130              0.0066087087195
   211.09472335              0.023367123250
    76.177643862             0.070420716898
    29.633839163             0.17360344953
    12.187785081             0.32292305648
C     S
    53.026006299             0.074897404492
    15.258502776             0.76136220983
C     S
     5.2403957464            1.0000000
C     S
     2.2905022379            1.0000000
C     S
     0.69673283006           1.0000000
C     S
     0.27599337363           1.0000000
C     S
     0.10739884389           1.0000000
C     P
   105.12555082              0.00084647553844
    24.884461066             0.0066274038534
     7.8637230826            0.030120390419
     2.8407001835            0.099951435476
     1.1227137335            0.23826299282
C     P
```

```
     0.46050725555          1.0000000
C     P
     0.18937530913          1.0000000
C     D
     1.84800000             1.0000000
C     D
     0.64900000             1.0000000
C     D
     0.22800000             1.0000000
```

Functions removed from standard Def2 TZVP basis set for C:

```
C     P
     0.075983791611         1.0000000
C     F
     1.41900000             1.0000000
C     F
     0.48500000             1.0000000
C     G
     1.01100000             1.0000000
```

H atoms - Modified Def2 TZVP

```
H     S
    34.0613410              0.0060251978
     5.1235746              0.045021094
     1.1646626              0.20189726
H     S
     0.32723041             1.0000000
H     S
```

```
     0.10307241             1.0000000
H     P
     0.8000000              1.0000000
```

Mn-MgO

Basis sets used for Mg, O and C were unmodified versions of the Def2 TZVP set - see https://bse.pnl.gov/bse/portal

Mn atoms - Modified Stuttgart Double Zeta

```
Mn    S
    15.5640010              1.0997890
    13.2869280             -1.3058510
     6.1372810             -0.7680240
Mn    S
     1.7659830              1.0000000
Mn    S
     0.7137740              1.0000000
Mn    P
    27.4320610              0.0838510
    11.3668730             -1.0649650
Mn    P
     4.4525400              0.2026520
     1.8534590              0.8317540
Mn    P
     0.6451800              1.0000000
Mn    P
     0.1030440              1.0000000
Mn    D
```

```
    29.5142230              0.0371620
     8.9628240              0.1827450
     3.0279670              0.4356070
Mn    D # UNCONTRACTED FROM PREVIOUS D FUNCTIONS
     0.9832920              0.5770530
Mn    D
     0.2703250              1.0000000
Mn    F
     0.7950000              1.0000000
```

Functions removed from standard Stuttgart double zeta basis set for Mn:

```
Mn    S
     0.0983280              1.0000000
Mn    S
     0.0370970              1.0000000
Mn    S
     0.0100000              1.0000000
Mn    P
     0.0282960              1.0000000
Mn    D
     0.0700000              1.0000000
Mn    F
     3.1180000              1.0000000
Mn    G
     1.9640000              1.0000000
```

MnO

All basis sets identical to those used for Mn-doped MgO

Li-MgO

Basis sets used for all atoms were unmodified versions of the Def2 TZVP set - see https://bse.pnl.gov/bse/portal

Effective Core Potentials

All ECPs used as part of the calculations described within this thesis are reproduced in full. Work described in Chapter 3 used the GAMESS-UK code for QM calculations, while work described in Chapters 4–6 used the NWChem code. For simplicity, all ECPs are given in the NWChem format.

MgO

Mg atoms - Stuttgart RLC ECP

```
Mg nelec 10
Mg ul
2       1.000000000             0.000000000
Mg S
2       1.732000000            14.676000000
Mg P
2       1.115000000             5.175700000
Mg D
2       1.203000000            -1.816000000
```

Mn-MgO

Mg atoms - Stuttgart RLC ECP

Identical to MgO work - see above

Mn atoms - Stuttgart RSC ECP

```
Mn nelec 10
Mn ul
2       1.000000000             0.000000000
Mn S
2      18.520000000           226.430902000
2       8.373000000            30.359072000
Mn P
```

```
2     18.920000000          142.154705000
2      8.017000000           21.536509000
Mn D
2     22.720000000          -22.568119000
2      7.640000000           -1.205810000
```

MnO

Mn(R1) atoms - Stuttgart RSC ECP

Identical to dopant atom in Mn-doped MgO work - see above

Mn(R2) atoms - Stuttgart RSC ECP

Identical to MgO work - see above

Li-MgO

Mg atoms - Stuttgart RLC ECP

Identical to MgO work - see above

Interatomic Potentials

MgO

```
# region 1-3
buck
Mg1     core O3     shel  798.394448  0.323866  0.000  0.000 12.000
lennard 12  6
Mg1     core O3     shel  182.246312  0.000000  0.000 12.000
buck
O1      core O3     shel  22764.300  0.149000 27.879  0.000 12.000
# region 1-4
buck
Mg1     core O4     shel  798.394448  0.323866  0.000  0.000 12.000
lennard 12  6
Mg1     core O4     shel  182.246312  0.000000  0.000 12.000
buck
O1      core O4     shel  22764.300  0.149000 27.879  0.000 12.000
# region 2-2
# region 2-3
buck
Mg2    core O3     shel  798.394448  0.323866  0.000  0.000 12.000
lennard 12  6
Mg2    core O3     shel  182.246312  0.000000  0.000 12.000
# region 2-4
buck
Mg2    core O4     shel  798.394448  0.323866  0.000  0.000 12.000
lennard 12  6
Mg2    core O4     shel  182.246312  0.000000  0.000 12.000
# region 3-3
```

```
buck
Mg3    core O3     shel  798.394448  0.323866  0.000  0.000 12.000
lennard 12  6
Mg3    core O3     shel  182.246312  0.000000  0.000 12.000
buck
O3     shel O3     shel  22764.300  0.149000 27.879  0.000 12.000
spring
O3      46.097205     3589.6947
# region 3-4
buck
Mg3    core O4     shel  798.394448  0.323866  0.000  0.000 12.000
lennard 12  6
Mg3    core O4     shel  182.246312  0.000000  0.000 12.000
buck
Mg4    core O3     shel  798.394448  0.323866  0.000  0.000 12.000
lennard 12  6
Mg4    core O3     shel  182.246312  0.000000  0.000 12.000
buck
O3     shel O4     shel  22764.300  0.149000 27.879  0.000 12.000
# exclusions of interactions in and between regions 4 and 5
coulomb
Mg4 core  Mg4 core  0.0  100.0
Mg4 core  O4  core  0.0  100.0
Mg4 core  O4  shel  0.0  100.0
O4  core  O4  core  0.0  100.0
O4  core  O4  shel  0.6  100.0
O4  shel  O4  shel  0.0  100.0
F5  core  F5  core  0.0  100.0
F5  core  Mg4 core  0.0  100.0
F5  core  O4  core  0.0  100.0
F5  core  O4  shel  0.0  100.0
```

```
# GULP CONTROL PARAMETERS
xtol opt   6.000000
gtol opt   6.000000
ftol opt   8.000000
maxcyc     5
stepmx     1.00
output xyz current.xyz
accuracy 12.000
```

Mn-MgO

```
# region 1-3
buck
Mg1  core O3  shel  1428.5  0.2945   0.0   0.0 12.0
O1   core Mg3 shel  1428.5  0.2945   0.0   0.0 12.0
O1   core O3  shel 22764.3  0.1490  23.0   0.0 12.0
Mn1  core O3  shel  1007.4  0.3262   0.0   0.0 12.0
# region 1-4
buck
Mg1  core O4  shel  1428.5  0.2945   0.0   0.0 12.0
O1   core Mg4 shel  1428.5  0.2945   0.0   0.0 12.0
O1   core O4  shel 22764.3  0.1490  23.0   0.0 12.0
Mn1  core O4  shel  1007.4  0.3262   0.0   0.0 12.0
# region 2-2
# region 2-3
buck
Mg2  core O3 shel  1428.5  0.2945   0.0   0.0 12.0
# region 2-4
buck
Mg2  core O4 shel  1428.5  0.2945   0.0   0.0 12.0
```

```
# region 3-3
buck
Mg3  shel O3 shel  1428.5  0.2945   0.0   0.0 12.0
O3   shel O3 shel 22764.3  0.1490  23.0   0.0 12.0
spring
Mg3   361.60
O3    54.76
# region 3-4
buck
Mg3  shel O4  shel  1428.5  0.2945   0.0   0.0 12.0
O3   shel Mg4 shel  1428.5  0.2945   0.0   0.0 12.0
O3   shel O4  shel 22764.3  0.1490  23.0   0.0 12.0
# exclusions of interactions in and between regions 4 and 5
coulomb
Mg4 core  Mg4 core  0.0  100.0
Mg4 core  Mg4 shel  0.6  100.0
Mg4 shel  Mg4 shel  0.0  100.0
Mg4 core  O4  core  0.0  100.0
Mg4 core  O4  shel  0.0  100.0
Mg4 shel  O4  core  0.0  100.0
Mg4 shel  O4  shel  0.0  100.0
O4  core  O4  core  0.0  100.0
O4  core  O4  shel  0.6  100.0
O4  shel  O4  shel  0.0  100.0
F5  core  F5  core  0.0  100.0
F5  core  Mg4 core  0.0  100.0
F5  core  Mg4 shel  0.0  100.0
F5  core  O4  core  0.0  100.0
F5  core  O4  shel  0.0  100.0
# GULP CONTROL PARAMETERS
xtol opt   6.000000
```

```
gtol opt   6.000000
ftol opt   8.000000
maxcyc     20
stepmx     1.00
output xyz current.xyz
accuracy 12.000
```

MnO

Note the decomposition of the Mn sublattice into two species, where one is differentiated by the “hat” label (chosen for simplicity and due to being recognised as a neutral input character by both NWChem and GULP).

```
# region 1-3
buck
O1   core  Mn^3  shel  1007.4  0.3262   0.0   0.0 12.0
O1   core  Mn3  shel  1007.4  0.3262   0.0   0.0 12.0
O1   core  O3   shel 22764.3  0.1490  23.0   0.0 12.0
Mn^1  core  O3   shel  1007.4  0.3262   0.0   0.0 12.0
Mn1  core  O3   shel  1007.4  0.3262   0.0   0.0 12.0
lennard 9 6
Mn^1 core Mn3 core 0.0 52.5 0.0 5.0
Mn1 core Mn^3 core 0.0 52.5 0.0 5.0
# region 1-4
buck
O1   core  Mn^4  shel  1007.4  0.3262   0.0   0.0 12.0
O1   core  Mn4  shel  1007.4  0.3262   0.0   0.0 12.0
O1   core  O4   shel 22764.3  0.1490  23.0   0.0 12.0
Mn^1  core  O4   shel  1007.4  0.3262   0.0   0.0 12.0
Mn1  core  O4   shel  1007.4  0.3262   0.0   0.0 12.0
```

```
lennard 9 6
Mn^1 core Mn4 core 0.0 52.5 0.0 5.0
Mn1 core Mn^4 core 0.0 52.5 0.0 5.0
# region 2-2
lennard 9 6
Mn^2 core Mn2 core 0.0 52.5 0.0 5.0
# region 2-3
buck
Mn^2  core  O3   shel  1007.4  0.3262   0.0   0.0 12.0
Mn2  core  O3   shel  1007.4  0.3262   0.0   0.0 12.0
lennard 9 6
Mn^2 core Mn3 core 0.0 52.5 0.0 5.0
Mn2 core Mn^3 core 0.0 52.5 0.0 5.0
# region 2-4
buck
Mn^2  core  O4   shel  1007.4  0.3262   0.0   0.0 12.0
Mn2  core  O4   shel  1007.4  0.3262   0.0   0.0 12.0
lennard 9 6
Mn^2 core Mn4 core 0.0 52.5 0.0 5.0
Mn2 core Mn^4 core 0.0 52.5 0.0 5.0
# region 3-3
buck
Mn^3  shel  O3   shel  1007.4  0.3262   0.0   0.0 12.0
Mn3  shel  O3   shel  1007.4  0.3262   0.0   0.0 12.0
O3   shel  O3   shel 22764.3  0.1490  23.0   0.0 12.0
lennard 9 6
Mn^3 core Mn3 core 0.0 52.5 0.0 5.0
spring
Mn^3   95.00
Mn3   95.00
O3    54.76
```

```
# region 3-4
buck
Mn^3  shel  O4   shel  1007.4  0.3262   0.0   0.0 12.0
Mn3  shel  O4   shel  1007.4  0.3262   0.0   0.0 12.0
O3   shel  Mn^4  shel  1007.4  0.3262   0.0   0.0 12.0
O3   shel  Mn4  shel  1007.4  0.3262   0.0   0.0 12.0
O3   shel  O4   shel 22764.3  0.1490  23.0   0.0 12.0
lennard 9 6
Mn^3 core Mn4 core 0.0 52.5 0.0 5.0
Mn3 core Mn^4 core 0.0 52.5 0.0 5.0
# exclusions of interactions in and between regions 4 and 5
coulomb
Mn^4 core  Mn^4 core  0.0  100.0
Mn^4 core  Mn^4 shel  0.6  100.0
Mn^4 shel  Mn^4 shel  0.0  100.0
Mn^4 core  O4  core  0.0  100.0
Mn^4 core  O4  shel  0.0  100.0
Mn^4 shel  O4  core  0.0  100.0
Mn^4 shel  O4  shel  0.0  100.0
Mn4 core  Mn4 core  0.0  100.0
Mn4 core  Mn4 shel  0.6  100.0
Mn4 shel  Mn4 shel  0.0  100.0
Mn4 core  O4  core  0.0  100.0
Mn4 core  O4  shel  0.0  100.0
Mn4 shel  O4  core  0.0  100.0
Mn4 shel  O4  shel  0.0  100.0
Mn^4 core  Mn4 core  0.0  100.0
Mn^4 core  Mn4 shel  0.0  100.0
Mn^4 shel  Mn4 core  0.0  100.0
Mn^4 shel  Mn4 shel  0.0  100.0
O4  core  O4  core  0.0  100.0
```

```
O4  core  O4  shel  0.6  100.0
O4  shel  O4  shel  0.0  100.0
F5  core  F5  core  0.0  100.0
F5  core  Mn^4 core  0.0  100.0
F5  core  Mn^4 shel  0.0  100.0
F5  core  Mn4 core  0.0  100.0
F5  core  Mn4 shel  0.0  100.0
F5  core  O4  core  0.0  100.0
F5  core  O4  shel  0.0  100.0
# GULP CONTROL PARAMETERS
xtol opt   6.000000
gtol opt   6.000000
ftol opt   8.000000
maxcyc     20
stepmx     1.000
output xyz current.xyz
accuracy 12.000
```

Li-MgO

```
# region 1-3
buck
Mg1  core O3  shel   1428.5   0.2945   0.0  0.0 12.0
O1   core Mg3 shel   1428.5   0.2945   0.0  0.0 12.0
O1   core O3  shel  22764.3   0.1490  23.0  0.0 12.0
Li1  core O3  shel    426.48  0.3000   0.0  0.0 12.0
# region 1-4
buck
Mg1  core O4  shel   1428.5   0.2945   0.0  0.0 12.0
O1   core Mg4 shel   1428.5   0.2945   0.0  0.0 12.0
```

```
O1   core O4  shel  22764.3   0.1490  23.0  0.0 12.0
Li1  core O4  shel    426.48  0.3000   0.0  0.0 12.0
# region 2-2
# region 2-3
buck
Mg2  core O3 shel  1428.5  0.2945   0.0   0.0 12.0
# region 2-4
buck
Mg2  core O4 shel  1428.5  0.2945   0.0   0.0 12.0
# region 3-3
buck
Mg3  shel O3 shel  1428.5  0.2945   0.0   0.0 12.0
O3   shel O3 shel 22764.3  0.1490  23.0   0.0 12.0
spring
Mg3   361.60
O3    54.76
# region 3-4
buck
Mg3  shel O4  shel  1428.5  0.2945   0.0   0.0 12.0
O3   shel Mg4 shel  1428.5  0.2945   0.0   0.0 12.0
O3   shel O4  shel 22764.3  0.1490  23.0   0.0 12.0
# exclusions of interactions in and between regions 4 and 5
coulomb
Mg4 core  Mg4 core  0.0  100.0
Mg4 core  Mg4 shel  0.6  100.0
Mg4 shel  Mg4 shel  0.0  100.0
Mg4 core  O4  core  0.0  100.0
Mg4 core  O4  shel  0.0  100.0
Mg4 shel  O4  core  0.0  100.0
Mg4 shel  O4  shel  0.0  100.0
O4  core  O4  core  0.0  100.0
```

```
O4  core  O4  shel  0.6  100.0
O4  shel  O4  shel  0.0  100.0
F5  core  F5  core  0.0  100.0
F5  core  Mg4 core  0.0  100.0
F5  core  Mg4 shel  0.0  100.0
F5  core  O4  core  0.0  100.0
F5  core  O4  shel  0.0  100.0
# GULP CONTROL PARAMETERS
xtol opt   6.000000
gtol opt   6.000000
ftol opt   8.000000
maxcyc     20
stepmx     1.00
output xyz current.xyz
accuracy 12.000
```